Annual Progress Report

The Texas Center for High Intensity Laser Science and the The Texas Petawatt Project

Spring, 2006

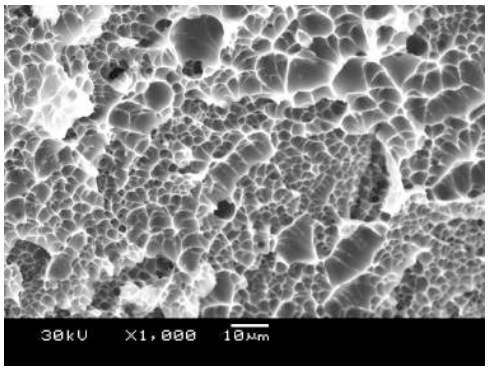

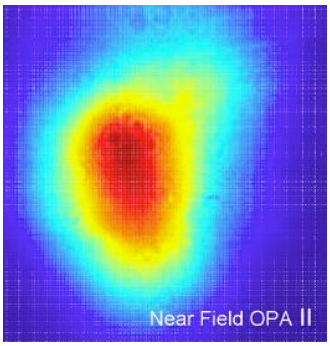

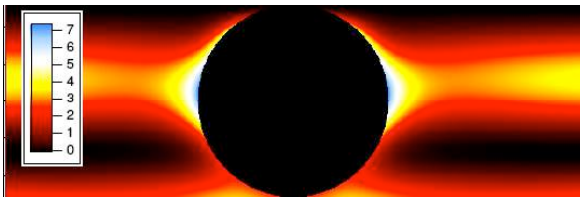

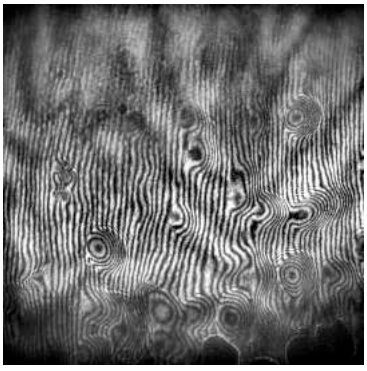

Annual Progress Report – Spring 2006
for SSAA Cooperative agreement DE-FC52-03NA00156

The Texas Center for High Intensity Laser Science
The Texas Petawatt Project

Submitted by Todd Ditmire (Director of TCHILS, University of Texas at Austin)

Contents:

I. Science activities at the Texas Center for High Intensity Laser Science

During 2005 under this SSAA Center, we have conducted a wide range of experiments. These experiments have utilized laser facilities at UT, LLNL, and Sandia. The emphasis of research in the Center is based in two areas, high energy density physics, including hydrodynamics and high temperature plasma experiments, and high strain rate materials science. In addition, the Center has been constructing a Petawatt laser facility. This project in progressing successfully and remains within our planned schedule. This document describes each of the science activities in the Center as well as the activities in support of the Petawatt laser development. The individuals involved in each Center activity are listed under each sub-section.

Section I describes each of the science activities in the Center, section II discusses the laser development activities and section III lists the individuals supported by the SSAA Center grant and all the publications resulting from the funding of the Center to date.

I.A Radiative blast wave studies on the Sandia Z-Beamlet Laser

Participants:
A. E. Edens, J. Osterhoff, D. R. Symes, and T. Ditmire (**University of Texas**)*
*J. F. Hansen and M. J. Edwards (**Lawrence Livermore National Laboratory**)*
*R.G. Adams, P. Rambo, L. Ruggles, I.C. Smith, and J. L. Porter (**Sandia National Laboratory**)*
**Now at Sandia National Lab*

A central activity within the Center involves the study of hydrodynamic behavior of high Mach number blast waves. Our interest in these wave is based on the fact that very high velocity blast waves can become radiative and exhibit hydrodynamics instabilities. These experimental studies have been conducted on a number of laser facilities. Over the last three years we have performed experiments on the LLNL Janus laser and the Sandia Z-Beamlet laser. We have also performed experiments in slightly different geometry on the UT THOR laser described in the next section. Experiments at Sandia during the past year have led to a number of publications and the graduation of the first PhD student from TCHILS.

Central to this work on radiative blast waves is the study of the stability of these shock waves [1-4] and how these instabilities affect supernovae dynamics. In particular, there are several instabilities of interest associated with the formation and evolution of shock waves produced by supernovae, i.e. supernova remnants(SNRs) [2,5]. One important hydrodynamic feature associated with some radiative SNRs, an overstability proposed by Vishniac et al., arises from a mismatch between the ram and thermal pressures at the surface of a blast wave which can cause a growing, oscillating ripple on that surface [3,6,7]. Radiative SNR shocks are cooler and more compressible than non-radiative SNR shocks, leading to a thinner blast front which is susceptible to this Vishniac overstability [8-11]. Vishniac et al. made quantitative predictions for the temporal evolution of small perturbations on a blast wave front and derived the growth rate of

the overstability as a function of the effective adiabatic index of the shocked material and wave number of the oscillation [7].Most experimental attempts to see the Vishniac overstability have used laser irradiation of a target to create a blast wave in a background gas [12,13]. These experiments take advantage of a laser's ability to deliver a large amount of energy to a small focal spot in a time span short compared to the evolution of the resulting explosion. There are several complications associated with these experiments that make it difficult to measure the growth rate of the overstability. The first complication for laser experiments in spherical geometry, as opposed to cylindrical geometry, is the effect of the laser's passage on the background gas, which can pre-ionize the gas. A second complication to experimental observation is that if the overstability grows from noise it is difficult to achieve large growth in the limited lifetime of the experiments.

Most of the data described here was acquired on the Z-Beamlet laser at Sandia National Laboratories [14], which fired 500J-1000J, 1ns pulses of 1054nm wavelength. During previous years data was taken on the Janus laser at Lawrence Livermore National Laboratory [15], which fired 10 J-150 J, 1ns laser pulses at 527nm wavelength (however, the upgrade of this laser in 2005 made shots to outside users scarce).

Building off the work on understanding laser produced blast waves that led to our Nov 2004 Physics of Plasmas article [16], we have measured the decay of perturbations induced on these blast waves and compared that rate of decay to theoretical predictions. The experimental setup used for these experiments is illustrated in Figure I.A.1. This setup was used at Sandia National Laboratories on the Z-Beamlet laser, which illuminated solid targets immersed in .01 atmospheres of background gas with 1 kJ, 1ns laser pulses. The resulting explosion launched a blast wave into the gas, which was imaged at a variable time later by a 80 mJ, 150 ps probe beam.

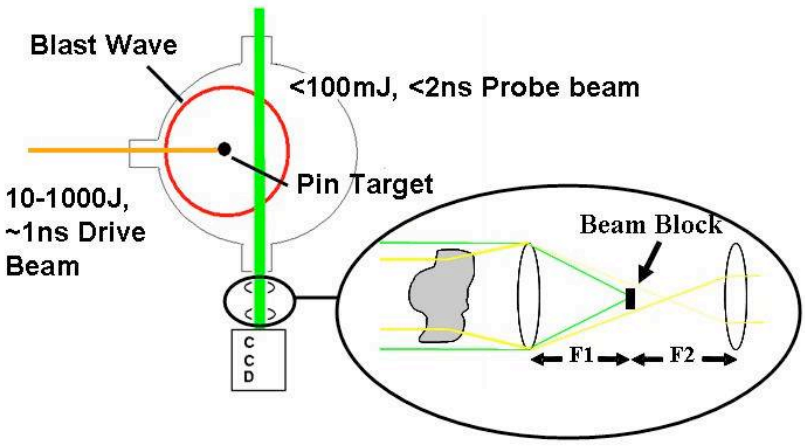

Figure I.A.1. Experimental setup of laser shock experiments. Drive beam, varying in energy from 10J-1000J, enters the chamber from left and illuminates a pin target. This creates a blast wave that is imaged by the probe laser onto a dark field imaging telescope, shown in the inset. The dark field telescope blocks light that passes through the chamber undeflected, but any light that encounters a density gradient is deflected around the beam block at the center of the telescope and shows up as a bright area.

Perturbations were induced on the surface of a blast wave by means of regularly spaced wire arrays placed in the path of the blast wave, Illustrated in figure I.A.2. According to the theory of Vishniac and Ryu, the evolution of a perturbation on a blast wave should vary as a power law in time with an exponent that depends on two factors: the mode number of the perturbation and the polytropic index of the medium in which the blast wave travels. By varying the spacing of the wires in the array, we were able to change the mode number of the induced perturbations. Similarly, the choice of background gad in the chamber determined the polytropic index of the blast wave material. We have measured the decay rate of perturbations for a number of different combinations of background gas and perturbation mode number and compared our experimental results to the theoretical predictions. Our experiments looked at 3 different mode number perturbations in each of 3 different background gasses: helium, nitrogen, and a mixture of nitrogen and xenon. The polytropic index of the background gas should depend inversely on the importance of radiation in that gas. Higher atomic number gasses will radiate more, therefore our blast waves in helium should radiate the least and those in the mixed gas should radiate the most. The complexity of the evolution of our blast wave varies directly with the importance of radiation, as the higher the radiation level, the more the properties of the gas will change with time and the greater the effects of the radiation on the surrounding system. A time sequence for blast waves in nitrogen gas is seen in figure I.A.3.

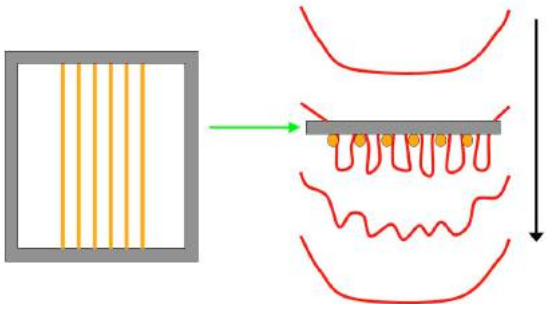

Figure I.A.2: Illustration of the planar wire array used to introduce perturbations on the blast wave

The theoretical predictions of Vishniac and Ryu for how perturbations should evolve are illustrated in figure I.A.4. The comparison of our experimental results to this data is seen in figure I.A.5. Since blast waves in helium gas radiate very little, we expect this gas to behave as an ideal monatomic gas and thus have a polytropic index of 1.67. We can see the experimental data for helium indeed agrees closely with the theoretical predictions for a polytropic index (gamma) of 1.67, which gives us great confidence that our measurements are valid. The nitrogen data seems to agree with a polytropic index of 1.3-1.5, and a further analysis of this data can be found in our recent publication in PRL [17]. Finally, the mixed gas data is somewhat more complicated, with the 1st two mode numbers implying a polytropic index between 1.1 and 1.2, while the third is more consistent with an index of 1.3. In general we can say that the implied polytropic index does in fact decrease with the importance of radiation in a gas, as is expected.

.

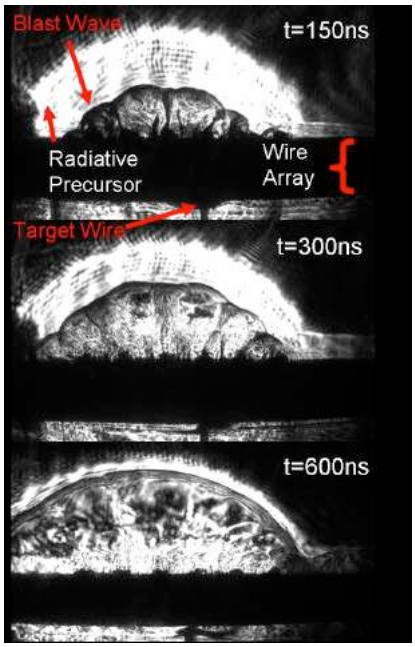

Figure I.A.3. Evolution of perturbations induced on a blast wave traveling in nitrogen gas. A 1kJ, 1ns laser pulse has illuminated a nylon wire target at t=0 and the resulting explosion launched a blast wave that traveled past a 4 mm spaced wire array, inducing perturbations on the surface of the blast wave. The perturbations clearly decrease in amplitude with time.

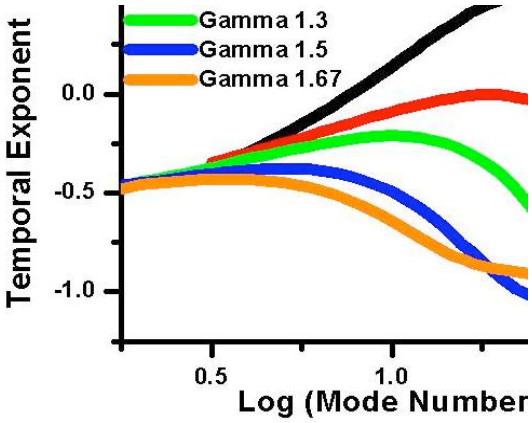

Figure I.A.4. Curves showing the predictions of Vishniac and Ryu for the evolution of perturbations on blast waves. Each curve shows the predicted decay rate versus mode number for a given polytropic index (gamma)

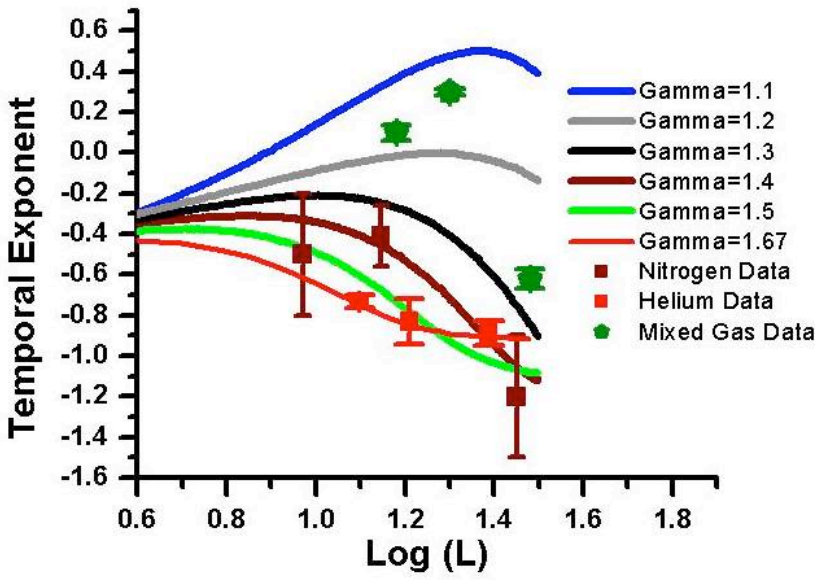

Figure I.A.5. Experimental data for the decay rate of perturbations on blast waves taken in a number of gasses compared to theoretical predictions

References for section I.A

1. J. J. Erpenbeck, Physics of Fluids **5** (10), 1181 (1962).
2. P.A. Isenberg, Astrophysical Journal **217** (2), 597 (1977).
3. D. Ryu and E. T. Vishniac, Astrophysical Journal **313** (2), 820 (1987).
4. B. G. Elmegreen and D. M. Elmegreen, Astrophysical Journal **220** (3), 1051 (1978).
5. J. P. Ostriker and C. F. Mckee, Reviews of Modern Physics **60** (1), 1 (1988); G. L. Welter, Astronomy and Astrophysics **105** (2), 237 (1982).
6. E. T. Vishniac, Astrophysical Journal **274** (1), 152 (1983).
7. D. Ryu and E. T. Vishniac, Astrophysical Journal **368** (2), 411 (1991).
8. E. Liang and K. Keilty, Astrophysical Journal **533** (2), 890 (2000).
9. G. Welter and J. Schmidburgk, Astrophysical Journal **245** (3), 927 (1981).
10. J. M. Blondin, E. B. Wright, K. J. Borkowski et al., Astrophysical Journal **500** (1), 342 (1998).
11. M. M. MacLow and M. L. Norman, Astrophysical Journal **407** (1), 207 (1993).
12. T. Ditmire, K. Shigemori, B. A. Remington et al., Astrophysical Journal Supplement Series **127** (2), 299 (2000); K. Shigemori, T. Ditmire, B. A. Remington et al., Astrophysical Journal **533** (2), L159 (2000); M. J. Edwards, A. J. MacKinnon, J. Zweiback et al., Physical Review Letters **8708** (8), art. no. (2001).
13. J. Grun, J. Stamper, C. Manka et al., Physical Review Letters **66** (21), 2738 (1991).
14. J. L. Rambo P. K. Rambo, Jr., G. R. Bennett, I.C. Smith, A.C. Erlandson, J.E. Murray, and J. Caird, OSA Trends in Optics and Photonocs, Conference on Lasers and Electro-Optics **73**, 362 (2002).

15. J.A. Glaze, W.W. Simmons, and W.F. Hagen, *Status of large neodymium glass lasers*. (Soc. Photo-Optical Instrumentation Engrs, Palos Verdes Estates, CA, USA Reston, VA, USA, 1976).
16. A. D. Edens, T. Ditmire, J. F. Hansen, et al., Physics of Plasmas **11**, 4968 (2004).
17. A. D. Edens, T. Ditmire, J. F. Hansen, et al., Physical Review Letters **95** (2005)

I.B Blast wave studies on the UT THOR Laser

Participants:
*J. Osterhoff, D. R. Symes, R. Fäustlin M. Maurer, A. Bernstein and T. Ditmire (**University of Texas**)*
*A. Edens (**Sandia National Laboratory**)*
*A. S. Moore, E. T. Gumbrell (**Atomic Weapons Establishment, UK**)*

In addition to these studies of blast waves from exploding point like laser plasmas, we have been pursuing a technique to make cylindrical blast waves in a gas jet. This technique will avoid the problem often seen in the studies of the last section in which the laser perturbs the medium as propagates toward the solid target. To do this, we utilize a gas target composed of rare gas clusters. Clusters are an intermediate state between solids and gases and combine efficient energy absorption properties with a low average density. This makes them an ideal medium in which to study highly energetic hydro events.

The experiments were conducted at the University of Texas using the THOR laser system which is a 20 TW-Ti:Sapphire system providing 0.7 J of energy in a 35 fs FWHM pulse at a repetition rate of 10 Hz. The 800 nm wavelength beam was focused to a peak intensity on the order of 10^{17} W/cm^2 into a cluster spray. In this experiment shock waves were produced by focusing laser light up to intensities of $1\text{x}10^{18}$ W/cm^2 with a f/7 spherical mirror into a gas plume of hydrogen, argon or xenon clusters. The THOR laser was focused to a spot ≈50 μm in diameter located 8mm below the gas jet. The clusters absorb about 50% of the laser light leading to energy deposition of ≈50mJ/mm in a cylindrical filament of a diameter determined by the laser focus and a length ≈4mm. After the laser pulse, a shock is launched into the surrounding gas which was monitored using interferometric and dark-field imaging. The interferogram yields phase information which can be directly transformed into a radial electron density profile and the dark-field images diagnose the spatial derivative of the electron density and hence are sensitive to shock front modulations and radiative ionization events occurring outside the blast wave shell. For the probing a small portion of the main beam was passed through a separate compressor and frequency doubled inside a KDP crystal. The probe beam could be continuously time delayed relative to the main heating beam Δt in a time window of -3.4 ns $\leq \Delta t \leq$ 97.0 ns. Thus a mapping of the shock evolution as a function of time was possible over nearly 100 ns with accuracy of a few picoseconds.

Irradiating xenon clusters with the full laser power created radiative blast waves with strong deviations from an adiabatic Sedov-Taylor trajectory. In cylindrical geometry, a purely energy conserving blast wave should exhibit a radius dependance with time as $t^{1/2}$. This is shown in figure I.B.1 where the late-time (>10ns) blast wave radius fits to a power law of $\alpha = 0.42 \pm 0.01$. The $\alpha = ½$ Sedov-Taylor solution is shown in blue. In addition, clear radiative precursors are visible in the dark field schlieren images and in the electron density profiles obtained from the interferograms shown in figure I.B.2.

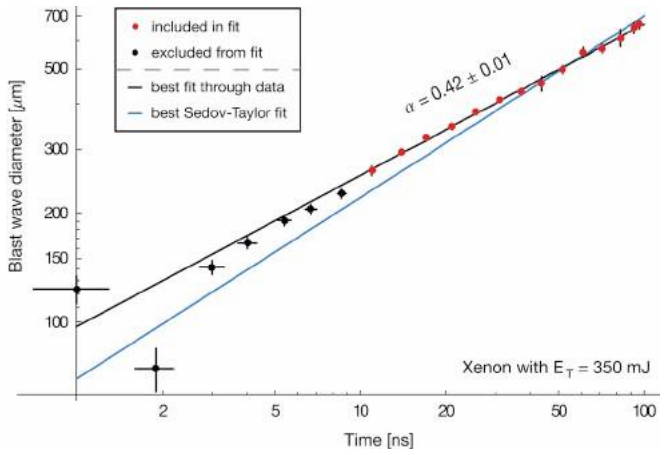

Figure I.B.1. Radiative heat transport in xenon leads to a reduced deceleration parameter α.

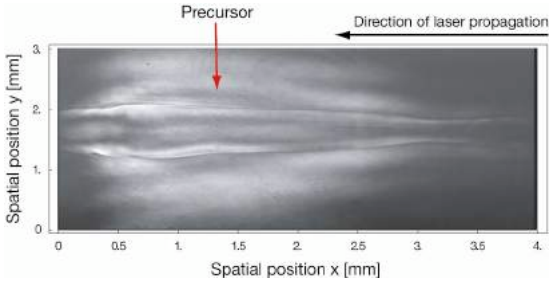

Figure I.B.2. Dark-field images of xenon plasmas show strong evidence of major radiative energy losses.

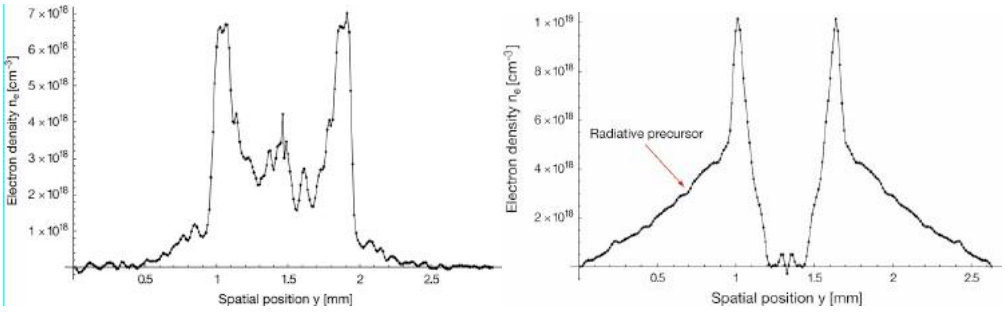

Figure I.B.3 .Electron density profiles in argon (left) and xenon (right). The xenon exhibits a clear ionization precursor ahead of the shock front.

By changing the target gas we can easily change the importance of radiation within the system. The shock fronts in argon drop sharply with very little ionization of the gas ahead of the shock and the blast wave evolution shows no significant deviation from the adiabatic trajectory. As stated before, a radiative loss from the blast wave should increase its compressibility, thinning the shock shell. Indeed, we compared the shell thickness in xenon and argon at equal blast wave radii, shown in figure I.B.3, and found a considerable reduction for the higher *Z* gas.

During this past year we therefore undertook a comparison of blast waves in a number of gases to further explore the phenomena seen in figure I.B.3 Typical images of blast waves in hydrogen and xenon cluster gases are shown in figure I.B.4. The shock is visible as a bright line in the dark-field images and a sudden large fringe shift in the interferograms. In Xe, surrounding gas is ionized because of the radiation emitted by the hot, shocked material. These precursors are seen as fringe shifts and a glow ahead of the shock (also observed in figure I.B.2), features which are absent in the low Z hydrogen images. Through analysis of the interferograms we obtained the time history of the electron density profile in Ar and Xe blast waves, shown in figure I.B.5. The Xe data (similar to those in the figure I.B.2 but with better imaging resolution) show large precursors and thin-shell shocks of thickness $H \approx 100$ μm. In contrast for Ar the precursor is barely visible and the shock shells are thicker $H \approx 300$ μm. The trajectories for these blast waves are compared in figure I.B.6. The evolution of the Xe waves displays three distinct regions with different trajectories. Before about 8-10ns, the shock has yet to form. Then the blast wave enters a radiative phase, as suggested by the data above, with a deceleration parameter $\alpha = 0.39 \pm 0.01$. At about 30ns, the trajectory reverts to the energy-conserving Sedov-Taylor value of $\alpha = 0.51 \pm 0.01$ indicating that the energy losses from the shocked gas are no longer significant. The Ar blast waves follow the energy conserving trajectory $\alpha = 0.50 \pm 0.03$ for the entire time.

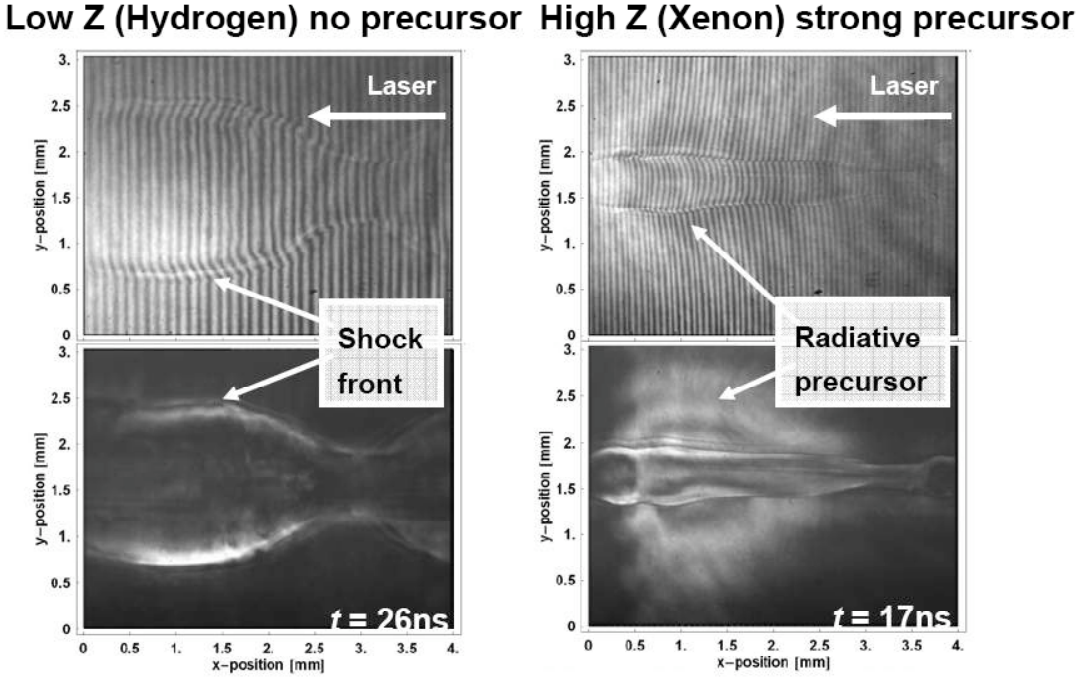

Figure I.B.4: Un-machined blast waves in hydrogen and xenon, at 26ns and 17ns respectively, illustrating the effect of the strong radiative precursor present in xenon. The laser focus is at x = 1mm in all the images.

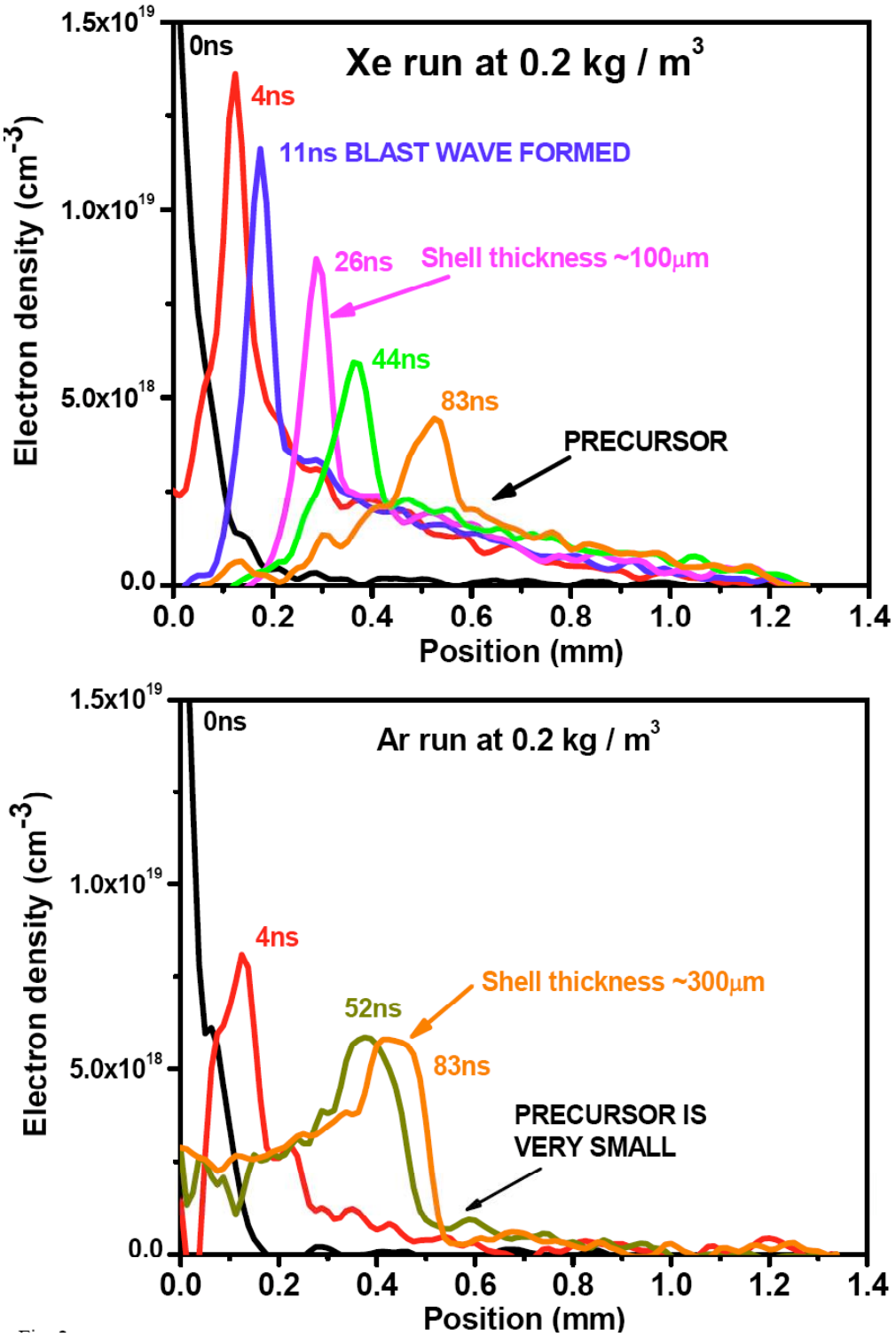

Figure I.B.5: Electron density over blast wave radius at different time steps. Xe blast waves exhibit thin-shell shocks with large precursors visible.

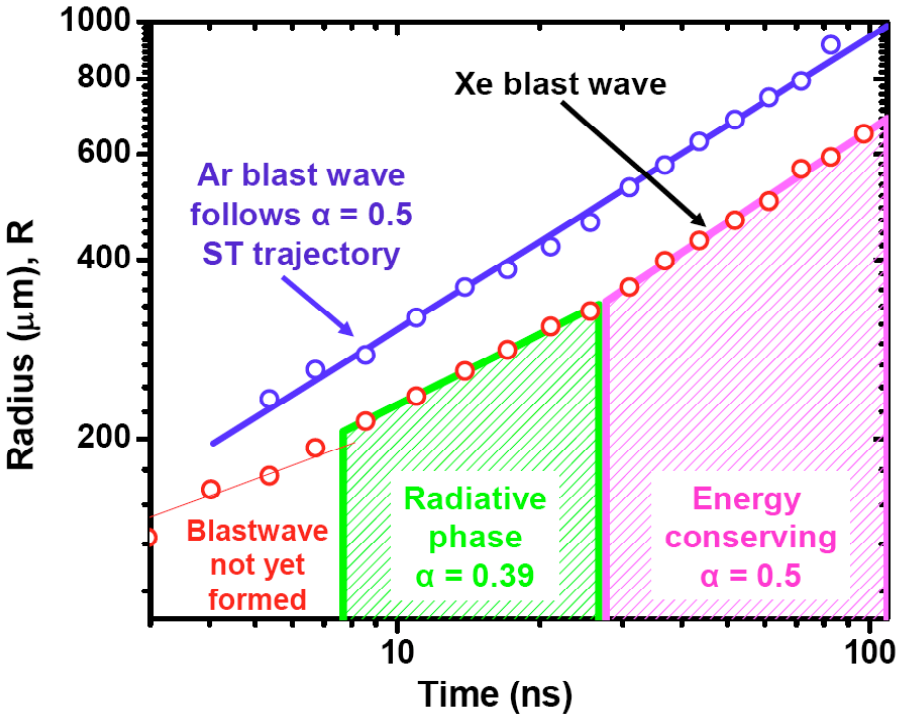

Figure I.B.6: Ar and Xe blast wave trajectories. Xe blast wave ceases to lose significant energy.

As mentioned, blast waves that strongly radiate should also undergo shell-thinning since the polytropic index of the gas reduces and the material becomes more compressible. We have studied this by measuring the shell thickness H as a function of the blast wave radius R in Ar and Xe. The compressibility $c=\rho_{shell}/\rho_0$ can be related to these parameters through $1/c = (2H/R) - (H^2/R^2)$ assuming that all the swept-up material resides in the shell. The comparison in figure I.B.7 showing thicker shells in Ar than Xe for the same blast wave radius demonstrates that the more strongly radiating Xe is more compressible because of a lower polytropic index γ. Interestingly the thickness of the Xe shells remains approximately the same during the radiative phase identified above suggesting a decreasing α. When the trajectory becomes energy conserving, H starts to increase. Surprisingly, the compression we measure for Xe is $c\approx$2-3, lower than the strong shock limit for an ideal gas of c=4. For a radiating gas with a lowered α, we would expect a compression exceeding 4. This indicates that the blast waves we generate are not in the strong shock limit (M>>1). This is a consequence of the preheating of the gas ahead of the shock. When the shock forms at ≈10ns the shock speed is ≈10km/s. Without preheat this would correspond to a Mach number $M\approx$50. In fact the precursor is heated to several eV so the ambient medium sound speed could be as high as 3km/s, drastically reducing the Mach number to ≈2.

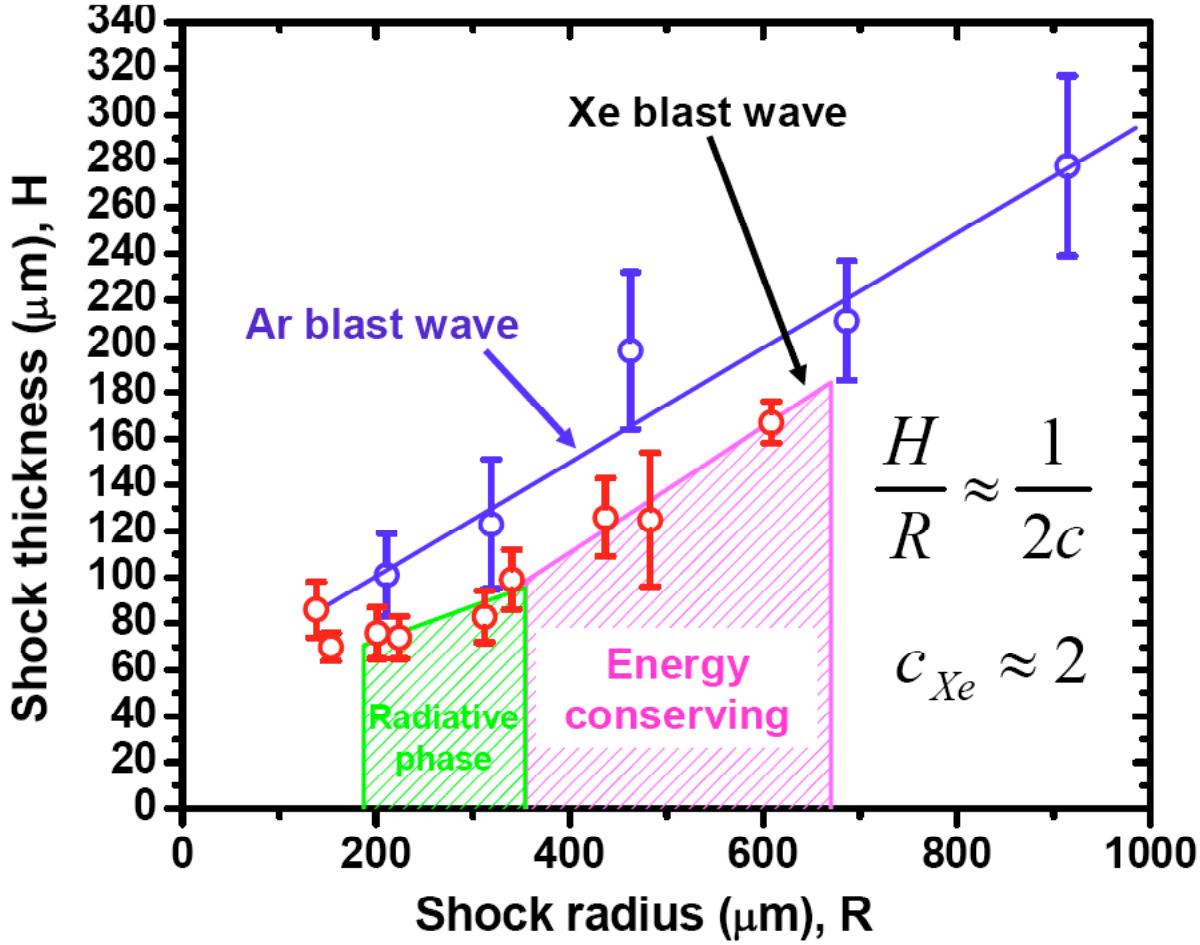

Figure I.B.7: Ar and Xe blast wave shell thickness. Xe blast waves appear to exhibit thinner shock shells.

These results provide convincing evidence that the blast waves we produce in Xe are strongly radiative. However, in these and in previous studies [1] no evidence of instability has been seen on the shock front. The next stage of the experiment was thus to impose artificially a modulation on the shock. These experiments have been performed recently and are still under analysis.

In this experiment we used a second transverse terawatt laser beam to destroy clusters in specific locations before the arrival of the main heating beam [2]. This leaves a medium with a constant atomic density but a variable cluster density. The disparity in absorption efficiencies between the clustered gas (≈50%) and the monatomic gas (≈1%) leads to regions of hot and cold plasma thus launching shaped blast waves. The laser beam used for machining the clusters had ≈50mJ energy in a ≈200fs pulse. (Because of this our heating beam energy was reduced to ≈300mJ.) We used a cylindrical and spherical lens combination to create a line focus of length ≈7mm and width ≈200 μm. An interferometer placed in the beam path before this enabled us to generate interference fringes in the beam of a variable wavelength. This focus was overlapped spatially with the position of the plasma filament produced by the heating beam using the imaging system and the beam was timed to arrive about 2ns prior to the heating beam. The images shown in figure I.B.8 are images when both beams irradiated the Ar clusters. We observe very nicely modulated blast waves. We will be exploring these waves more thoroughly in the coming year.

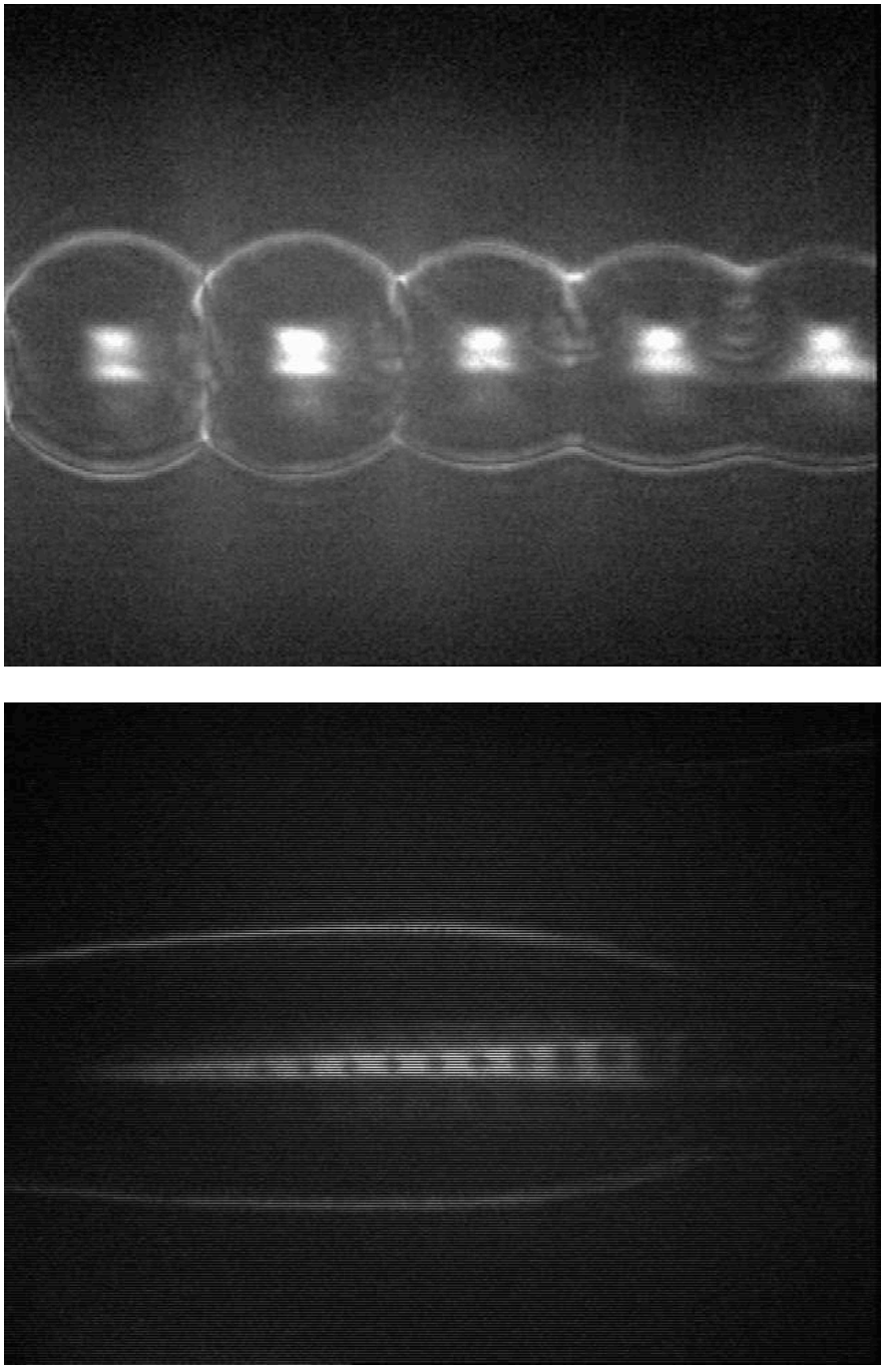

Figure I.B.8: Ar blast waves 24ns after heating beam incident with varied machining spacing. Acquired using dark field Schlieren method.

References for section I.B

[1] M.J Edwards et al. Phys. Rev Lett. 085004 (2001)
[2] Phys Plas **12**, 052707 (2005)

I.C Shocked materials studies on the THOR laser

Participants:
*W. Grigsby, S. Bless and T. Ditmire (**University of Texas**)*
*Jeff Colvin (**Lawrence Livermore National Laboratory**)*

A major component of our collaborative research with LLNL is in in the study of materials dynamics under laser shock loading. We have a number of projects devoted to this topic. These studies are motivated by the fact that a complete understanding of shock waves in materials requires comprehensive microscopic understanding of the compression wave. Within the Center we have undertaken a series of experiments to develop ways of studying atomic scale motions in materials as a material undergoes very high strain rate shock compression. To study these dynamics we are using short pulse lasers in high time resolution pump-probe experiments. Our initial work is concentrated on examining the shock induced melt transition in Tin.

In many cases of shock loading at high strain rates the material response is complicated by phase transitions such as lattice restructuring [1-3] and melting [1, 3-6]. To study these dynamics we are using lasers in high time resolution pump-probe experiments to develop a real time diagnostic on the phase of a shocked material. This can enable a probing of the entire phase history of a material as it shock compresses and releases.

Our work has so far concentrated on characterizing laser produced shock waves in thin metal foils backed by a transparent window. We shocked the front surface of a foil and probed the rear surface at various delay times using linear reflectivity and rear surface interferometry. The reflectivity of the metal is used to help diagnose the state of the material in optical pump probe measurements, while interferometry is used to determine the shock parameters (i.e. particle velocity and shock velocity).

The laser that we used was the THOR Ti:sapphire CPA laser system. We drove the shock waves with the uncompressed pulse, which was a Gaussian shaped stretched pulse with a width of 600 ps FWHM. After amplification to ~1 J, the beam was split into two parts. Most of the energy was diverted into the shock driving beam (~700 mJ) which contained a delay leg that allowed the beam to arrive in the target chamber at the same time as the probe beam. The energy not contained in the shock beam traveled into the pulse compressor where it was compressed to ~40 fs before traveling to the target chamber. The short time duration of the probe allowed us to take time-resolved images of the rear surface using an ordinary CCD camera. The short duration also gives us the ability to probe the target with high intensities and low fluences, so that diagnostics such as harmonics generation are possible in the future.

The experiment was performed inside of a vacuum chamber that allowed us to shock and probe without the worry of ionizing air near the focus of our beams. The shock driving laser was focused using an f/20 lens to a diameter of a few hundred microns FWHM, depending on the intensity for which we were aiming. The layout is illustrated in figure I.C.1. The main laser pulse drove an ablation-driven shock wave which traveled through the target [7]. For these experiments, our targets consisted of 4 μm of tin deposited onto the surface of a 50.8 mm diameter x 6 mm thick, (100) lithium fluoride window with a surface flatness of <= 0.3 μm. The target thickness was chosen so that the shock wave would not decay appreciably during propagation through the 4 μm of metal, while still allowing time for the shock to steepen. The window was used as a support structure for the thin foil, and also as a medium to confine the rear surface of the target to prevent material ejecta. In order to shock and probe a fresh surface for each shot, an XYZ translation stage was used to raster the target between shots.

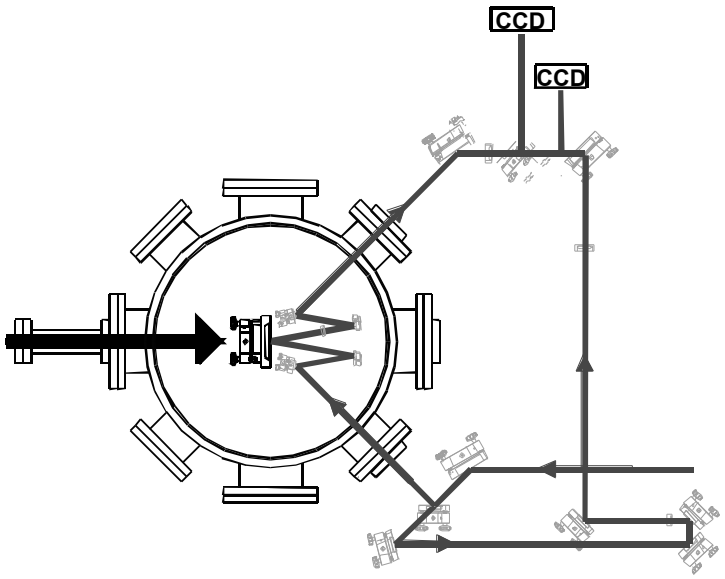

Figure I.C.1: Diagram of experimental setup. The pump beam arrives from the left and the probe beam arrives from the right.

The main diagnostic used to determine shock parameters was a Mach-Zehnder style interferometer that probed through the back surface of the lithium fluoride and reflected off of the tin interface. To observe smooth and straight fringes with our probes, the surface flatness requirements were typically < 3 μm across the entire substrate. One arm of the interferometer traveled into the vacuum chamber, reflected off of the target interface, and was then imaged onto the face of a CCD camera located outside of the chamber. The reference arm of the interferometer was located completely outside of the chamber and was adjusted to have equal imaging optics and equal optical delay to the probe arm. A combining beamsplitter was placed before the CCD, and adjustments were made to straighten and optimize the fringes on the camera. Before each shot was taken, a reference image was saved so that the change in surface position due to the shock wave could be measured accurately.

Data analysis was performed by Fourier analysis of the interferometric images, in a manner similar to Takeda, et al [8]. In this method, the image is first Fourier transformed, line by line. A super-Gaussian filter is then applied to the resulting spectrum to clean up the image. The primary background frequency is then subtracted by rotating the spectrum so this frequency lies at the origin. The new shifted spectrum is inverse Fourier transformed and the phase shift is extracted from the result. We were able to extract the distance *d* that the surface expanded using,

$$d = \frac{\lambda \cdot \phi(x, y)}{4\pi n \cdot Cos(\theta)} \qquad (1)$$

to the surface normal), and $\phi(x,y)$ is the unwrapped phase shift from the analysis of the interferograms.

We employed a second diagnostic that measured two-dimensional linear reflectivity. Our reflectivity data was obtained with the same probe pulse as in the interferometer, however a beamsplitter diverted a portion of the probe arm to a separate 16 bit CCD camera before the beam was combined with the reference arm. This allowed us to obtain data with high resolution, and also without the added convolution that fringes cause in the interferometer. The reflectivity data was normalized to reference shots taken before the shock wave was driven into the target, so that we could more easily compare multiple shots with each other.

In these experiments, we used five different laser intensities to drive shock waves into our Sn/LiF targets. We measured the displacement of the interface as a function of probe delay for each of these five cases. The maximum displacement that we could probe was limited by the fringe size relative to the shock spot, and also by the contrast between adjacent fringes on the CCD. For example, interferometric data for the $1x10^{13}$ W/cm^2 scan did not extend past 0.6 _m because of a lack of magnification in the probe imaging. For the other scans, where the fringes were distinguishable, we were able to observe up to a 2.1 μm expansion.

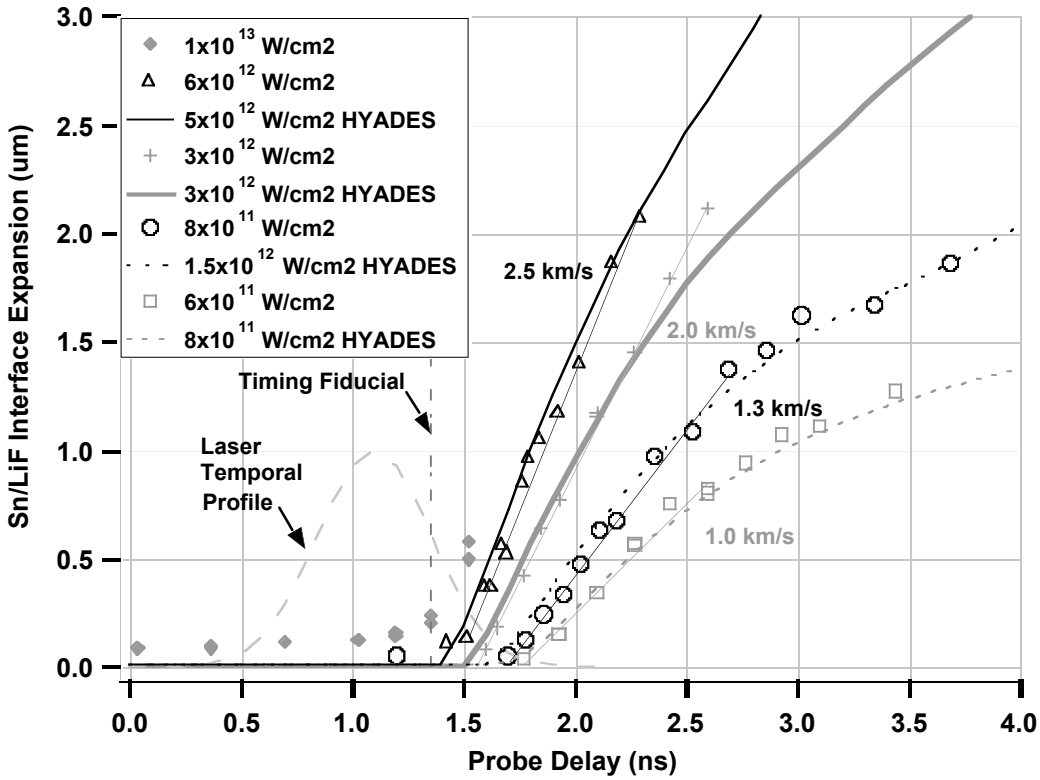

Figure I.C.2: HYADES simulations (curves) are fit to four of the five Sn/LiF interface expansion data (symbols). The numbers printed next to the linear fits to the data (solid thin lines) are the slopes of the lines (i.e. interface velocities).

A line was fit to the linear portion of the expansion data, illustrated in figure I.C.2, using a least-squares algorithm, to determine the particle velocity at shock breakout. The shock impedance mismatch between the tin and the lithium fluoride was accounted for so that the interface velocity could be converted into a particle velocity of the bulk tin. This particle velocity was then combined with Hugoniot data for tin to estimate the pressure observed at the interface within the target:

$$U_S = 2590\ \text{m/s} + 1.49 u_p \quad (1)$$

$$P = \rho_o U_S u_p \quad (2)$$

This pressure is compared with results from HYADES in figure I.C.2 and in Table 1.

TABLE 1. Experimental Results Combined with Simulation Parameters

Incident Laser Intensity (W/cm^2)	Pressure From Measured U_p Using the Hugoniot (±30kbar)	Laser Intensity Used in HYADES Simulation (W/cm^2)	Pressure From HYADES Simulation (kbar)
$6x10^{11}$	260	$8x10^{11}$	237
$8x10^{11}$	330	$1.5x10^{12}$	380
$3x10^{12}$	580	$3x10^{12}$	645
$6x10^{12}$	800	$5x10^{12}$	950
$1x10^{13}$	N/A	N/A	N/A

Data obtained from the reflectivity diagnostic are not currently understood. They contain what look like interference rings (See figure I.C.3) that may be due to a problem with the imaging system. More work must be done before any conclusions can be drawn from this data.

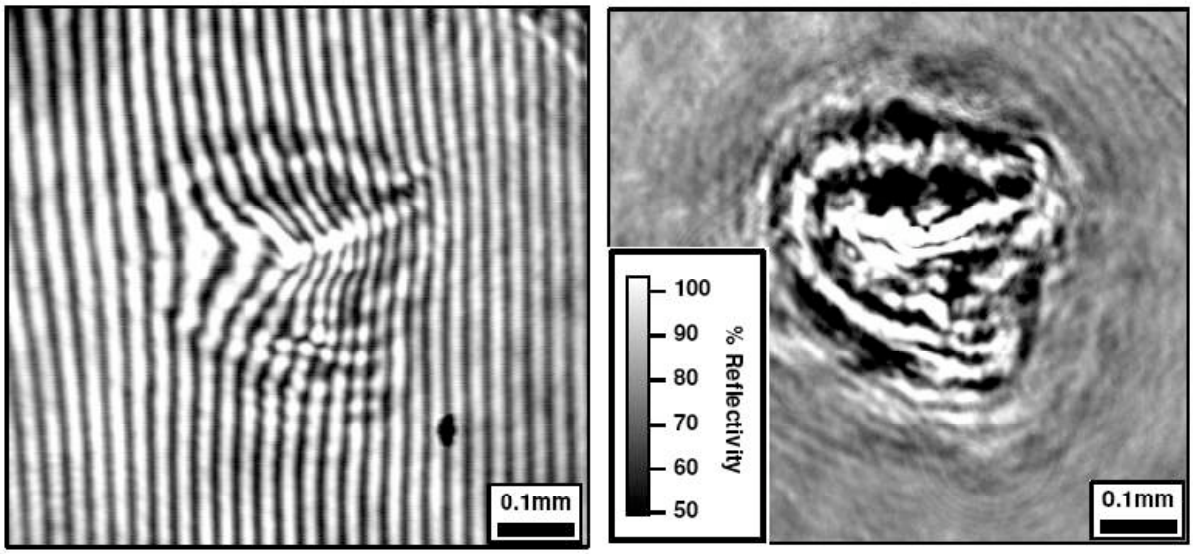

Figure I.C.3: Interferometric and reflectivity data from a shock breakout. The laser intensity was 6x10^{12} W/cm^2 and the probe delay was 450 ps after the timing fiducial.

Simulations of both the laser-target coupling and of the subsequent shock wave evolution in the target were run using HYADES, which is a one-dimensional radiation and hydrodynamics code developed by Jon Larsen [9]. The simulations were run with 150 mesh points spanning 4 μm of tin (feathered 5% for both surfaces) and 100 mesh points spanning 21 μm of lithium fluoride (feathered 5% from the front to the back). The EOSs used were SESAME #2160 and #7270 for tin and lithium fluoride, respectively. Results from these simulations were initially used to predict the approximate laser intensity necessary to shock melt tin at the rear surface of the target. These results agreed well with the initial LASNEX simulations that we performed. Later, after the experiments were carried out, HYADES simulations were used to match the Sn/LiF interface expansion to measured data. The laser intensity parameter was adjusted in the simulations until a match to the target expansion data was made. As figure I.C.2 shows, the resulting simulations match the data very well. Additionally, the intensities necessary in three of the four simulations agree perfectly with the measured intensities, within error (See Table 1).

We have shocked targets, consisting of 4 μm of tin coated on a (100) lithium fluoride substrate, with laser intensities ranging from 5x10^{11} to 5x10^{13} W/cm^2. The expansion of the rear surface of the tin due to the shock wave was measured as a function of probe delay using an interferometer. These data were compared with the known Hugoniot equations to estimate the pressure that the interface achieved. Preliminary HYADES simulations were able to match our expansion data

very well, when the incident laser intensity was used as a variable parameter. Although we were able to shock at pressures above the melt pressure of tin, we have not yet seen a consistent enough change in the reflectivity of our target that we can attribute to shock melting.

References for Section I.C

1. Mabire, C. and Hereil, P.L., *Shock induced polymorphic transition and melting of tin up to 53 GPa (experimental study and modelling)*. Journal De Physique Iv, 2000. **10**(P9): p. 749-754.
2. Barker, L.M., *Shock-Wave Study Of Alpha - Epsilon Phase-Transition In Iron*. Bulletin Of The American Physical Society, 1975. **20**(1): p. 25-25.
3. Swift, D.C., et al., *Dynamic response of materials on subnanosecond time scales, and beryllium properties for inertial confinement fusion*. 2005. **12**(5).
4. Asay, J.R., *Experimental Determination Of Shock-Induced Melting In Aluminum*. Bulletin Of The American Physical Society, 1975. **20**(1): p. 20-20.
5. Werdiger, M., et al., *Detecting of melting by changes of rear surface reflectivity in shocked compressed metals using an interferometric diagnostic method*. Laser and Particle Beams, 1999. **17**(3): p. 547-556.
6. Elias, P., Chapron, P., and Laurent, B., *Detection of Melting in Release for a Shock-Loaded Tin Sample Using the Reflectivity Measurement Method*. Optics Communications, 1988. **66**(2-3): p. 100-106.
7. Trainor, R.J., et al., *Ultrahigh-Pressure Laser-Driven Shock-Wave Experiments In Aluminum*. Physical Review Letters, 1979. **42**(17): p. 1154-1157.
8. Takeda, M., Ina, H., and Kobayashi, S., *Fourier-Transform Method Of Fringe-Pattern Analysis For Computer-Based Topography And Interferometry*. Journal Of The Optical Society Of America, 1982. **72**(1): p. 156-160.
9. Larsen, J.T. and Lane, S.M., *Hyades - a Plasma Hydrodynamics Code for Dense-Plasma Studies*. Journal of Quantitative Spectroscopy & Radiative Transfer, 1994. **51**(1-2): p. 179-186.

I.D Optical Diagnostic Development on Laser-Driven Shocks at the Janus Laser

Participants:
*A. C. Bernstein, W. Grigsby, A. Dalton, D. Milathianaki and T. Ditmire (**University of Texas**)*
*Jeff Colvin, Jim McNaney, Ray Smith, D. Price (**Lawrence Livermore National Laboratory**)*

As a part of our shocked materials effort in TCHILS we have also started work on the LLNL Janus laser. In fact, this specific project is a collaboration between TCHILS and an LLNL LDRD-ER project (Project #03-ERD-018, "Determination of the Microstructural Morphology of Shock-Induced Melt and Resolidification," Jeff Colvin, PI).

As described in the previous section, we are developing optical probes for laser driven shocks which represent a complementary diagnostic to standard x-ray and electron diffraction techniques. While optical probes, like optical reflectivity, have been used successfully to diagnose the ultrafast time dynamics of melting from laser heating in the past, we are extending

these techniques to melting induced by laser-driven shocks.

Development of these optical techniques are ongoing at the THOR table-top laser at the University of Texas. This activity, described in section I.C, is allowing the our team to gain experience on small scale, rep-rated lasers. To derive materials information from these techniques, it is necessary to drive larger targets with substantially higher laser energy. Accordingly, we began an effort in FY05 to study the diagnosis of shock-driven melting with the new, upgraded Janus laser. The experiment described here took place between April 11 and April 29, 2005 using the Janus laser at LLNL.

Detailed experimental designs were made prior to the experimental time at Janus. A first trip was made to make the UT researchers familiar with the workspace, to obtain detailed drawings of the room and target chamber. Back at UT, CAD drawings were made of the entire experimental apparatus, including available table locations, optical mounts, beam routing, and diagnostic location, as shown in figure I.D.1.

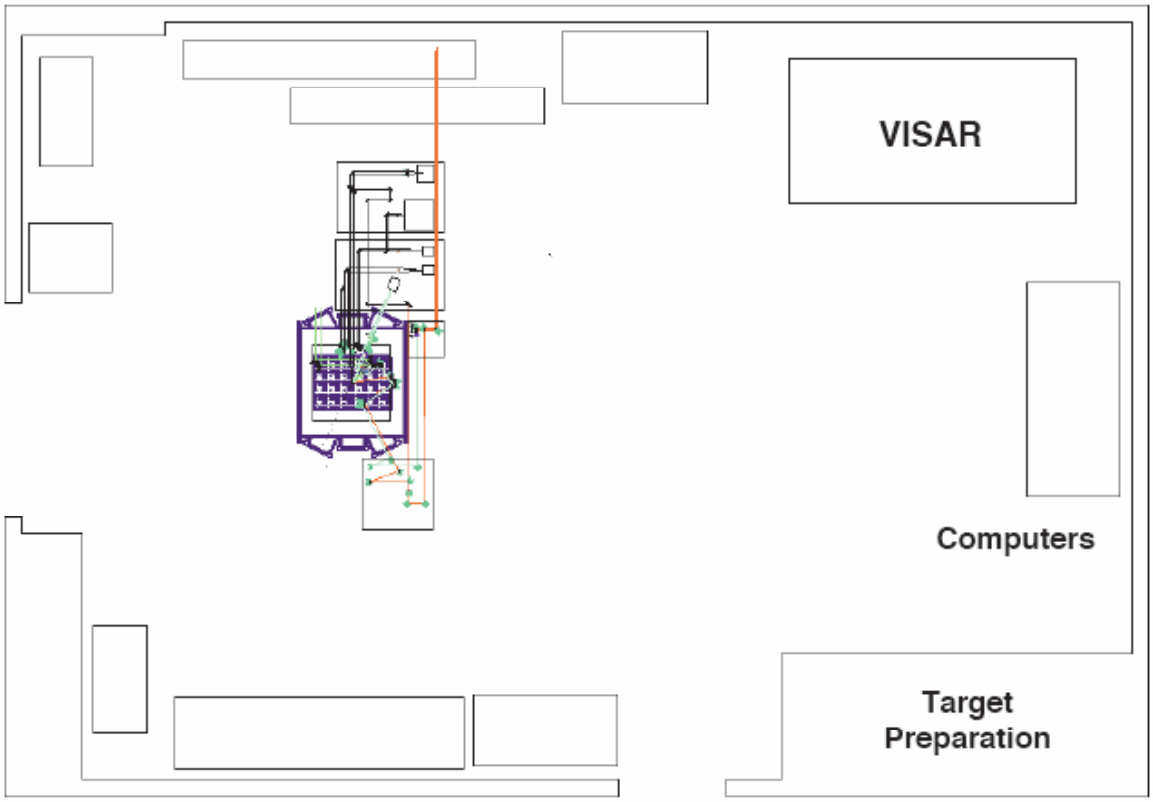

Figure I.D.1: Drawing of the room layout.

We conducted our first scaled-up experiments on Janus to drive shocks into planar Al foil targets of varying thickness. The Al foils were backed with LiF to impedance-match the shock-breakout from the rear surface of the Al, allowing us to examine shock-driven melting (as opposed to melting upon release). Laser energies were sufficient to shock-melt aluminum, which occurs

along the zero-temperature Hugoniot at a pressure of 1.2 Mbar. We diagnosed the shocks and the material state on the back (undriven) surface of the foil using a frequency-doubled Nd:YAG laser at the Janus facility as a probe beam, incident on the back surface. Figure I.D.2 is a schematic of the experiment.

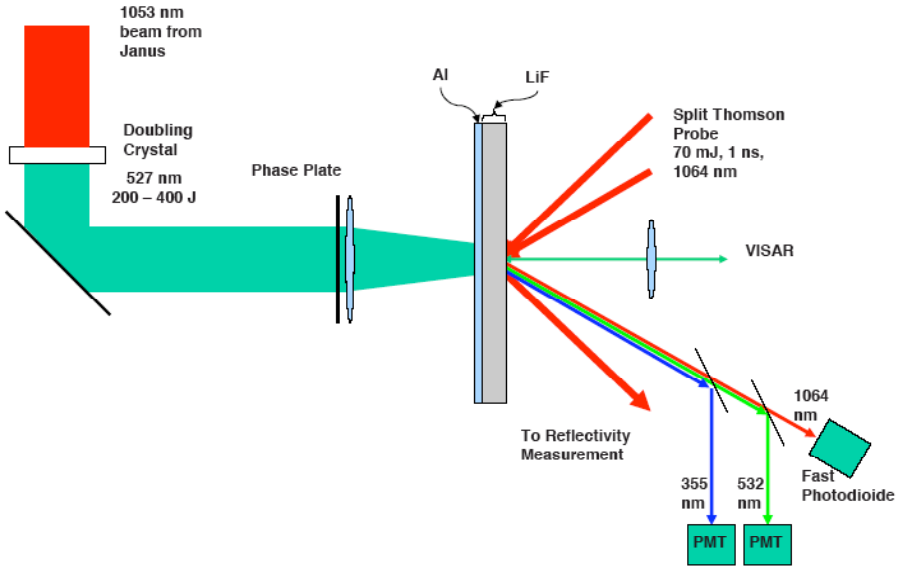

Figure I.D.2: Schematic of the experiment.

The four principal optical diagnostics employed were:

1. VISAR
2. Time-resolved optical reflectivity
3. Surface and bulk second harmonic generation
4. Third harmonic generation in the bulk near a surface

Both reflectivity (at 1064 nm) and harmonic generation detectors (532 nm and 355 nm) were situated along the specular direction. Multiple shots, with variation of pump and probe delays, as well as foil thickness and drive conditions, allowed a diagnosis of the back surface material throughout the history of the shock breakout. Figure I.D.3 shows a detailed drawing of this experiment. We took VISAR measurements of the shock-breakout (particle velocity) at the Al/LiF interface. These measurements also allowed us to estimate the Al reflectivity as a function of time at the 532 nm wavelength. We needed clearance for multiple probe beams, requiring construction of a new shroud to protect the VISAR pickup optics from scattered Janus light. In our first two shots the VISAR signal was contaminated by Janus light, but a final shroud configuration worked for the rest of the shots.

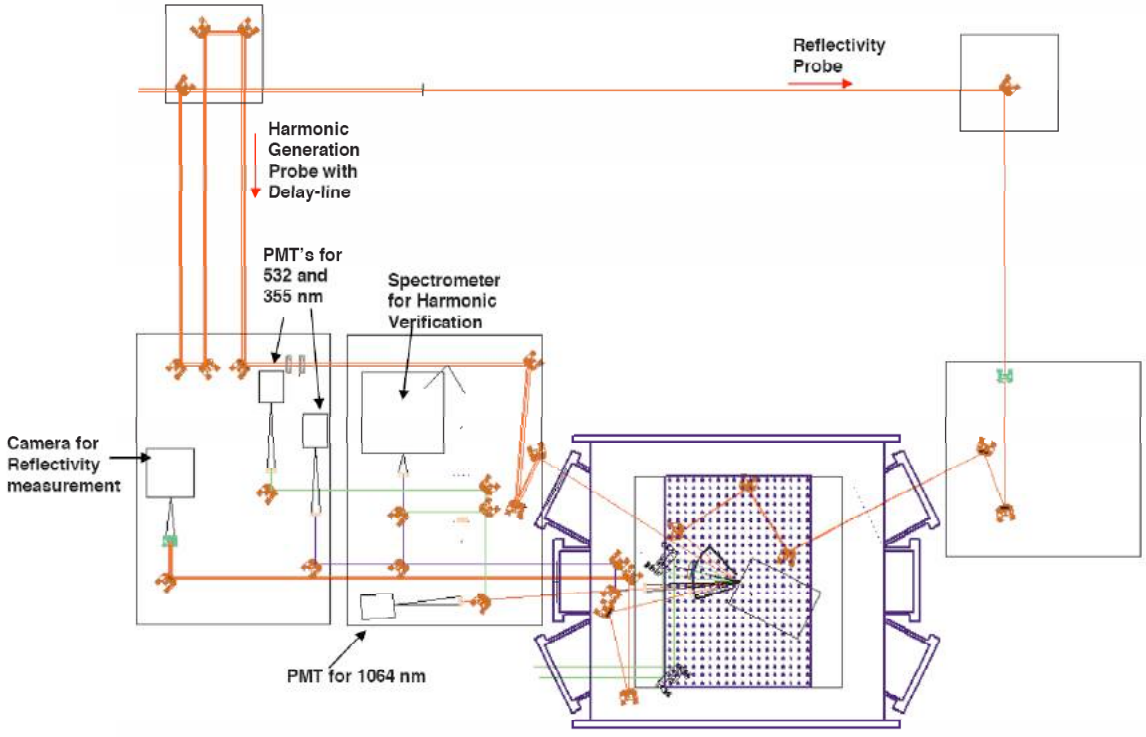

Figure I.D.3: Experimental Setup.

A program was written in-house at UT to analyze the VISAR images. It provides flexibility in the amount of spatial averaging performed in calculating the velocity profile of the Al during shock-breakout. It also displays the particle velocity across the entire target area, indicating any variations in target dynamics across its profile. Figures I.D.4 and I.D.5 show two representative VISAR measurements, and their analysis. Figure I.D.4 shows the result of a 76 J Janus drive pulse, which produced a peak velocity of 3 km/sec corresponding to a pressure of 764 bar. This matched well with LLNL calculations. Figure I.D.5 shows the result of a 196 J Janus pulse, driving the Al to about 5 km/sec corresponding to a pressure of 1635 barr. A noticeable second acceleration is found around 3 ns after the initial shock breakout, but is not flat across the surface. We are still investigating the origin of this feature.

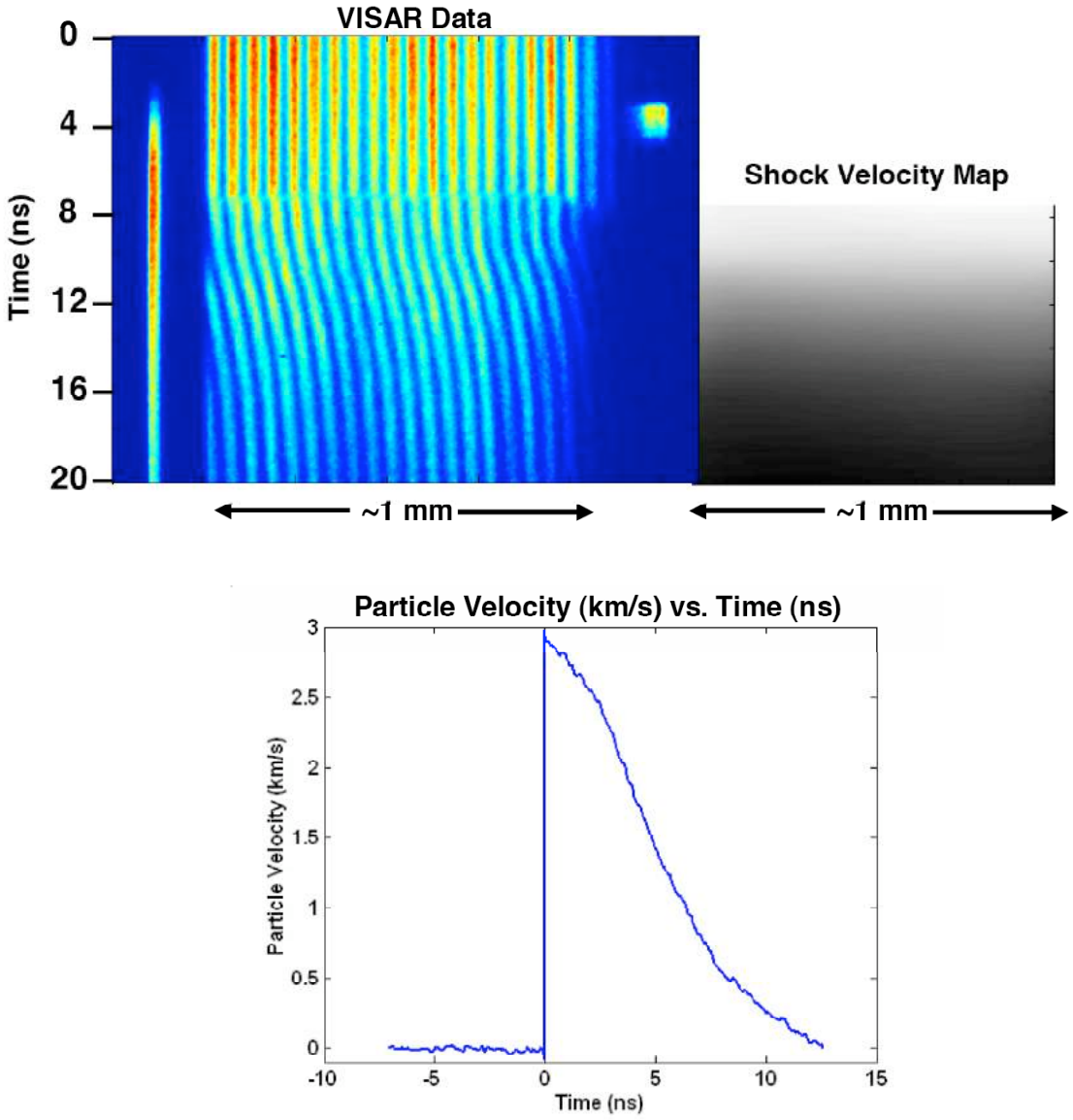

Figure I.D.4: VISAR information obtained for a 76 J Janus laser pulse. Top: VISAR trace (color) displayed side-by-side with brightness-indicated velocity map (grayscale). Shock breakout is flat across the target surface. Bottom: Particle velocity at one point of the Al rear surface as a function of time.

One of our hopes in these experiments was that surface third-harmonic generation (THG) and bulk second-harmonic generation (SHG) as produced in the aluminum, would serve as a fast optical probe of the transition from crystalline aluminum structure to amorphous. In anticipation of this, Nd:YAG lasers were used at the University of Texas to look for SHG and THG from a polycrystalline Al mirror and a LiF window. We recorded a signal from the aluminum which was several orders of magnitude greater than that generated by the LiF in transmission. Figure I.D.6 shows these data, and that they lie on a I^3 curve, as expected for a THG signal.

Despite this preliminary work, we were unable to find reliably THG or SHG signal with the actual targets at the Janus facility. In previous studies, THG was detectable at an intensity one

decade below that required to damage aluminum. However, our targets damaged before they emitted a clear THG signal. The broadband emission accompanying the target damage contaminated any signal we could see at the third-harmonic. We are still investigating this. While THG and SHG were detectable at UT when examining Al and LiF samples separately, one possible problem is that near-field enhancement of the field takes place at Al/LiF interface on the actual LiF-backed Al target, lowering the damage-threshold.

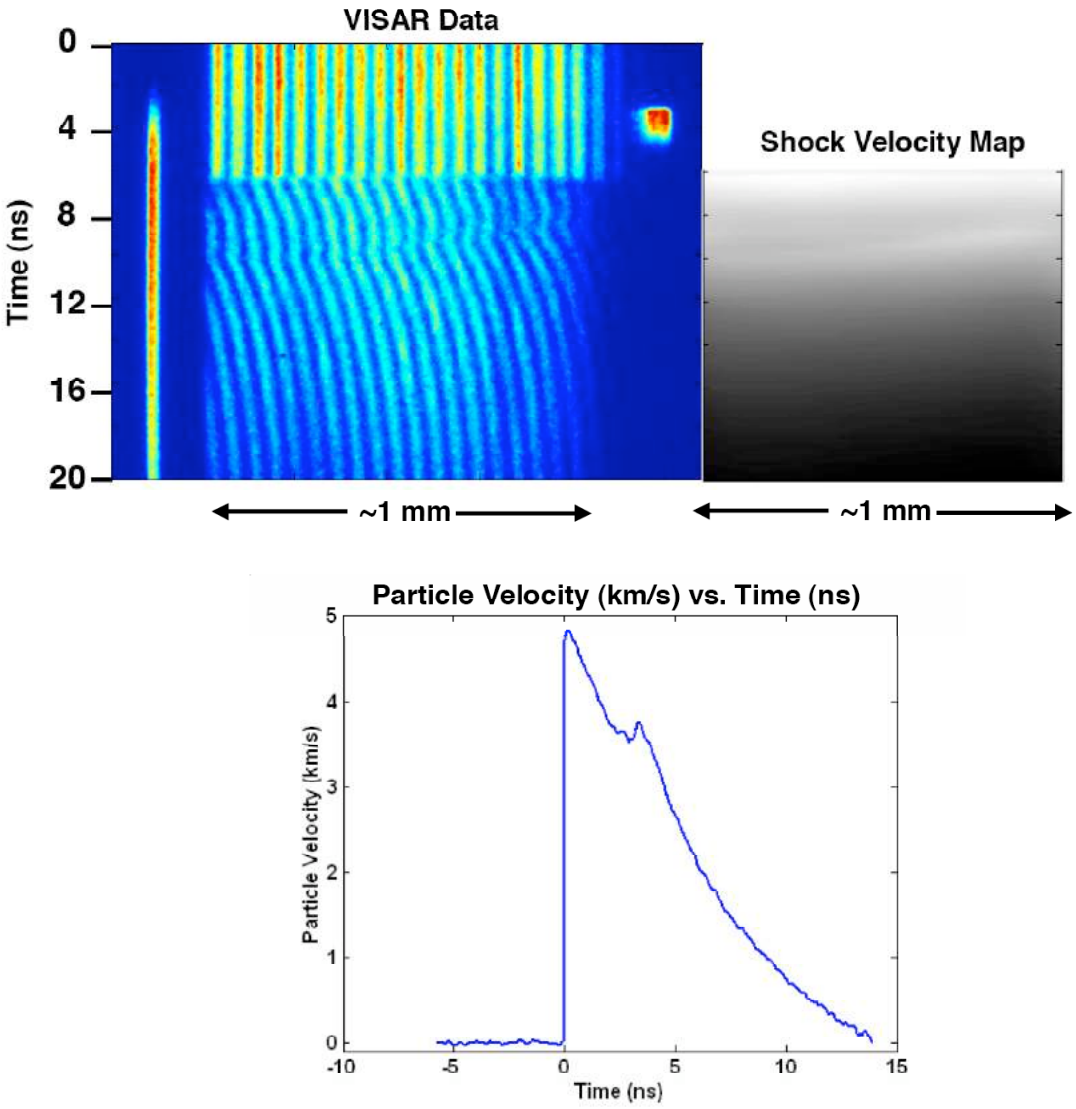

Figure I.D.5: VISAR information obtained for a 196 J Janus laser pulse. Top: VISAR trace (color) displayed side-by-side with brightness-indicated velocity map (grayscale). While shock breakout is flat across the target surface, around 3 ns later a secondary acceleration occurs which does vary across the target surface. A sharp drop in reflectivity is noticeable in the VISAR trace as Al experiences shock-driven melt. Bottom: Particle velocity at one point of the Al rear surface as a function of time.

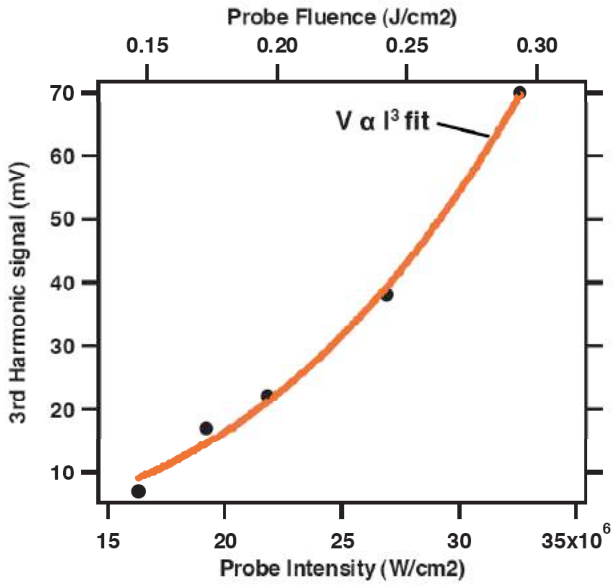

Figure I.D.6: Third harmonic signal measured on a polycrystalline Al mirror. The signal follows the expected I^3 law.

Although we were not able to detect harmonic generation below the intensity threshold of the probe beam for plasma generation at the Al/LiF interface (i.e., we saw a broadband signal here), we did obtain data on the two-color (1ω and 2ω) reflectivity of Al both well below and very near melt temperature. The initial data suggest that simple reflectivity measurements taken at two wavelengths may give detailed temporally-resolved information about the temperature and melting of Al during shock-breakout, as suggested by Benedict et al. [Phys. Rev. B 71, 064103 (2005)]. This occurs due to a resonance feature in the dielectric function of semi-crystalline Al, which changes its spectral features as a function of both temperature and pressure. This technique can also be scaled to the ultrafast domain in future experiments, because the technique relies on linear measurements, assuring that melting characteristics are resolved.

The reflectivity at 1064 nm was obtained with a fast photodiode measuring the probe reflected off the back of the Al foil, at the Al/LiF interface. A second reflectivity measurement at 532 nm was taken using the VISAR data itself. A portion of the VISAR YAG was sent directly to the streak camera, and not to the target, in order to normalize the reflectivity measurement in post-processing. It is seen on the left side of the VISAR traces in figures. I.D.4 and I.D.5.

Figure I.D.7 shows representative results of our measurement. The 532 nm reflectivity change is much faster for the 196 J shot than it is for the lower 76 J shot. However, the 1064 nm reflectivity changes more rapidly for the 76 J shot than it does for the 196 J

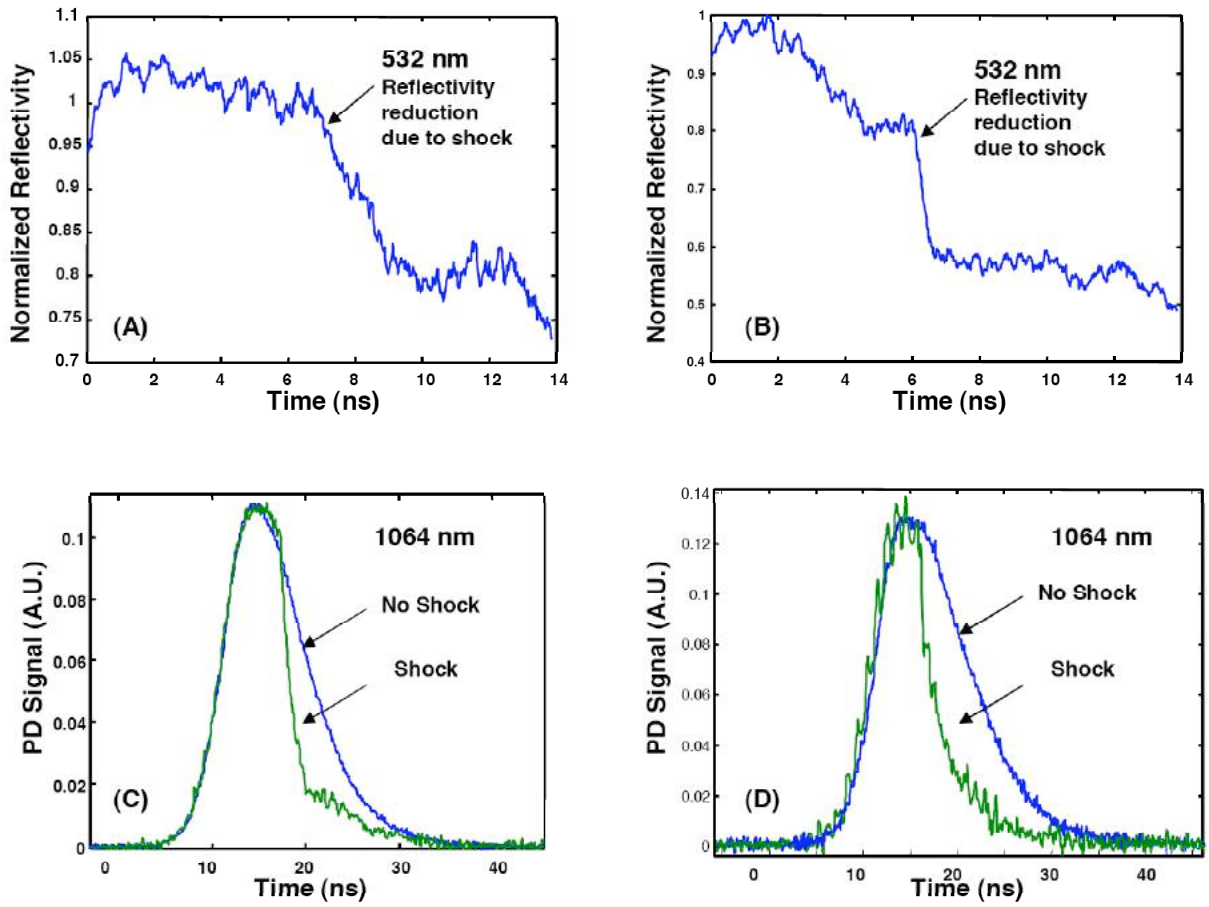

Figure I.D.7: (A) and (C) are reflectivity measurements from VISAR (532 nm) and fast photodiode (1064 nm), respectively, for the same 76 J shot shown in Fig. 4. (B) and (D) are the same measurements, but for the 196 J shot shown in figure I.D.5.

shot. These trends may be explainable by the migration of the resonance in aluminum as it experiences different temperature and pressures. Increasing temperature moves the resonance toward the red, but increasing pressure moves it toward the blue. The resonance disappears upon melt, and we expect to see similar reflectivity rate changes for both wavelengths. Indeed, both 532 nm and 1064 nm reflectivities change in under 5 ns for the 196 J pulse. This indicates that shock-melting is at least being approached for the stronger laser pulse. As seen in figure I.D.7, there is more noise in the photodiode signal of the 196 J shot. This is a consistent problem of the more energetic shots, and in future work we will electrically shield the cables and diodes.

I.E Spall Experiments on the Z-Beamlet Laser

Participants:
*A. Dalton W. Grigsby, A. Bernstein, J, Brewer, E. Taleff, and T. Ditmire (**University of Texas**)*

In addition to the investigation of phase changes in laser driven shocks, we are also interested in studying the spall strength of materials subject to high strain rate loading by a laser. In

particular, we are investigating the process of laser-induced spallation on the Z-Beamlet Laser at Sandia National Laboratory. We have developed a number of diagnostics for these experiments at Sandia.

For our spallation experiments Z-Beamlet (ZBL) light at 527 nm produces a shock wave by laser ablation of the front surface of a planar target. The shock propagates through the sample toward the rear surface of the target. In addition to using ZBL as the shock driver, long pulse and short pulse optical probes view the rear side of the material. The long pulse probe is a line-VISAR (Velocity Interferometry System for Any Reflector) whose design is illustrated in figure I.E.1. This design is based on the LLNL design of Celliers which is presently fielded on the Janus laser there [1]. In addition to VISAR we have implemented a short pulse (sub-picosecond) probe. The short pulse probe is a 2D reflectivity/interferometry diagnostic, which is used to take a snapshot of the rear surface of a target.

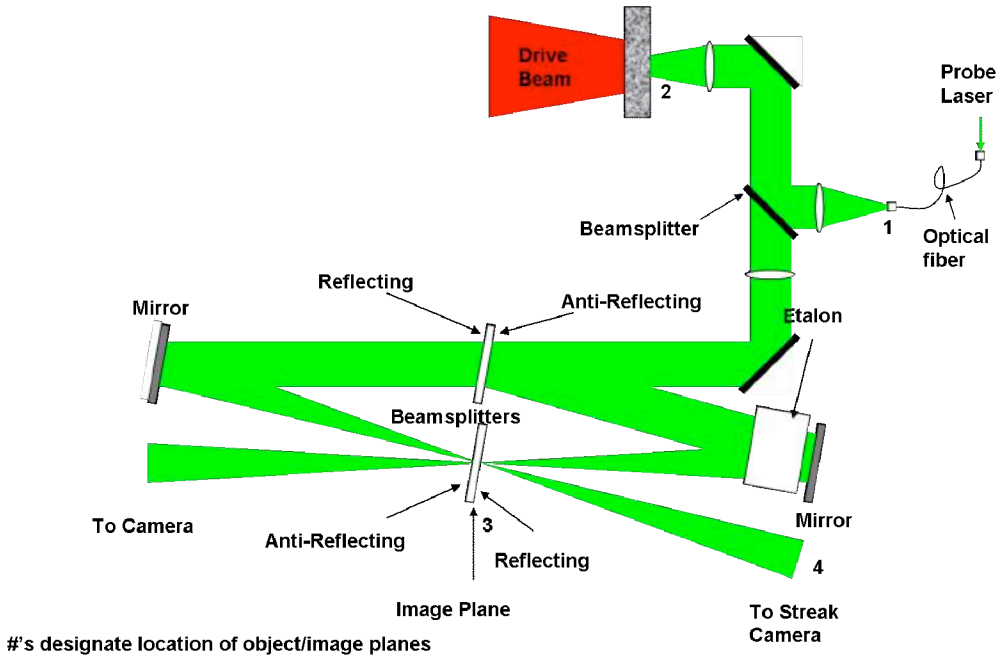

Figure 1. The figure above is a schematic of a line-VISAR system.

A focused laser intensity of ~10^{12} W/cm^2 (pulse length of 1.8 ns) is delivered onto several hundred microns of a free standing, planar target produces a shock wave that upon reflection from a free surface becomes a tensile wave. If the tensile wave meets a failure criterion specific to the material for some loading rate, the result is spallation (planar failure) of the material.

The tensile stress (or spall strength, P_{spall}) at the spall plane is determined from the first maximum and first minimum in the free surface velocity profile.

$$P_{spall} = \frac{1}{2}\rho_0 c_s (u_{\max} - u_{\min}) \quad \text{where } u_{\max} - u_{\min} \text{ is pullback velocity}$$

The strain rate for each shot was approximated from the free surface velocity profile.

$$\dot{\varepsilon} \approx \frac{\Delta u}{\Delta t} \cdot \frac{1}{2c_s}$$

The laser providing the probe pulses for the VISAR in our experiment had a limited time duration which limited the temporal window over which we could observe the free surface motion. In order to see the entire spall event, we designed a pulse stacker that triples the length of the original VISAR probe pulse. The design involves two half-waveplates and a polarizing beamsplitter, shown in figure I.E.2. The waveplates allow us to control the intensity of the pulses exiting the cavity. The round trip cavity time needs to be about the same as the pulse length of a single pulse in order to get a long, relatively constant intensity pulse. The output stacked VISAR pulse is shown in figure I.E.3. This pulse train enters an optical fiber which negates the fact that two different polarizations exit the pulse stacker.

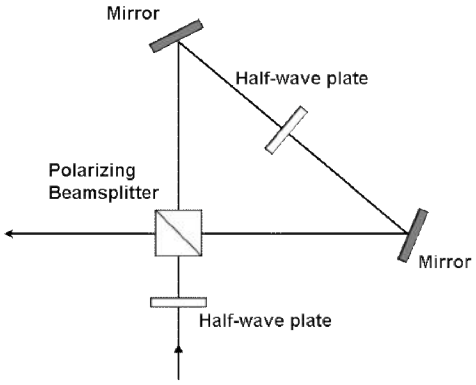

Figure I.E.2. Schematic illustrating the pulse stacker used to effectively triple the VISAR pulse length.

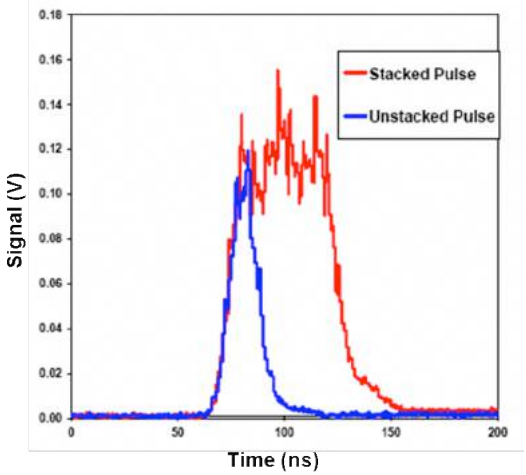

Figure I.E.3. Photodiode trace of a single pulse and a stacked pulse.

We are currently performing experiments to measure the spall strength of various materials such as 99.999% Al, Al+3% Mg (annealed), and Al+3% Mg (cold-worked). We want to study these materials because they have properties that are similar (mostly aluminum); however, they have properties that are also different (absence versus presence of second phase particles, etc.). We want to observe how the spall strength changes with the type of material and how the recovered samples compare to each other.

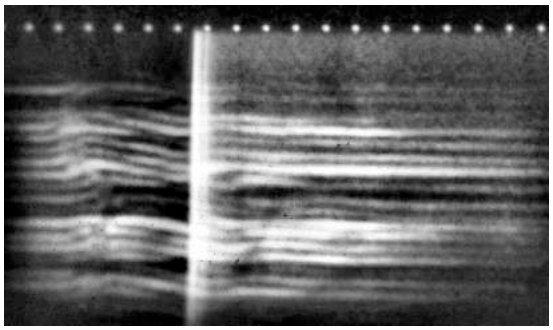

Figure I.E.4. Line-VISAR interferogram for a spall experiment of 200 _m of free standing Al + 3% Mg impacted at 4x10^{11} W/cm^2. The velocity per fringe constant is 0.29 km/s/fringe. The separation of the timing fiducials is 2 ns.

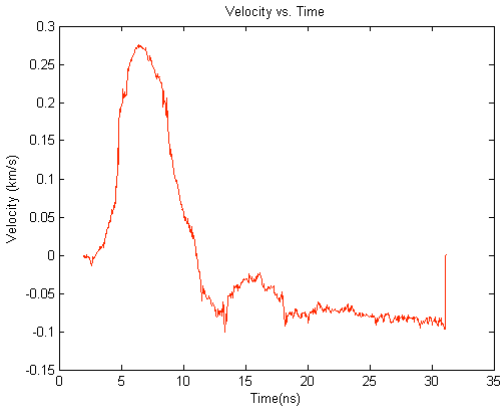

Figure I.E.5. Above is a lineout of the velocity corresponding to the interferogram on the left. The pullback velocity for this shot is 0.35 km/s. (Note: Analysis is ongoing to determine the material density and bulk sound speed of our various targets.)

Figures I.E.4 and I.E.5 show a line-VISAR interferogram and velocity profile for one of our spalled samples. In order to determine the absolute velocity after shock breakout, two VISARs with different velocity sensitivities are necessary to eliminate the ambiguity in the number of fringe shifts. Absolute velocity is not essential to determine the spall strength of a material since spall strength depends on the pullback velocity.

In these experiments, the short pulse diagnostics allow us to derive a 2D snapshot of the rear surface of a target. This is useful in examining shock breakout uniformity.

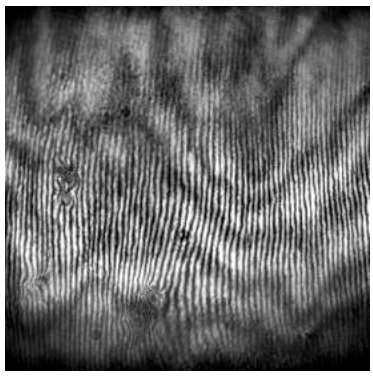

Figure I.E.6. The reference image above is from the short pulse displacement interferometer.

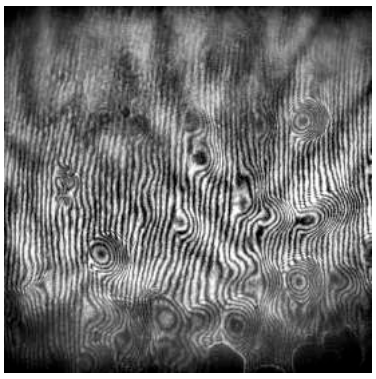

Figure I.E.7. This short pulse displacement interferogram shows the rear surface of a spall target shortly after shock breakout.

Figure I.E.6 shows a reference 2D displacement interferogram and figure I.E.7 shows an interferogram shortly after shock breakout. The short pulse diagnostics can be used to answer questions about the phase of the pump beam and target characteristics, such as surface flatness and parallelism.

In addition to collecting dynamic information about the target, we have recovered spalled samples from recent experiments. Preliminary analysis shows a contrast in the different types of fracture that occur in our samples during the spall process. We see vastly different behavior for materials that have similar properties. Figures I.E.8 and I.E.9 illustrate features of ductile and brittle fracture from collected post-mortem samples.

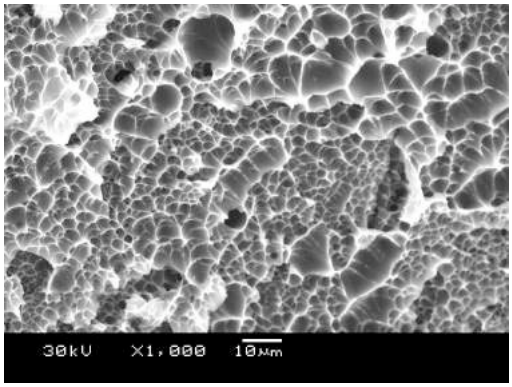

Figure I.E.8. The above SEM image shows the spalled surface of a high-purity annealed aluminum target. The dimpling is indicative of ductile fracture.

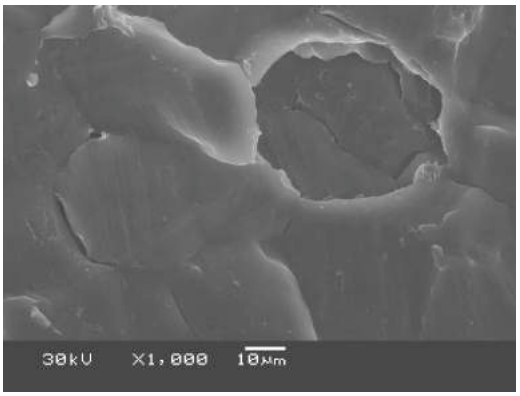

Figure I.E.9. The above SEM image shows the spalled surface of a Al+ 3% Mg target that has been slightly cold-worked. The sharp edges and score marks indicate that the fracture is less ductile.

References for section I.E

1. Celliers, P.M., *et al. Rev. of Sci. Inst.* 2004, **75**, 4916.

I.F Portable diagnostic development for time-resolved studies of phase transformations in materials under laser induced shock-loading

Participants:
*D. Milathianaki, A. Doulton, W. Grigsby, T. Ditmire (**University of Texas**)*
*H. Lorenzana, J. Hawreliak, J. Colvin (**Lawrence Livermore National Lab**)*

Some members of TCHILS are involved in an LLNL Strategic Initiative LDRD project at LLNL on laser driven shock wave phase changes. For this project we are responsible for developing a compact, transportable VISAR which can be fielded at a number of facilities. We will also be involved in the dynamic x-ray diffraction (DXRD).

In this collaborative effort with LLNL, we aim to study the dynamics of phase transformations in single and polycrystalline materials such as Al, Si, Bi etc. undergoing laser induced shock-melting (and possibly re-freezing). Temporal information on the phase transformations will be provided via time-resolved DXRD, whereas VISAR will be the means to verify the shock-drive across the sample. Simultaneous DXRD and VISAR is an extremely useful diagnostic and something that has been implemented only very recently at LLNL.

We were involved in a series of preliminary experiments at LLNL led by Hector Lorenzana. Preliminary experiments at the JANUS facility of LLNL have accomplished the following goals:

1. Troubleshoot single x-ray backlighter sources (Ti, V)
2. Test a dual backlighter technique utilizing a single backlighter foil being irradiated twice by double pulse or two backlighter foils being irradiated once by temporally separated single pulses
3. Simultaneously implement DXRD and VISAR. The sample in all cases has been Si single crystal. Sample data from the x-ray diffraction is illustrated in figure I.F.3 (supplied by H. Lorenzana).

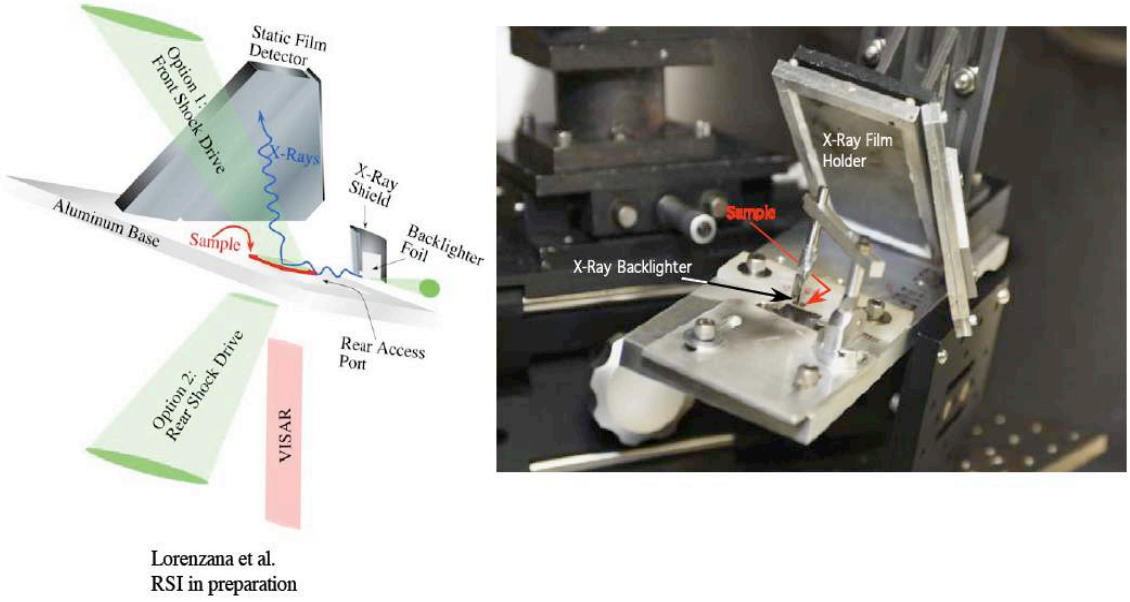

Figure I.F.1. Diagram of simultaneous DXRD and VISAR for shock-driven targets at JANUS. Photo showing actual setup of sample, backlighter, x-ray film holder.

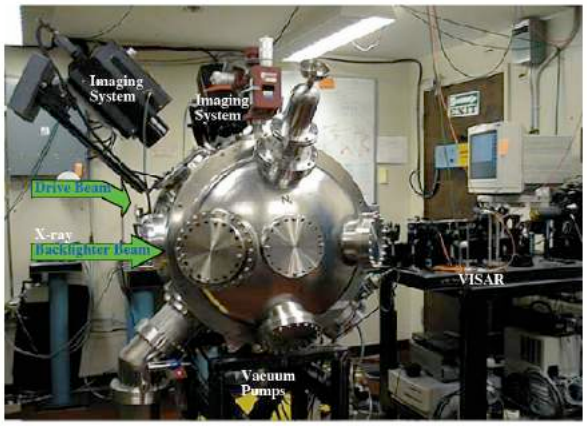

Fig. I.F.2. JANUS target room at LLNL. Backlighter and drive beams are shown. Part of the optical setup of the LLNL VISAR is also indicated.

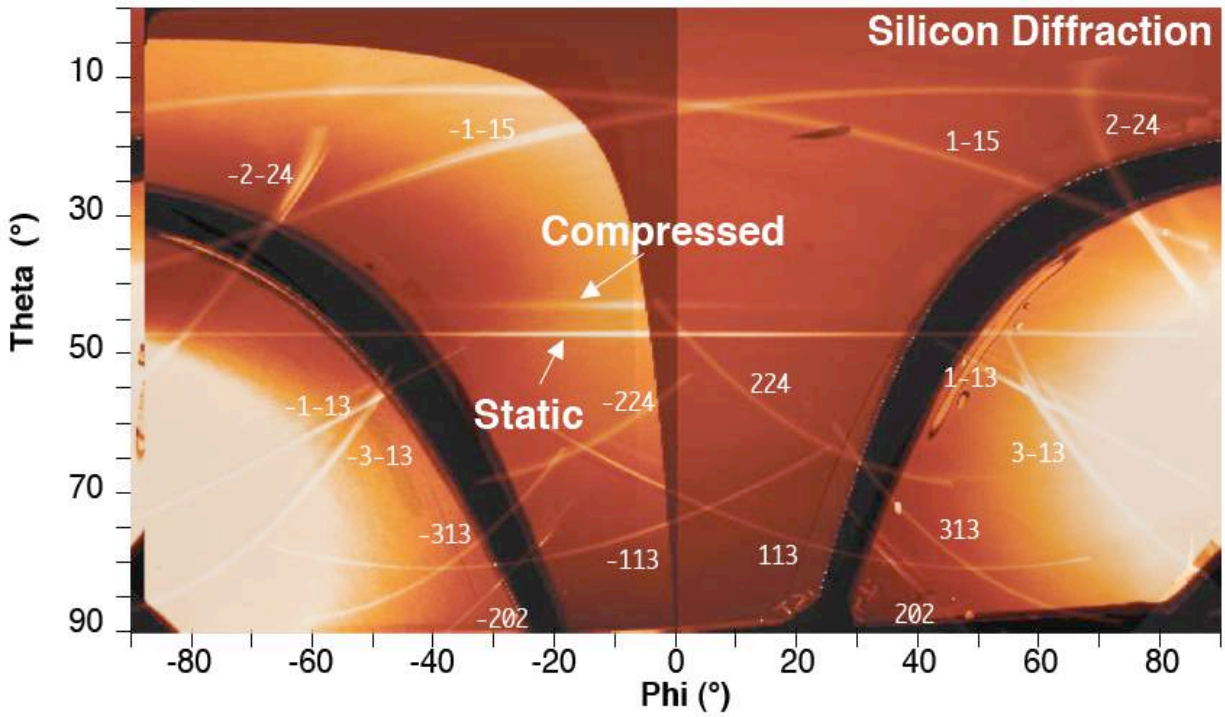

Figure I.F.3. Example data from Si sample showing diffraction from static and compressed lattice planes. (Lorenzana et. al.)

VISAR is the primary instrument for the measurement of the particle/shock velocity across the sample during shock-loading experiments. We are currently constructing a portable VISAR to be used at synchrotron facilities, where DXRD can be performed with monochromatic and highly directional x-ray beams. Such beams are of critical importance in DXRD of polycrystalline samples undergoing shock-loading.

A schematic of the VISAR under construction is shown in figure I.F.4.

The milestones we expect to accomplish in the coming months are:

a) Complete VISAR construction and installation at a synchrotron facility, most likely APS (Advanced Photon Source).
b) Investigate shock-melting in several single-crystal materials. Bismuth is a good candidate since both melting and re-solidification under shock-loading can be studied.
c) Determine good candidate materials in which the dynamics of shock-melting can be temporally resolved.

Troubleshoot polycrystalline DXRD technique.

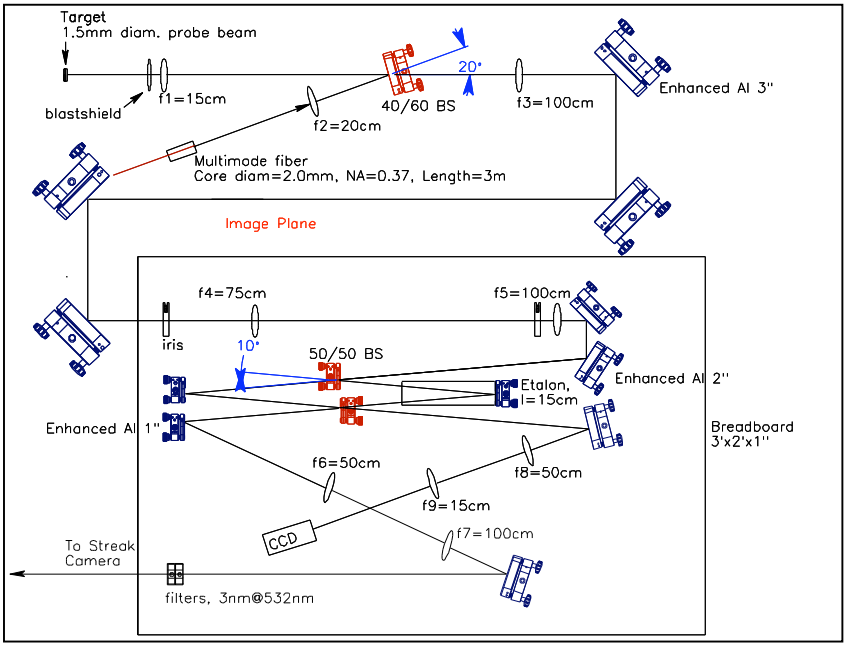

Figure I.F.4. VISAR schematic

I.G Materials science in support of laser driven shock experiments

Participants:
*J. Brewer, A. Dalton, T. Ditmire and E. Taleff (**University of Texas**)*

While the principal thrust of our shocked materials effort in TCHILS is aimed at developing optical diagnostics for laser driven shocks, we have begun a significant materials science effort here at UT to complement the dynamic diagnostics. This effort is led from the Mechanical Engineering Department here at UT by Prof. Eric Talleff.

During the past year in this aspect of the TCHILS effort we have developed the facilities for target fabrication and characterization. We are now capable of manufacturing free standing targets with thicknesses from 30 μm and up with optical quality finishes. Thinner targets are likely possible if the need arises. Our characterization capabilities include analyzing whole targets and cross sections.

In order to fabricate thin metallic foils, a pack-rolling technique was developed. In pack rolling, a small piece of any ductile material is placed in a folded stainless steel pack and reduced in thickness by feeding the pack through a precision rolling mill. By monitoring the foil's integrity, adding lubricants, periodically changing the pack, and heat treating at intermediate steps, the ductile material can be reduced in thickness many times. Foils have been successfully created from aluminum, magnesium, aluminum alloys, gold, and indium.

Before the manufactured targets are used in testing, the targets are measured to determine thickness and surface finish quality. The thickness can be measured in three ways: by direct mechanical measurement; analysis of target cross sections; and derivation from known area, mass, and density. The surface finish is measured using an optical profilometer; the available profilometer measures height deviations (profile) over a maximum area of 3.5mm by 4.7mm. A custom data analysis software package has been developed to characterize target surface profiles at different wavelengths by using a Gaussian filtering technique. This method allows for quantitative measurement of error of geometric form, waviness, and surface roughness. This information is used to characterize fabricated targets and to benchmark pack-rolling techniques.

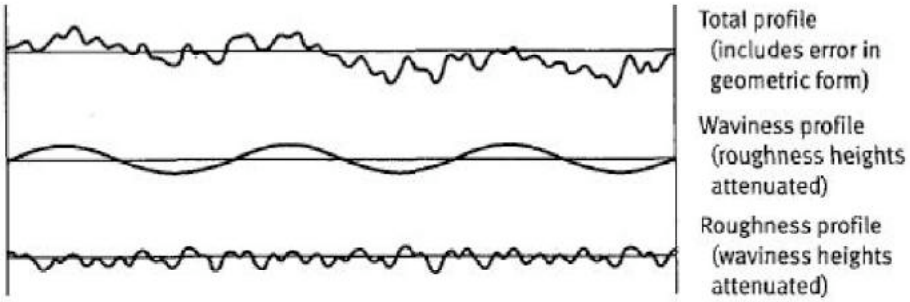

Figure I.G.1: Schematic showing the filtering of a surface profile into waviness profile and roughness profile. The cutoff wavelength for differentiation between waviness and roughness can be set using the developed software package. (Image taken from ASME standard B46.1)

Post shot analysis has been performed on a number of laser driven targets shot by the Sandia Z-Beamlet laser. Microscopy is used to characterize the surface of shot targets. These images allow measurement of spall area, can reveal the effects of laser intensity variation, and are used to characterize fracture/spall surfaces. The data obtained can be used to identify the initiation points of spall failure, for example.

Figure I.G.2 Overview of a shot target showing the spall surface (dull area). The effect of laser intensity variations are seen from small sections of the target that did not spall.

By sectioning the targets we can measure spall thickness as well as observe microscopic features within the targets. Characterization of the cross sections of targets fabricated by Sandia National Laboratories reveals a large population of intermetallic particles. These particles are possible nucleation sites for spall, which could lower spall strength compared to high-purity aluminum targets. By using energy dispersive x-ray spectroscopy (EDS), these particles were shown to be

rich in iron and silicon. Similar characterization of targets fabricated in house from high-purity aluminum showed no intermetallic particles.

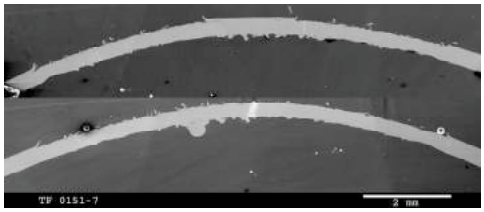

Figure I.G.3 Example cross-sectional image of a shot target. The spall surface is toward the top of the image. On the top half of the image, the spall was not complete; laser intensity variations led to the flat, unspalled surface. Spall thickness can be measured by comparing the thicknesses of the target where spall did and did not occur.

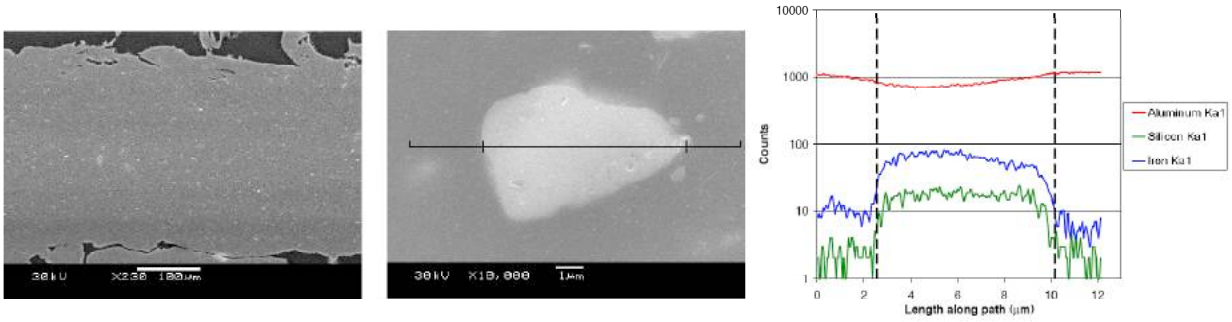

(a) (b) (c)

Figure I.G.4 Images showing the intermetallic particles observed in the Sandia targets. (a) Low magnification shows the dispersion of particles. (b) A highly magnified image of a single particle. The black line shows the path of the EDS line analysis shown in (c). (c) The dashed lines depict the edges of the particle. The composition of the particle is high in both iron and silicon.

I.H Molecular dynamics simulations of high strain rate shocks

Participants:
*M. Lane and M. Marder (**University of Texas**)*

In support of our tin shock experiments, we have also undertaken a simulation study of shocks in tin. We use molecular dynamics (MD) techniques developed at UT Austin in the Center for Nonlinear Dynamics. This part of our effort leverages the extensive expertise in the CNLD in various complex phenomena in materials and the MD simulations developed there over the past few years to model crack propagation.

MD simulation of shockwaves in model systems was established in the early 80's and ever-larger computations are bound only by the computing power of the day. MD study of shocks requires large computational facilities, since long-time shock simulations require large amounts of material to be simulated. The problem does not easily allow for small systems to run for long

times, or large systems to run for short times. Success in the field has been found by pushing forward with multi-million atom simulations on the nation's largest parallel machines.

Our simulation focus has been on the shock front, a relatively small neighborhood at the interface between compressed and uncompressed material. Our interest is in the transitions at this front, and how they depend on the forcing parameter for the shock wave. Our studies are demonstrating that we can simulate conditions at the front without the large system sizes usually necessary to study long-time shock propagation.

We employ a moving window technique in which only a small portion of the physical system is simulated. To accomplish this, we are constantly feeding fresh material to the system, and purging compressed material from behind the shock. The concept of a moving analytical window for studying shockwaves was first proposed by Klimenko and Dremin [1] as a means to time average fluctuations in a small system. Zhakhovskii, et al. [2] later improved on this method, but relied on - without fully describing - a ``special potential'' which functioned as a permeable piston at the back surface. Our purge criterion and purge method are based on firm principles of shock theory and statistical mechanics. The basic idea is to ensure that material behind the shock front has sufficiently approached thermodynamic equilibrium in the moving frame. So long as this condition obtains, discarding material should have little effect upon shock dynamics.

In our simulations crystalline material far ahead of the shock front is unperturbed by the shock, because shocks travel faster than any wave in the uncompressed material, and because our interatomic potential is short-ranged. Thus, neither direct particle interaction nor wave interaction can influence particles more than 10 Angstrom ahead of the front, We limit our simulation size by adding particles only as they come within a buffer zone >50 angstrom from the shock front. We add complete unit cells when we paste particles onto the front of the sample, and the front edge of the simulation is constrained to prevent unphysical surface reconstruction.

The code [3] used for this work is developed and maintained at the University of Texas at Austin. It has been applied to nonequilibrium problems in fracture, friction and shock simulation. The code is spatially parallel for scalability. We use classical molecular dynamics with an effective interatomic potential. The equations of motion are integrated by the Verlet method with a timestep of 0.3 femtoseconds. Temperature is monitored but not externally controlled. Shock waves are generated by moving an infinitely massive piston (momentum mirror) at a constant velocity into an initially stationary material. The piston velocity is the independent variable. In all of our runs, the tin crystal is oriented so that the shock runs along the [100] direction.

The Modified Embedded Atom Method (MEAM) of Daw and Baskes is used to model the atomic interactions. We employMEAM parameters due to Ravelo, et al. [4] which were determined by fitting structural, transitional and melt properties with experimental values to within 11%. Our simulations vary in size, with a minimum cross section of 5x5 units cells. Periodic boundary conditions are imposed in the directions transverse to shock motion. Particle numbers in our preliminary runs have been small, ranging from thousands to tens of thousands. In all cases simulations run until transients die away, requiring more than 10,000 timesteps in

every case.

As a compressive shock wave propagates, it converts pristine material ahead into denser material behind. Long shock simulations require large amounts of material to be simulated, although the shock front constitutes only a small part of the entire system. Our moving window technique simulates only the particles in the neighborhood of the moving front by adding material ahead of the shock only as needed, while purging from behind the shock when derived physical criteria are met.

The shock front is undisturbed by crystal ahead of it, and the crystal far enough ahead is unperturbed by the shock front. These statements hold because shocks travel faster than any wave in the uncompressed material, and because our interatomic potential is short-ranged. Thus, neither direct particle interaction nor wave interaction can influence particles more than 10 Angstrom ahead of the front, We limit our simulation size by adding particles only as they come within a buffer zone >50 angstrom from the shock front. Particles are added as complete unit cells, and the front edge of the simulation is constrained to prevent unphysical surface restructuring.

We contend that under many conditions particles behind the shock front can also be removed from the simulation. Here, there is no argument that waves cannot influence the front, since shocks are always subsonic in the compressed material. So, we must limit ourselves to steady state fronts. In these cases, we have developed a simple criterion for when material at the back edge can be purged.

Consider a material through which a perfect one-dimensional shock front is propagating. Take the shock as an abrupt change in ρ the density, and u the particle velocity. If a right-traveling disturbance moves with speed U, then one can balance the mass entering the region of abrupt change (the shock front) from the right with the mass leaving the region on the left.

In a given time Δt, the mass entering the region on the right is given by the product of the density and the volume flux into the region. The volume flux is given by the product of A the cross sectional area the relative velocity of the shock front, u_0-U, and Δt the time interval. Using the well known jump conditions [4] for a shock front we can form a simple physically meaningful criteria for purging material from the back surface. Thus, as the shock front propagates through our system, it's position is periodically calculated. This position is first compared to the front boundary of the system. If the shock front has entered the buffer zone, then a unit cell thickness of particles are added to the system ahead of the shock front. At each of these add events, the system's back boundary is also evaluated for a purge. If the average conditions within a volume equal to the volume just added satisfy the purge criterion, this volume is removed from the system and the porous piston is advanced. Such that, if an add and purge event occur simultaneously then the total system volume would remain constant and the number of particles in the system would decrease.

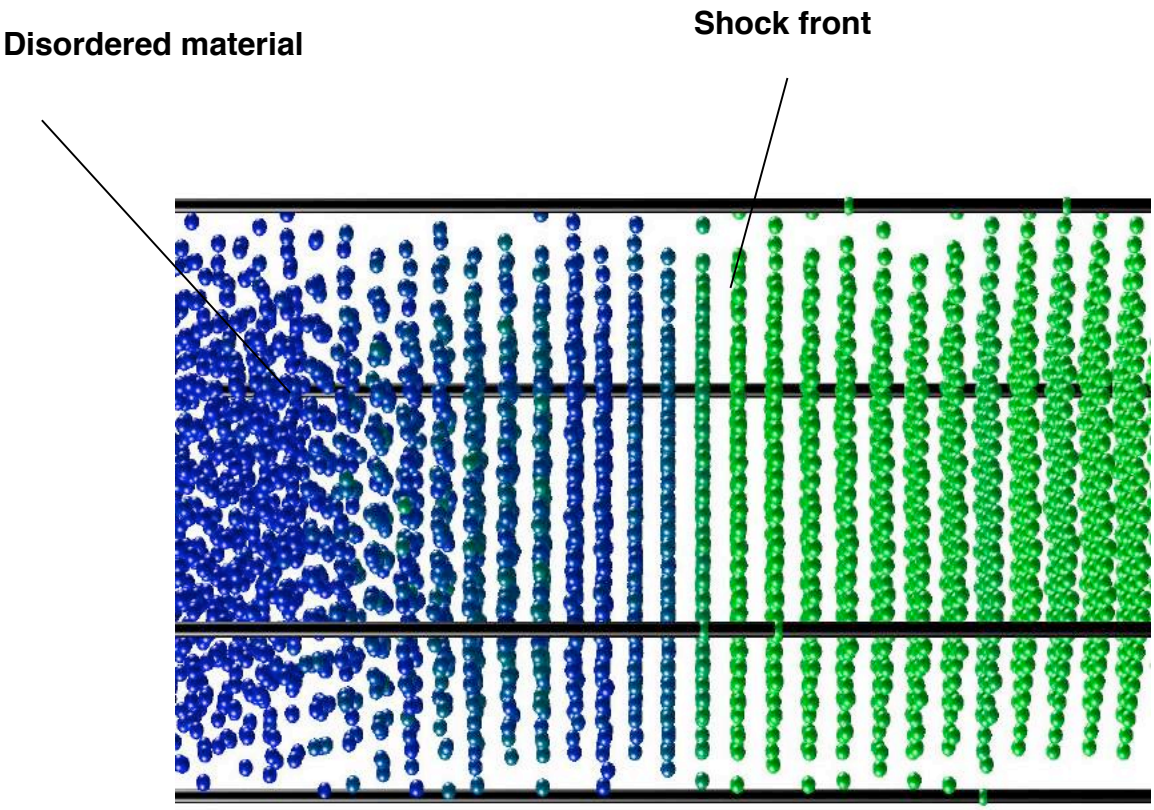

Figure I.H.1: Image of a simulated shock in a tin lattice. Color of the particle denotes the energy.

We have performed preliminary simulations on tin. One result is illustrated in figure I.H.1. We find that our simulations agree well with published Hugoniot data on tin, validating the potentials used in our simulations. A comparison of the Hugoniot derived in our MD simulations is compared to tine Hugoniot data in figure I.H.2.

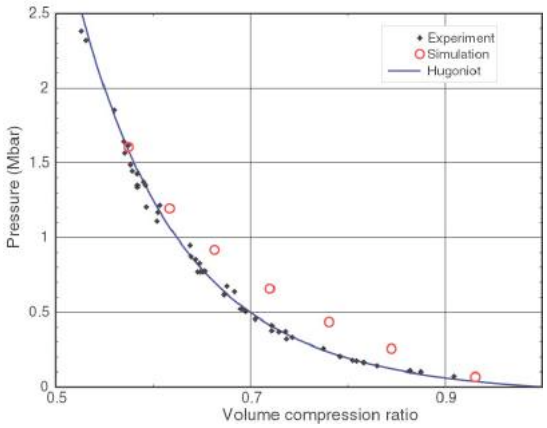

Figure I.H.2 Comparison of simulated tin Hugoniot points with data points

There are two major difficulties with applying traditional simulation methods [7,8] to the study of the dynamics near the shock front: (1) To produce the environment at the front, one must simulate a large and ever-growing system, of which the front constitutes only a very small fraction; and (2) The conditions within a steady-state shock take long times to arise, and each computationallyexpensive shock run results in only a single data point.

The constrained dynamics methods of the Hugoniostat and others [9.10] over a solution to the first issue, but provide no information about non-equilibrium dynamics at the shock front that would be needed to compare with experiments. The approach of Zhakhovskii et al. [2] succeeds in addressing the first point at the shock front, but does not address the second. We generalize and expand on their methods. First, we concentrate our efforts on the neighborhood of the shock interface, thereby increasing computational efficiency, and second, we map system response to a continuum of shock strength final states in a single run. These, combined, constitute the

Our simulation method makes the Hugoniot the thermodynamic path of our simulation system. This has not been possible experimentally. Figure I.H.3 contrasts the experimental loading paths (Rayleigh lines) to each state of the Hugoniot and the loading path which we will use to reach the same state points.

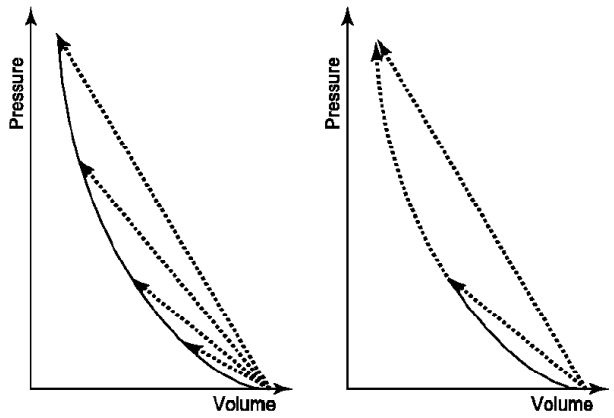

Figure I.H.3: (left) The Hugoniot, as collection of final shock states; and (right) as the state-to-state path of the Continuous Hugoniot Method.

We outline our simulation method in four stages: Benchmark – We begin each simulation with a traditional shock wave computation. This initial long duration, full-system run is allowed to continue to its final shock steady state. This steady state is our first point on the shock Hugoniot and serves to seed our subsequent computations. In figure I.H.3 this is represented by the lower Rayleigh line from the initial state to the beginning of the Hugoniot ramp.
Reduce – We truncate the system to a fixed width neighborhood around the front by removing particles which are beyond a set distance behind the shock front. We impose a warm impactor (piston) boundary condition and match the thermodynamic statistics at the rear purge point using a strong Langevin thermostat. A buffer of pristine material is preserved ahead. The length of the reduced system is determined by the system's thermalization length. The piston driving velocity

and mean velocity of the thermostat are equal, and this value, *vp*, serves as the external control parameter for shock strength.
Shock strength ramp – To this reduced system, we introduce a quasistatic increase of the shock forcing parameter. The goal is to increase the shock strength, while always maintaining a direct mechanical coupling between the forcing at the piston and the response at the shock interface. The piston velocity increases by a set amount per timestep. The temperature of the stochastic forcing is updated every purge to match the distribution at the purge point. The point of forcing always remains a set distance behind the shock front. This process continues until the shock strength parameter has reached its terminal value.
Terminal benchmark comparison – Finally, a second benchmark run is made with a shock strength matched to the final value of the shock strength ramp. This allows the final state of the Hugoniot ramp to be compared directly to a traditional shock run to identify any problems and to serve as an error check.

The validity of our purge technique assumes that the back of our system is in equilibrium. We verify this by velocity distribution analysis before we reduce the system. We assume our shocks are always in steady state. This is guaranteed, so long as our ramp loading is quasistatic. If so, the small changes have time to equilibrate across the entire system and the driving and response are mechanically coupled. If not, then the foundation of the Hugoniot-Rankine equations is eroded, and off-Hugoniot states are produced.

The essential property of this method is our ability to very slowly ramp the shock strength parameter while maintaining correct thermodynamic conditions at a roughly constant distance behind the front. This is not currently achievable in experiment. Instead, in experiments driving forces are imposed at ever-increasing distances. If one ramps the driving velocity in an experimental situation, the result is isentropic compression rather than a shock response.

We can estimate an upper bound for the quasistatic ramp rate of the shock strength control parameter. The velocity is scaled by units of the wave speed of the compressed material, CS , and the time is scaled by the return time of the acoustic waves in the system, $2L/CS$. We, thus, get the nondimensional condition for a quasistatic ramp.

$$\dot{\tilde{v}}_p = \frac{d\tilde{v}_p}{d\tilde{t}} = \frac{d(v_p/C_S)}{d(t/\frac{2L}{C_S})} \ll 1 \quad \Rightarrow \quad \frac{dv_p}{dt} \ll \frac{C_S^2}{2L}$$

Note that the upper bound for quasistatic ramp rate goes to zero for large systems. The advantage of the method is lost when systems are too large.

As a prelude to more realistic but computationally intensive studies, we test these ideas with the Lennard-Jones potential, which has a well-documented solid shock response [5,7]. We use the cubic-spline Lennard-Jones 6 – 12 potential [6] in order to allow easy comparison with published Hugoniot results of Germann et al. [11]. The shock was oriented along the <100> direction of the fcc crystal with unit cell dimension 5.314 Å =1.561σ. Initial temperature was varied with a weak Langevin thermostat from zero to 10K = 0.083 kB T/ε. Results are found not to depend on the initial temperature for shock driving velocities, v_p above 0.75 C_o. Systems were 20 x 20

lattice planes in cross-section with transverse periodic boundary conditions. The timestep was 0.3 femtoseconds.

The traditional shock simulation runs (benchmark runs) were driven by a warm impactor and reached 600 Å in length (100,000 particles). Continuous Hugoniot Method runs were held to 200 Å in length (20,000 particles), at any one time. The cumulative distance covered by these treadmilling runs was almost 1.3 μm in length, and would have required over 1,200,000 particles in a conventional simulation. Every shock was given time to establish a steady state (usually 30 to 60 ps). The ramp rate of 0.001 m/s per step = 3.3×10^{12} m/s^2 is used for the remainder of this article. We report on our efforts in the strong shock regime, for driving velocities ranging from $v_p = 0.75\ C_o$ to $1.5\ C_o$.

The Continuous Hugoniot Method allows a system to move directly from one shock state to another. Therefore, the path of our Continuous Hugoniot Method through *Us –vp* space during a single run is the principal Hugoniot of final shock states in the material. This is true to the extent that there is quick convergence within the reduced system to the values far behind the shock. Figure I.H.4 shows such a path for a simulation which runs from $v_p = 0.75\ Co$ continuously through $v_p = 1.5\ C_o$. Initial and terminal benchmark runs, bookend the ramp. The Hugoniot fit proposed by Germann et al. is plotted in its applicable range.

We see excellent agreement of our method's results with both comparisons. In the lower range of *vp*, where we can compare to the published fit, our data overlays the fit very nicely and continue it smoothly beyond the range for which it was originally published. At higher shock strengths our data stiffens (as it should), showing a super-linear increase in *US* vs *vp*. In the upper range of *vp*, we compare to our terminal benchmark results, which also agree well.

Figure I.H.4 shows a series of four density profile snapshots taken from a continuous Hugoniot ramp (shown as solid lines). They are at $vp = 0.75\ C_o$, $0.9\ C_o$, ,$1.2\ Co$ and $1.5\ Co$. The density profiles of the two benchmark runs and the final densities predicted by the Hugoniot fit for $0.75\ C_o$ and $0.9\ C_o$ are plotted.

The profiles produced by the Continuous Hugoniot Method agree well with the results of the benchmark runs up to the point where they are purged. The benchmark densities, however, continue to grow beyond this point. In both cases the density predicted by the published fit is approximately 2% larger than the average final density produced by the Continuous Hugoniot Method.

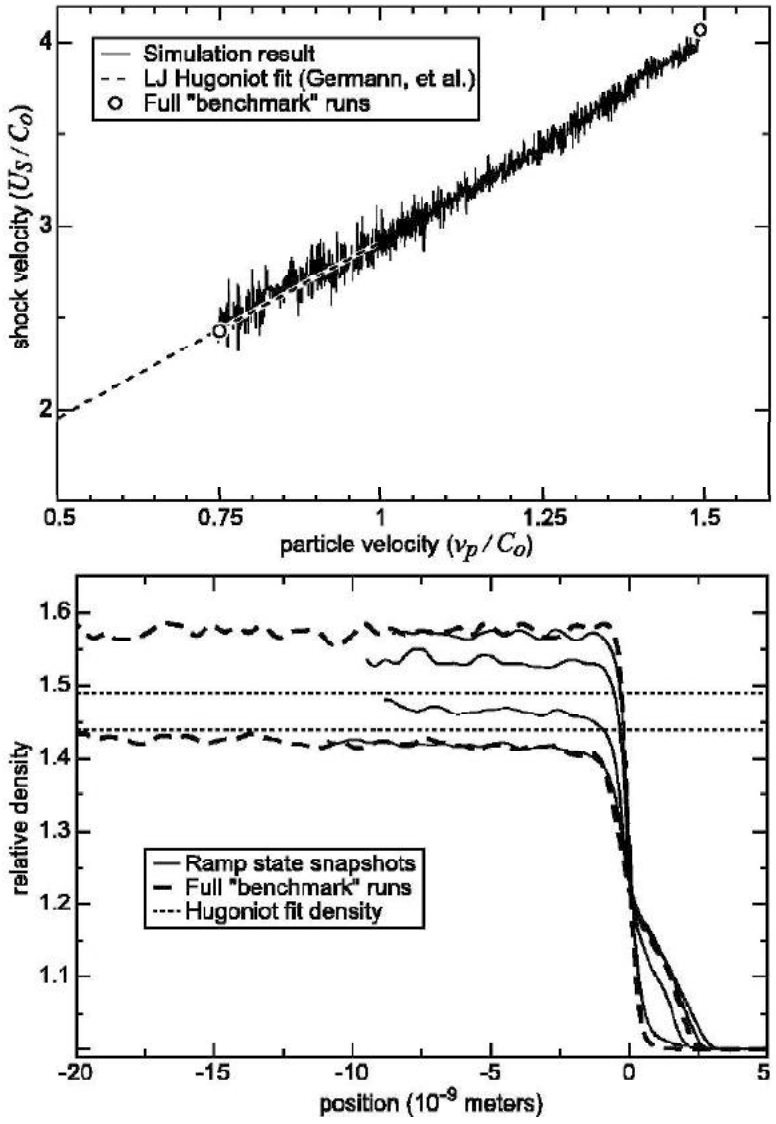

Figure I.H.4: (top) Results of the Continuous Hugoniot Method, the fit of Germann et al. [?], and bookend benchmark runs. (bottom) Density profiles snapshots from a shock strength ramp (solid), from the initial and terminal benchmarks (dashed), and from the Hugoniot fit (dotted).
to converge completely to its asymptotic value.

The final state of the Hugoniot ramp is a particularly important point of comparison because it is the state of the maximum integrated error. Figure I.H.5 provides snapshots from the terminal benchmark (top) and the Continuous Hugoniot Method (bottom). The slices are along the x–z plane at the final piston velocity $v_p = 1.5\ C_o$. Both systems exhibit a strong disordering transition on similar length scales, islands of incomplete disordering, and a common sharp density rise. Both have also developed forward-reaching features ahead of the front. Figure I.H.5, shows very good agreement between the radial distribution functions for the material behind each front.

The computational speedup provided by the Continuous Hugoniot Method depends upon the

density of points with which one wants to locate the Hugoniot. We find that the computation time to compute two benchmark runs by traditional methods is approximately equal to the computation time we employed to compute the entire intermediate Hugoniot, via our method. Thus if we had chosen to trace out the Hugoniot by interpolation with 10 conventional shock computations, we would have required 5 times more computation. More generally, let N_h be the number of traditional runs needed to map the Hugoniot between two states as a function of shock strength. Then the speed up is linear in N_h, given roughly by $N_h/2$. Alternatively, we point out we were able to simulate the cumulative effect of 1,280,000 particles with the resources required to hold only 20,000 at any one time.

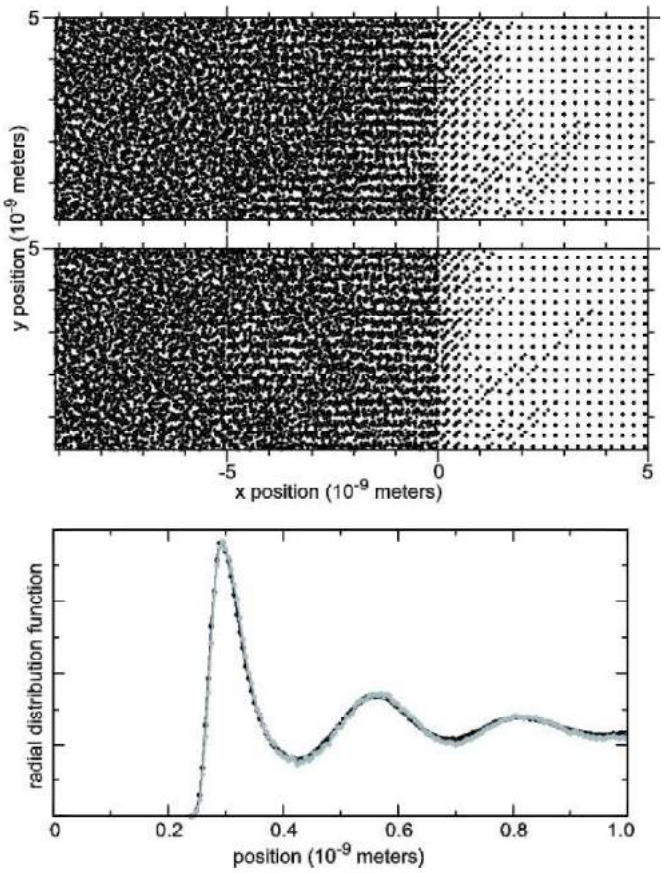

Figure I.H.5: Structural dynamics and rdf comparison – Particle slicesin the region of the shock front for states from (middle) the Continuous Hugoniot Method and (top) the terminal benchmark. Also shown (bottom) is a comparison of radial distribution functions for the compressed material extending 10 nm behind each front. $v_p = 1.5\ C_o$.

References for section I.H

1. V. Yu. Klimenko and A.N. Dremin. Soviet Physics Doklady, **25(4)**:288--289, (1980).
2. V. V. Zhakhovskii, S. V. Zybin, K. Nishihara and S. I. Anisimov, Phys. Rev. Lett. **83,** 1175 (1999).

3. B.L. Holian, et al., and R.~Ravelo, M.D. Furnish et.al., editor Shock Compression of Condensed Matter - 1999, pages 35--41. AIP Conference Proceedings, 1999.
4. Y. B. Zel'dovich and Y. P. Raizer, *Physics of Shock Waves and High-Temperature Hydrodynamic Phenomena*, (Academic Press: 1967).
5. B. L. Holian. Atomistic computer simulations of shock waves. Shock Waves,**5**:149{157, 1995.
6. B. L. Holian, A. F. Voter, N. J. Wagner, R. J. Ravelo, S. P. Chen, W. G. Hoover, C. G. Hoover, J. E. Hammerberg, and T. D. Dontje. Effects of pairwise versus many-body forces on high-stress plastic deformation. Physical Review A, **43**(6):2655-2661, March 1991.
7. Brad Lee Holian and Peter S. Lomdahl. Plasticity induced by shock waves in nonequilibrium molecular-dynamics simulations. Science, **280**:2085-2088, Jun 1998.
8. K. Kadau, T. C. Germann, and P. S. Lomdahl. Large-scale molecular dynamics simulation of 19 billion particles. International Journal of Modern Physics C, **15**:193-201, 2004.
9. J. B. Maillet, M. Mareschal, L. Soulard, R. Ravelo, P. S. Lomdahl, T. C. Germann, and B. L. Holian. Uniaxial hugoniostat: A method for atomistic simulations of shocked materials. Physical Review E, **63**:16121, December 2000.
10. Evan J. Reed, Laurence E. Fried, and J. D. Joannopoulos. A method for tractable dynamical studies of single and double shock compression. Physical Review Letters, **90**(23):235503, June 2003.
11. Timothy C. Germann, Brad Lee Holian, and Peter S. Lomdahl. Orientational dependence in molecular dynamics simulations of shocked single crystals. Physical Review Letters, **84**(23):5351-5354, June 2000.

I.I Warm Dense Matter Studies on the LLNL JanUSP/Callisto Laser at LLNL

TCHILS has a number of projects devoted to study of heated plasmas at high density. Many of these studies are being conducted in anticipation of the activation of the Texas Petawatt in a couple of years.

The short pulse laser systems at TCHILS, LLNL and Sandia enable the study of warm dense matter WDM [1] through the technique of isochoric heating. While shock heating of solids is currently the more refined technique of gathering equation of state (EOS) data in the WDM region, the technique only accesses a limited region of state space [1], namely on the principal Hugoniot. Direct isochoric heating, followed by measurements along a release isentrope will be an important complimentary technique for EOS measurements [2]. Isochoric heating experiments performed on the Texas Petawatt laser will expand on current experiments at LLNL, in which the heating mechanism is a laser-accelerated proton beam. While WDM temperatures are easily achieved through direct laser heating of a thin foil [3], isochoric heating over more than a laser skin depth (e.g. several nm) requires a penetrating source, such as protons, x-rays [1, 4], or electrons. That a solid target could be heated to WDM temperatures by a laser generated proton beam was seen in separate experiments at LLNL by measurement of self-emission [5] and free expansion into vacuum [4] of a proton heated target. The current experiment uses these two diagnostics simultaneously to connect pressure with temperature and internal energy of isochorically heated WDM, thus measuring the equation of state.

In past years within this NNSA Center, we have examined x-ray isochoric heating via laser generated x-rays (see report last year). We have found that insufficient x-rays were produced on either our THOR laser or the LLNL JanUSP laser to yield secondary target temperatures of above 1 eV. Consequently, during the past year we have explored the potneital of using short pulse generated proton beams for heating. This approach builds off of successful experiments that were performed at LLNL in which a proton bam generated by JanUSP heated a target to >10 eV as determined by the target's self emission. We wish to extend this experiment by implementing the active optical probing techniques that we have developed previously on JanUSP for the x-ray heating experiment. Optical probing can yield heated target reflectivity (related to conductivity) as well as target release velocity (related to material EOS).

Current experiments are performed on the Calisto (formerly JanUSP) laser at Lawrence Livermore National Laboratory (LLNL). A high contrast, 100fs pulse at 800nm is delivered with up to 10J on target. For our purposes, a below-maximum intensity of $1x10^{18}$ W/cm^2 in a ~90μm diameter spot is ideal. The laser interacts with a 20μm thick Si source foil with a mirror-like rear surface from which high-energy protons are accelerated [6]. Spaced 75μm from the back surface of the source foil is a 10μm thick Si sample foil to be heated by ultrashort proton pulse. The rear surface of the sample foil is also mirror-like, allowing for a reflecting probe beam.

The scheme of our experiment is depicted in figure I.I.1. For each shot, the probe beam provides an interferometric image of the sample rear surface at a precise delay after heating. Also, self-emission from the heated region is collected, split, filtered at two specific wavelengths, and focused onto a 3ps resolution streak camera as a diagnostic of the temperature [5]. Finally, radiochromic film (RCF) stacks are used to measure the energy spectrum of protons penetrating the sample, to determine deposited internal energy [7].

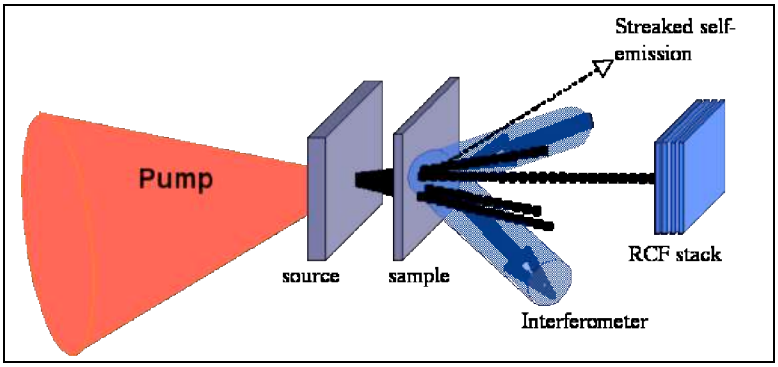

Figure I.I.1 Basic experimental scheme. Protons accelerated from the back surface of a source layer of Si heat a nearby sample layer to several eV. Interferometry, proton dosimetry, and a time-resolved self-emission diagnostic are employed.

A similar target geometry was employed to isochorically heat Al to near-WDM temperatures using K_a x-rays [4]. Although laser conditions were optimized for x-ray rather than proton production and most images were taken at early times before the arrival of protons at the sample,

some images were taken with sufficient delay to see the effects of proton heating, as shown in figure I.I.2. The expanding heated region was well-localized with a very clean profile.

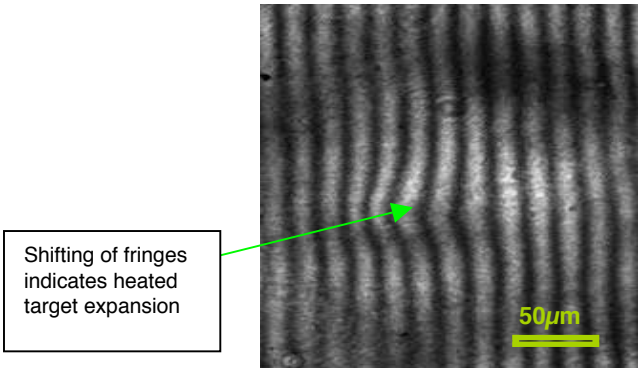

Figure I.I.1: An example interference image of the back surface of a proton-heated sample from a previous campaign. Left-bending interference fringes in the center of the image indicate the rear surface expanding into vacuum at a set delay relative to the pump pulse. A half-fringe shift 5ps after proton heating suggested a temperature of over 1eV [4].

References for section I.I

1. Lee, R.W., et al., *Finite temperature dense matter studies on next-generation light sources*. Journal of the Optical Society of America B (Optical Physics), 2003. **20**(4): p. 770.
2. Foord, M.E., D.B. Reisman, and P.T. Springer, *Determining the equation-of-state isentrope in an isochoric heated plasma*. Review Of Scientific Instruments, 2004. **75**(8): p. 2586-2589.
3. Widmann, K., et al., *Interferometric investigation of femtosecond laser-heated expanded states*. Physics Of Plasmas, 2001. **8**(9): p. 3869-3872.
4. Dyer, G., et al., *Isochoric heating of solid aluminium with picosecond X-ray pulses*. Journal Of Modern Optics, 2003. **50**(15-17): p. 2495-2505.
5. Patel, P.K., et al., *Isochoric heating of solid-density matter with an ultrafast proton beam*. Physical Review Letters, 2003. **91**(12): p. 125004.
6. Allen, M., et al., *Direct experimental evidence of back-surface ion acceleration from laser-irradiated gold foils*. Physical Review Letters, 2004. **93**(26).
7. Breschi, E., et al., *A new algorithm for spectral and spatial reconstruction of proton beams from dosimetric measurements*. Nuclear Instruments & Methods In Physics Research Section A-Accelerators Spectrometers Detectors And Associated Equipment, 2004. **522**(3): p. 190-195.

I.J Fusion neutron generation studies from laser –irradiated clusters

Participants:
D. Symes, R. Hartke, F. Buergens, and T. Ditmire ***(University of Texas)***
*P. Patel, and D. Price (****Lawrence Livermore National Laboratory****)*

Within TCHILS we have an ongoing interest in the production of intense bursts of neutrons by short pulse laser driven deuterium fusion. Ultimately, we hope to field these kinds of experiments on the Texas Petawatt laser with the intent of producing enough neutrons to perform time resolved materials damage studies with the short pulse of neutrons acting as a pump. Consequently, we have put effort into understanding the yield scaling of neutrons with an eye toward ascertaining the scaling toward a petawatt. Much of the core of this work has been performed in recent years in collaboration with people from LLNL. We are now beginning to collaborate with simulation experts at Sandia as well on this project. Work within the Center during the last year has been an extension of our ongoing work in this area over the past few years.

The approach that we have been studying relies on the fact that very high ion temperature plasmas can be produced when an intense, femtosecond pulse irradiates a gas of van der Waals bonded clusters. When a gas of deuterium clusters is used as a target a plasma of sufficiently fast deuterium ions can be produced to drive DD nuclear fusion. The idea of these experiments is illustrated in figure I.J.1. A high intensity, ultrafast laser pulse is focused into a gas jet of deuterium clusters, creating a plasma filament with a diameter roughly that of the laser focus (~100 μm) and a length comparable to the extent of the gas jet plume (~ 2 - 5 mm). The fast deuterium ions ejected from the exploding clusters can then collide with ions ejected from other clusters in the plasma driving DD fusion and releasing neutrons from one branch of the fusion reaction, $D + D \rightarrow He^3 + n$, in which a neutron is released with 2.45 MeV of energy.

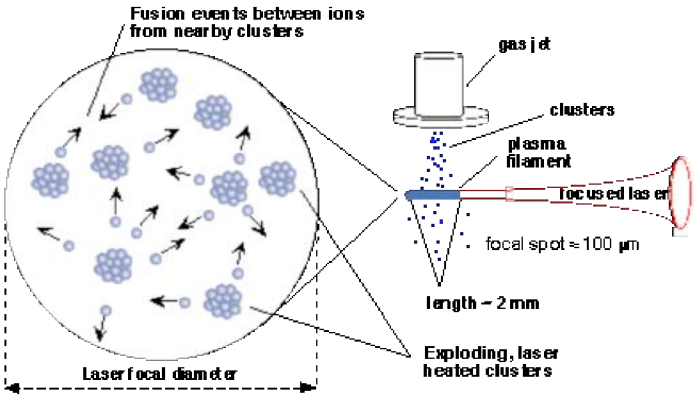

Figure I.J.1: Schematic of the deuterium cluster fusion experiment.

This fusion was first observed in cluster deuterium plasmas in initial experiments at LLNL where we observed up to ~ 10^4 DD fusion neutrons at 2.45 MeV per laser shot with roughly 100 mJ of laser energy focused to intensity of 10^{17} W/cm^2 [1]. The yield scaling with laser energy in these experiments is shown in figure I.J.2 (labeled "Falcon data"). Since the initial experiments reported in [2], we have characterized the scaling of the fusion yield to higher laser energy.

These results were gathered in the first year and a half of the NNSA SSAA contract. These experiments were performed in collaboration with LLNL. To do this yield scaling we used the LLNL JanUSP laser which delivered up to 10 J of energy in 100 fs pulses [3]. Data on the neutron yield from the irradiated cluster plume were acquired with an array of plastic scintillating detectors as a function of pulse energy for 100 fs and 1 ps pulse durations, results which are also shown in figure I.J.2. We find that the fusion yield increases rapidly with laser energy, increasing roughly as the square of the energy for all pulse durations [4]. During the past year, under support from the Center we can repeated these scaling experiments on the UT THOR laser. These data are also illustrated in figure I.J.2.

The fusion yield scaling in these experiments can be estimated by noting that the expected fusion neutron yield for the cluster gas jet experiment will be approximately: $N \approx \langle \sigma_{DD \to nHe} v \rangle n_i^2 \tau_{dis} V$ where n_i is the D^+ ion density (>2 x 10^{19} cm^{-3} in cooled jets), τ_{dis} is the disassembly time of the plasma, $\langle \sigma_{DD \to nHe} v \rangle$ is the velocity averaged fusion cross section (for the D+D→ He^3 +n reaction) and V is the plasma volume. The yield is directly related to the disassembly time of the plasma, which is, for the inertially confined plasmas of the experiments described above, roughly the time required for a deuteron to exit the plasma by free streaming across the filament diameter. Our observed fusion yield in all cases is consistent with equation above (where $<\sigma v> \sim 10^{-19}$ cm^3 s, $n_i \sim 10^{19}$ cm^{-3}, $\tau \sim 100$ ps and $V \sim 0.03$ mm^3 for 100 mJ shots implying a yield, N ~ 3 x 10^4 /shot). A large gain in yield could be derived if τ_{dis} could be increased.

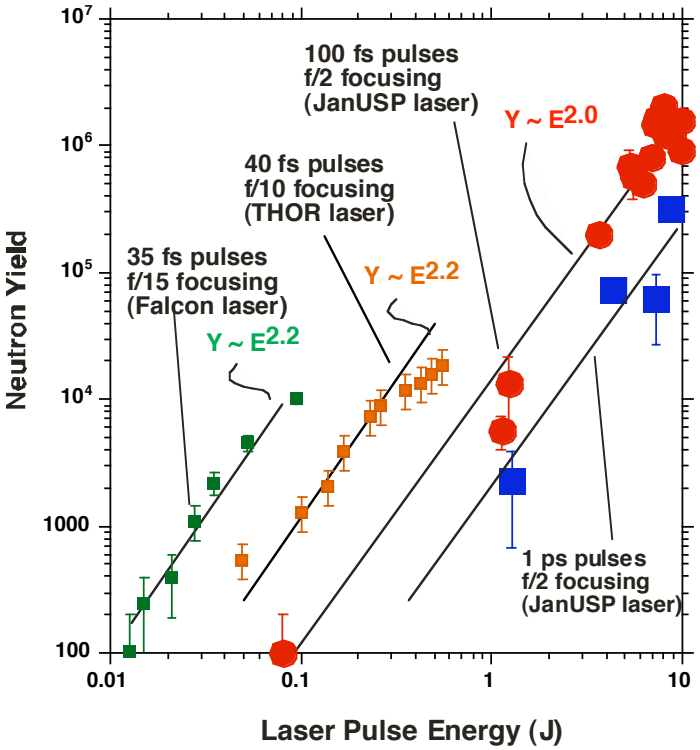

Figure I.D.2: Measured scaling of cluster fusion yield as a function of laser energy. These data were acquired with three different laser systems.

During this the past year, we concluded a series of studies of exploding mixed species CH_4 and CD_4 clusters. Heteronuclear clusters like deuterated methane are very interesting since these

mixed ion clusters may exhibit enhancements in ion energy through a dynamical effect in the Coulomb explosion. The Coulomb explosion of a single species cluster, like D_2 clusters, will eject deuterons with an energy given directly by the potential energy of the ion as it is initially in the fully stripped cluster. In exploding mixed ion clusters like CD_4 the light deuterons will outrun the heavier ions, explode in an outer shell with a higher average energy than would be expected from the naïve estimate of ion energy based on initial potential energy. This implies that the fusion yield could be substantially increased in plasmas formed from explosions of heteronclear clusters over that of neat D_2 clusters of the same size because of this kinematic enhancement of ion energies in the mixed ion case. We examined the explosion of CD_4 clusters and the fusion yield that results from these plasmas. Those experiments indicated that there was some enhancement of deuteron energies from CD_4 when compared to similar sized D_2 clusters.

This year, we followed up on these experiments motivated by a surprising result published recently by the LOA group in France [5]. This group reported what seemed to be a rather large (>40%) anisotropy in the neutron emission from exploding CD_4 cluster plasmas. This is unexpected if the pure Coulomb explosion model is at work since the clusters should eject ions nearly isotropically. We examined the angular distributions from these clusters using the THOR laser at UT and the apparatus illustrated in figure I.J.3. Here we examined the distributions of neutrons as a function of polarization angle in the laser polarization plan as well as a function of azimuthal angle in the plane of propagation. The French group reported a large peaking of the neutrons perpendicular to the laser propagation direction.

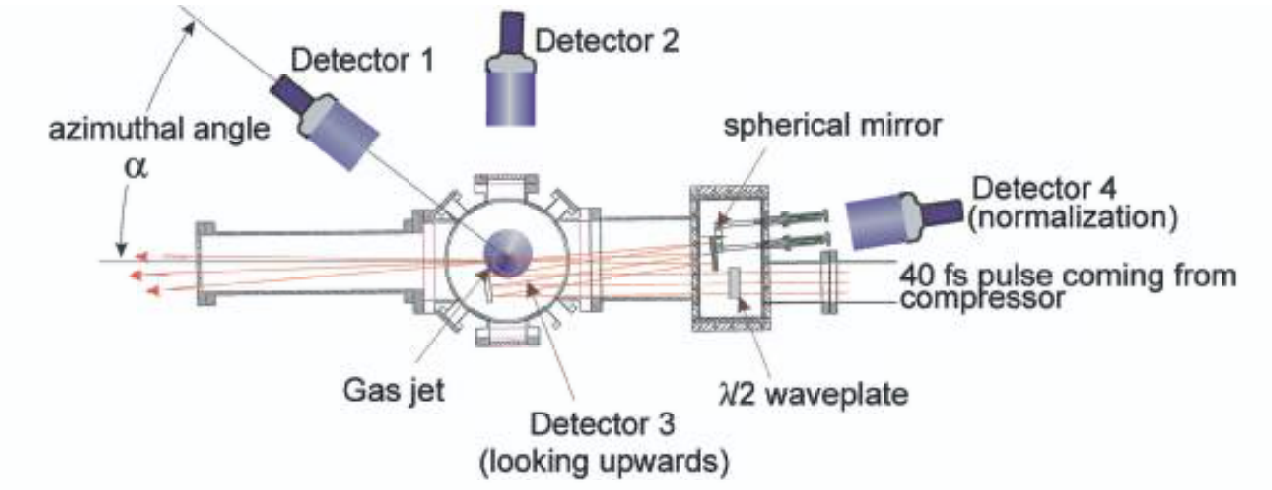

Figure I.J.3: Experimental set-up used for measuring the neutron angular distribution on the UT THOR laser.

Our results are quite at odds with the French results. We find, first that there is nearly completely uniform neutron emission with polarization angle. We do observe a slight anisotropy in the azimuthal plane. This is illustrated with the data shown in figure I.J.4. Here the neutron emission from a CD_4 cluster plasma, irradiated with 0.5 J of a 40 fs laser pulse is shown. The cluster sizes are around 10 nm per cluster. We see a small peaking of the neutron emission in the

forward and backward direction (ie along and and back against the laser propagation axis). This anisotropy is much smaller than reported by the LOA group and is in a direction different than they see. We believe that our result is, in fact, completely in keeping with the Coulomb explosion picture of the cluster explosion, and that the slight neutron peaking can be explained by the cigar shaped plasma filament geometry of the plasma. A detailed explanation of these results as explained by detailed Monte Carlo particle simulations will be presented in a paper about to be published.

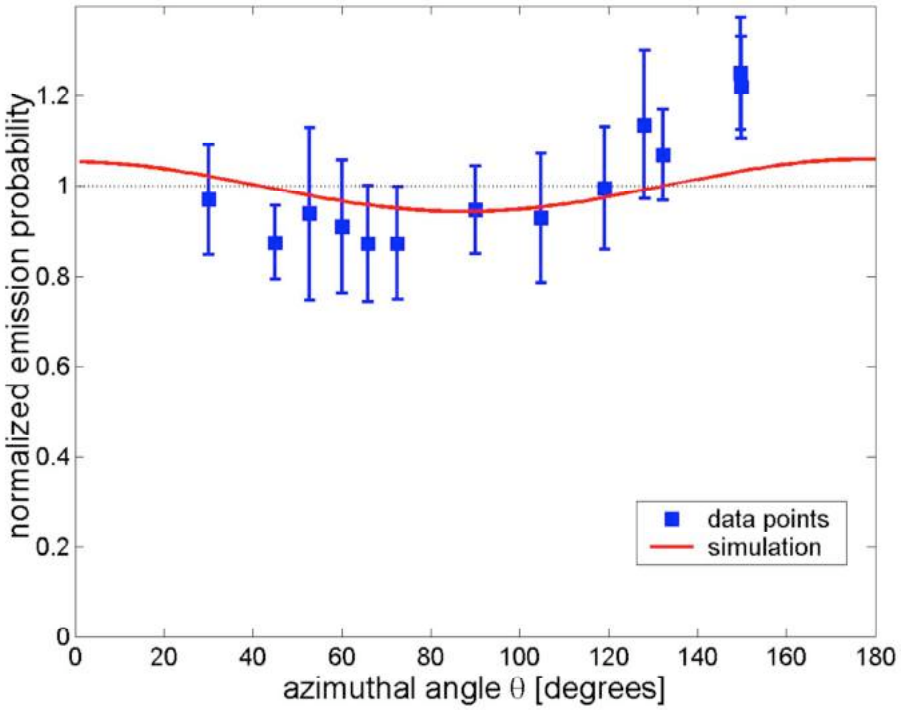

Figure I.J.4: Azimuthal scan of neutron yield from CD_4 clusters carried out by an angular scan of 'Detector 1' shown in Figure I.J.3.

References for section I.J

1. T. Ditmire, *et al.*, , *Nature* **398**, 489 (1999).
2. J. Zweiback, *et al.*, , *Phys. Rev. Lett.* **84**, 2634 (2000).
3. J. D. Bonlie, F. Patterson, D. Price, B. White, and P. Springer, *Appl. Phys. B-Lasers Opt.* **70**, S155 (2000).
4. K. W. Madison, R. Fitzpatrick, P. K. Patel, D. Price, T. Ditmire, *Phys. Rev. A*
5. G. Grillon, *et al.*, *Phys. Rev. Lett.* 89, art. no.-065005 (2002).

I.K K-alpha x-ray production studies at the UT THOR laser

Participants:
*G. Dyer, B. Cho, D. Symes, and T. Ditmire (**University of Texas**)*
*S. Gaillard, Y. Sentoku, T. Ohkubo, N. LeGaulladec and T.E. Cowan (**University of Nevada, Reno**)*
*R. Shepherd, H. Chen, K. Widmann (**Lawrence Livermore National Laboratory**)*

Within TCHILS we have an interest in developing bright K-alpha x-ray sources. The motivations for doing this include a desire to produce x-rays with enough intensity to heat a secondary target for warm dense matter studies and desire to produce a bright x-ray backlighter source. Both motivations will ultimately see utilization on the Texas Petawatt laser and, perhaps, Z-Petawatt at Sandia. We also have a new interest in proton production (explained in more detail below) for similar applications.

K-alpha x-rays and proton beams can be readily produced with a multi-terawatt laser focused onto a simple thin foil. In this case, the source size is quite small (<1mm), but can be considerably larger than the laser focal spot size [1]. Where greater concentration of the source is desired, alternate target geometry may be capable of guiding absorbed energy in the form of hot electrons interacting with the electromagnetic fields of the laser into a smaller volume, improving concentration and intensity. This is the concept behind using conical targets, which are studied for their application to fast ignition [2]. Utilizing target geometry in this way holds the possibility of generating a source that is superior for many applications.

Since cone targets are difficult to produce and expensive to buy, our study a year ago focused on an analogous but much simpler to produce target geometry: The pyramidal, or square-based cone geometry. In the experiments reported here, these pyramid targets are irradiated with the 20 TW THOR laser and the x-ray, electron and proton source characteristics are studied with a variety of diagnostics. Our experiments were performed on the THOR laser using up to 700mJ of 800nm laser light on target in a 38fs laser pulse that was focused to a spot of less than 10μm in diameter, yielding intensities of over 10^{19}W/cm^2 available on demand. Diagnostics included proton and electron spectrometers, x-ray pinhole cameras, a Faraday cup, and a six-channel hard x-ray spectrometer.

A major aspect of these studies has been the development of novel, cone shaped targets with very sharp tips (with tip sizes smaller than a wavelength). We have developed guiding structures such as pyramidal and wedge shaped targets made from silicon. Sub-micron tips of negative pyramids are etched anisotropically into silicon wafers. After etching, the thickness of the silicon wafer is less than 1 μm at the tip of the guiding structure. Titanium foils are adhered to the backside of the wafer. In the case of pyramid target, the laser is interacting with two pairs of opposing walls. In the case of a wedge, the interaction is restricted to one pair of opposing walls. Hence, a wedge can be regarded as a two-dimensional pyramid. This geometry is designed to investigate polarization effects of micro shaped targets by rotating the orientation of the target with respect to the polarization of the laser.

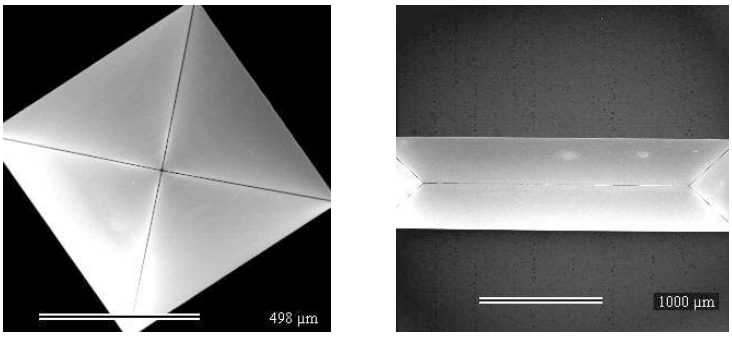

Figure I.K.1. SEM images of pyramid (left) and wedge (right) target which are etched in silicon wafers.

Based on our silicon fabrication techniques, free-standing gold pyramid targets were developed by Nano-mechanics group at University of Nevada at Reno. After creating positive pyramids on silicon wafer, a thick gold layer was deposited. Separating the gold from the substrate, free-standing gold pyramids with the same geometric condition as the silicon pyramids could be obtained.

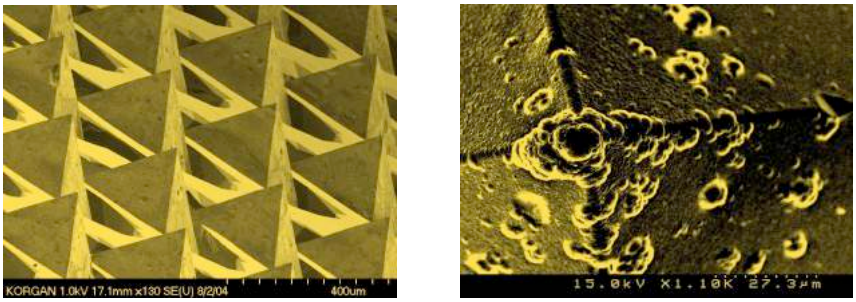

Figure I.K.2. SEM images of silicon pyramids fabricated on silicon wafer (left) and the free-standing gold pyramid target which are separated from silicon pyramid. (right)

We have conducted experiments irradiating these targets using the THOR laser. X-rays above 2.5 keV were imaged using pinhole camera with beryllium filter. The titanium K_α emissions were measured using both a von-Hamos and a spherical crystal x-ray spectrometer. Hard x-rays were also measured using a six-channel hard x-ray spectrometer (0.1 ~ 2 MeV). Additional diagnostics are scheduled for implementation in early 2006, including an electron spectrometer and an x-ray penumbral imaging camera.

A spherical crystal x-ray spectrometer was used to image the $K\alpha_1$ emission from flat titanium foils. The emission was compared to silicon pyramid and wedge targets backed with titanium foils. Figure I.K.3 is the 1D spatial image of $K\alpha_1$ emissions from these targets. Flat target data show side peaks and broad plateau around the main peak; however, images from the pyramid and wedge targets show no side structure.

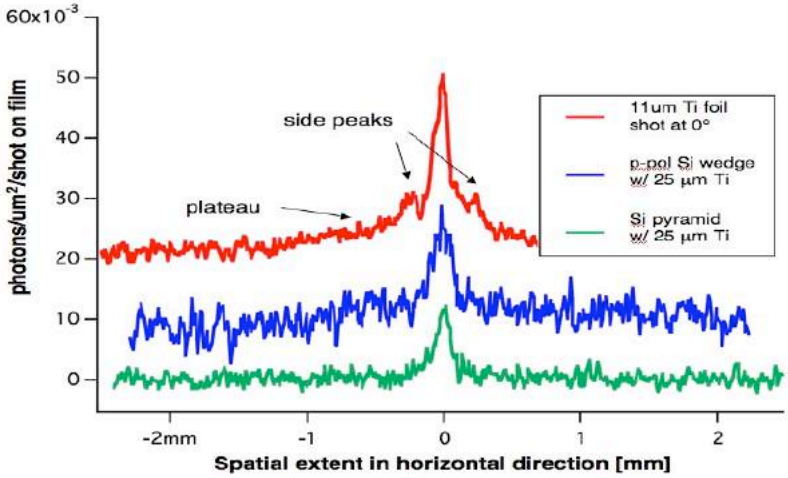

Figure I.K.3. $K\alpha_1$ emission from 11μm flat Ti foil and Si wedge and pyramid targets with 25μm Ti foil adhered to back surfaces. The foils were shot with the laser being incident at normal. Pyramid targets were shot along the pyramid axis of symmetry and wedges were irradiated with p-polarized laser.

A von-Hamos spectrometer was employed for comparing $K\alpha_1$ and $K\alpha_2$ x-ray yields from various targets. Figure I.K.4 shows that $K\alpha$ emission from flat targets is greater than from shaped targets. Among shaped targets, s-polarized wedges generate more $K\alpha$ photons than p-wedges and the pyramid shaped target is intermediate in x-ray yield. Considering Titanium $K\alpha$ photon energy (~ 4.5 keV) and the ponderomotive electron energy in our laser intensity (I=10^{19} W/cm^2), the electron temperature from each target is too high for optimal K shell ionization. In this regime, the higher the electron temperature, the less $K\alpha$ photons would be generated.

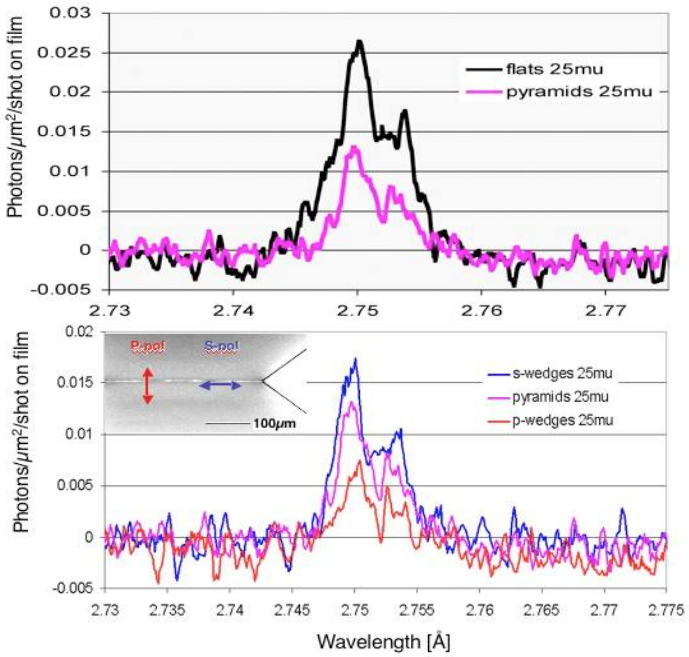

Fig. I.K.4. $K\alpha_1$ (left) and $K\alpha_2$ (right) peaks from a von-Hamos spectrometer. For flat and pyramid targets, laser-shot conditions were the same as Fig 3. For wedge targets, both p- and s-polarized laser lights were irradiated. Inset informs the laser polarizations in wedge targets.

We have also investigated the very energetic (MeV) photon regime in which x-rays are produced by bremsstrahlung emission. A combination of scintillator / photomultiplier detectors with various cut off filters was utilized for comparing the hard x-ray yield from p and s-polarized wedges and pyramid targets. Figure. I.K. 5 shows the highest hard x-ray yield for p-polarized wedges and the lowest yield for s-polarized wedges. These results inform an enhancement of very energetic (MeV) electrons for p-polarized wedge targets. $K\alpha$ photon yields and this hard x-ray data suggest the higher electron temperature for the p-polarized wedge than s-polarized wedge as well as shaped targets than flat target. All of these are also in accordance with the PIC simulations by Y. Sentoku, which predict a higher electron temperature for the p-polarized wedge than s-wedge. Our results also suggest anisotropic energy transport in the cone targets for fast ignition.

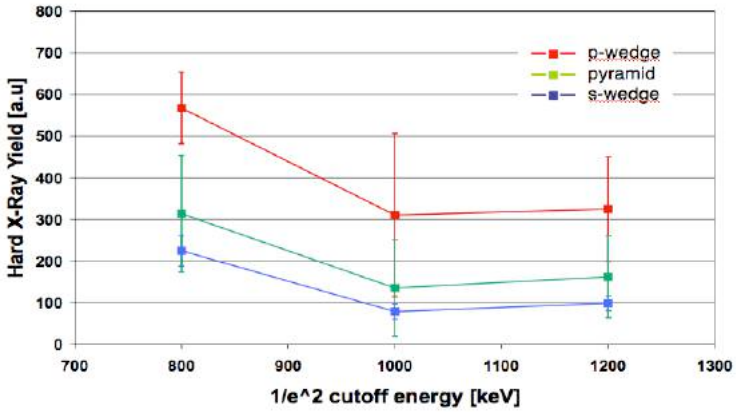

Figure I.K.5. Hard x-ray yield from p and s-polarized wedges and pyramid targets. P-polarized wedge has highest hard x-ray yield around 1MeV and s-polarized wedge has the lowest. Pyramid is a combination of p and s polarized wedges, resulting in a medium yield.

Finally, X-ray emission from 10μm thick free-standing gold pyramids was imaged with a pinhole camera. The emission was compared to flat gold foil with the same thickness. The pyramid target was shot along the pyramid axis of symmetry and flat foil was shot at normal. We could observe both an enhancement in overall signal as well as a sharper peak in the region of x-ray emission for the pyramid targets as compared to plain flat targets. This is illustrated in the pinhole camera images of figure I.K.6.

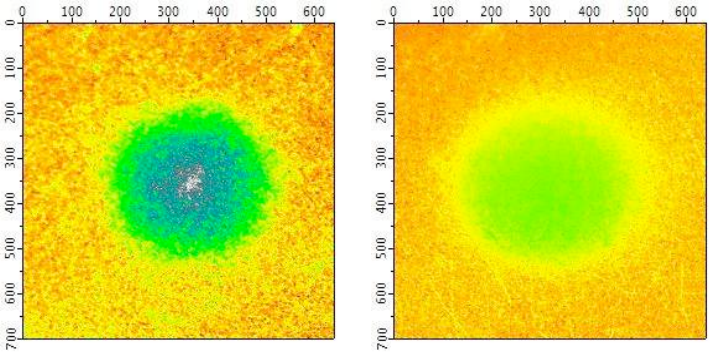

Figure I.K.6. Pinole images of x-ray emission from 10 µm free-standing gold pyramid (left) and simple flat gold foil of the same thickness (right). X-rays below 2.5 keV are excluded by a Be filter. Pinhole is 10µm diameter. Units are in microns; images are in false colors to enhance the contrast.

References for section I.K

1. R. B. Stephens, et al. Phys. Rev. E. **69**, 066414 (2004)
2. Y. Sentoku, H. Ruhl, Y. Toyama, R. Kodama, T. E. Cowan, Phys. Plas **11**, 6 (2004)

I.L X-ray generation from sphere targets

Participants:
*D. R. Symes, H. A. Sumeruk, I. V. Churina, and T. Ditmire (**University of Texas**)*
*T. D. Donnelly (**Harvey Mudd College**)*

In addition to exploring the use of cone targets for x-ray production, we are exploring other, unique targets for x-ray production. In particular, we have begun a campaign in the Center to study hot electron generation and x-ray production from targets coated with microspheres. This work is motivated by the possibility that spheres with size comparable to the wavelength of the incident laser radiation can result in electric field enhancements through well know Mie resonances. This local field enhancement could then lead to more efficient electron generation and brighter x-ray production. The idea of using micro structured targets for x-ray produciton with an intense laser is not new. Recent experiments have demonstrated enhancements in x-ray yield achieved by using structured surfaces such as gratings [1], velvets [2], and nanoparticles [3]. The use of well defined, monodisperse microspheres offers the advantage of exploiting the Mie resonance in a controlled way.

This past year we investigated hard x-ray (>100 keV) generation from copper targets coated with a partially covering layer of microspheres. When a spherical object is illuminated with light of a wavelength,, similar to the diameter, d, of the object, a complicated electric field pattern arises due to interference between the incident and scattered waves. The interaction of an intense laser with such a target can generate a spherical plasma with non-uniform heating across its surface [4, 5]. For example, figure I.L.1 displays the electric field pattern of a 1μm spherical plasma irradiated with 0.8 μm laser ligh t. In particular, when the size parameter $m = \pi d/\lambda \approx 1$, the

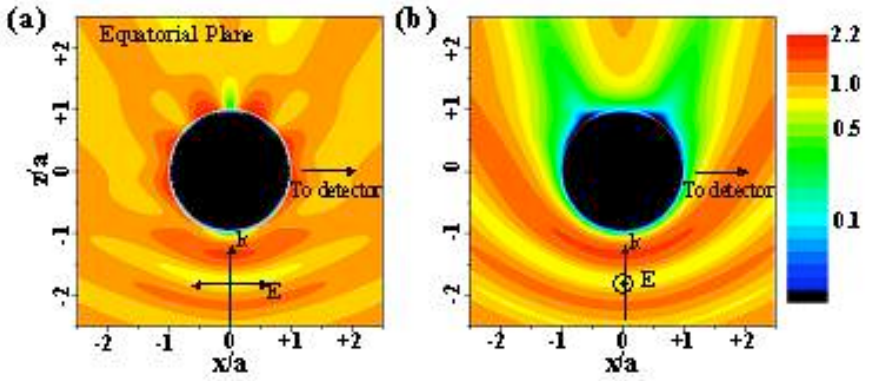

Fig. I.L.1. Calculated electric field plot for an ionized, micron-diameter plasma sphere for laser polarization (a) parallel and (b) perpendicular to the page. The laser propagation direction is +z. Note the enhancement in the field visible in (a). The strength of the electric field is color coded as a ratio of the field strength in vacuum. A field enhancement of over x2 at the sphere's surface is observed in the simulation.

system can experience a Mie resonance in which the electric fields are greatly enhanced. By depositing wavelength-length scale spheres across the surface of a metal substrate, we aim to exploit the Mie resonance to increase the temperature of the resonantly heated electrons which are responsible for the generation of hard x-rays.

We prepared the targets using commercially available polystyrene spheres of diameter 0.26, 0.5, 1.0, 1.5 and 2.9 μm with a size distribution of 3%, diluted with water to a concentration of ≈1:1000, and applied to polished copper substrates. The solution was made more dilute for the smaller spheres to improve the consistency of the surface. We observed the target surfaces using a scanning electron microscope (SEM) to ascertain the uniformity of the coating and to check the depth of the sphere layers. SEM images of copper coated with a 2.9 μm sphere solution, shown in figure I.L.2, at magnification of (a) 100x and (b) 5000x demonstrate that the spheres form a monolayer over a large area.

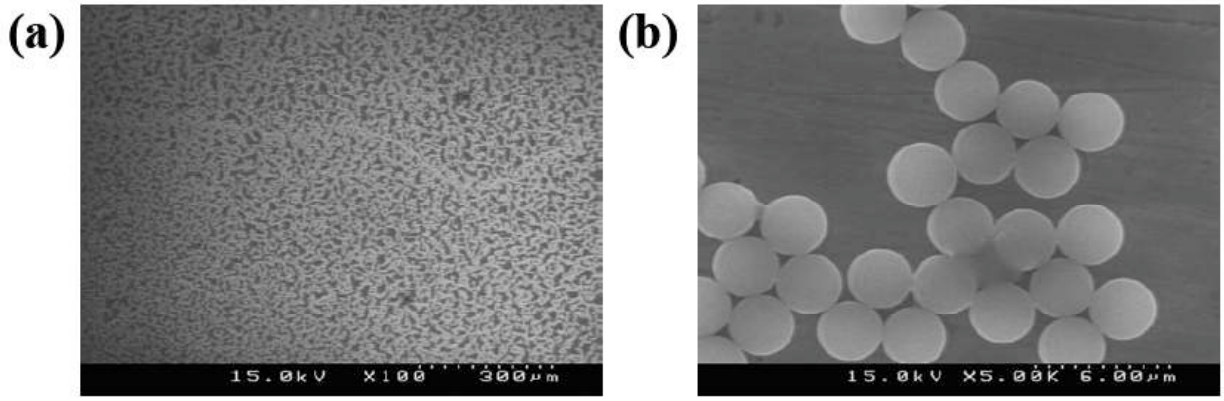

Fig. I.L.2. Scanning electron microscope images of a copper substrate coated with 2.9 μm spheres at (a) 100x and (b) 5000x magnification. Note the uniformity of coverage in (a) and the size consistency shown in (a).

We performed the experiment using the THOR laser system. Initially we employed the 800 nm pulses directly. However, a scan of x-ray yield as a function of angle for p-polarized pulses on a planar solid Cu target revealed that we had a significant preplasma with scale length of the order of 3 μm. Since we wished to interact with structures that were smaller than this, clearly this prepulse significantly altered the sphere prior to the arrival of the main pulse. To mitigate this problem we frequency doubled the laser with a KDP crystal. This yielded scale lengths which were < 100 nm. The focal intensity at 400 nm was $\approx 2 \times 10^{17}$ Wcm^{-2}. Hard X-ray emission from the plasma was observed using six filtered NaI scintillation detectors arranged around the target chamber. Ion emission from the front surface of the target was measured using a charge collector (Faraday cup) at a distance of 0.20 m behind a mesh biased at -300V to reduce the emission of secondary electrons from the detector surface. A magnetic field of 1 kG was placed ≈1 cm in front of the collector to deflect electrons.

X-ray yields and ion spectra from polished copper targets were directly compared to sphere coated copper targets at incidence angles of 0°, 10°, 24° and 45°.

We illuminated polystyrene spheres of diameters 0.1 -2.9 microns on a glass substrate, with a 400 nm 100fs pulse. We were observing X-rays in the energy range of 25-75 KeV.

X-ray yield at two photon energies as a function of sphere size is illustrated in figure I.L.3. We see a clear peak in the x-ray yield for spheres with size 260 nm diameter. This surprisingly does not correspond to the sphere size in which we expect a maximum in the electric field from Mie resonances.

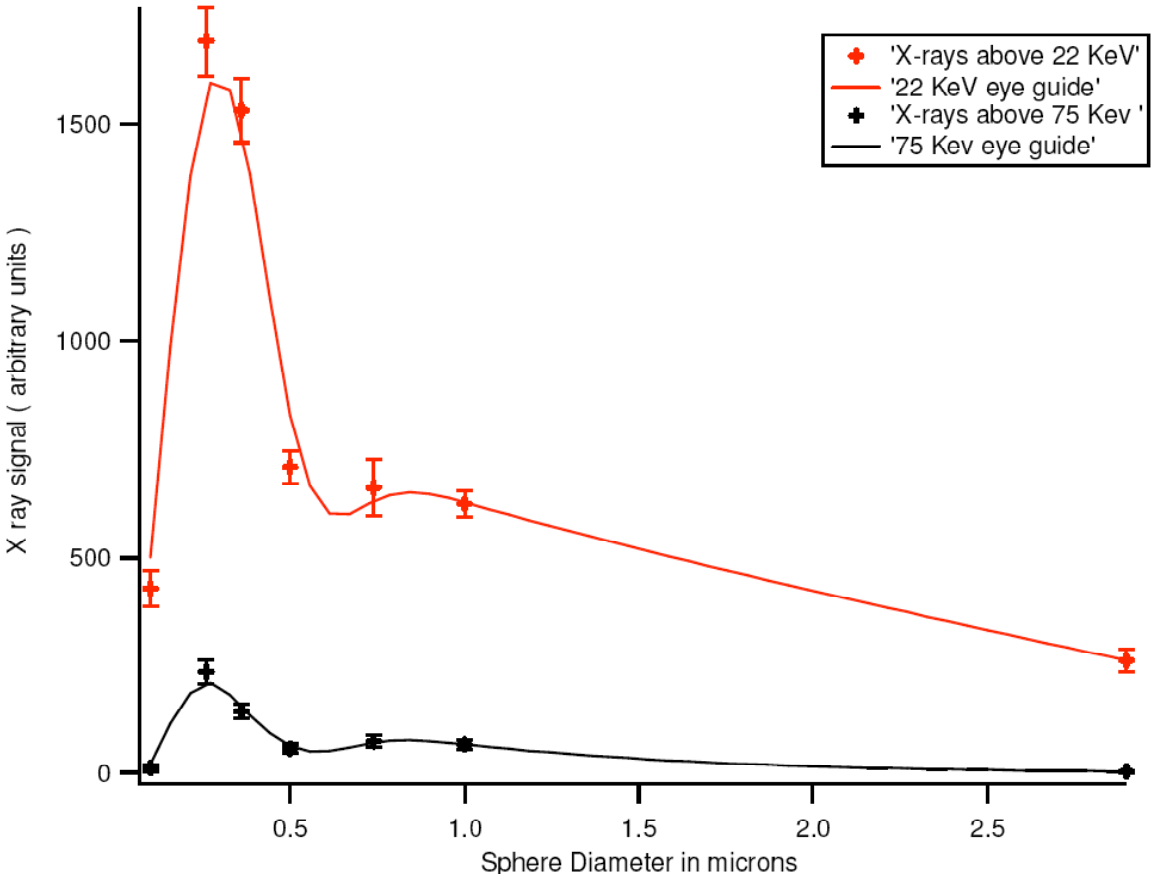

Figure I.L.3: X-ray yield as a function of sphere size measured with filtered NaI detectors.

To explore these effects we performed Mie based modeled to solve for the local field around a sphere. The two physical parameters in the model are the size parameter (a ratio of the sphere radius to wavelength) and the index of refraction of the sphere. Our spheres can be considered as above critical density plasma balls. Using hydrodynamic codes both Medusa103 and Haydes, we estimated the energy of the electrons in the plasma +-1 Kev and the collisionality. Using Drude model we can obtain an estimate for the index of refraction of the plasma. We conducted parameter scans of both the index of refraction and size parameter. The electric field distribution and size was fairly insensitive to realistic changes in the plasma density and collisonality. A sphere size scan revealed a clear maximum in the electric field strength at the surface. For our wavelength the maximum modeled electric field occurred at 0.1 microns.

To gauge the effect of the substrate effect on the electric field we used the method of images from a perfectly conducting surface. By superposing two solutions for the electric field we were able to use the same code to obtain the electric field in this situation. The size of the resulting intensities was lower then for the free sphere case but the position of the maximum intensity was unchanged from 0.1 um. This calculated field distribution for a 260 nm sphere is illustrated in figure I.L.4.

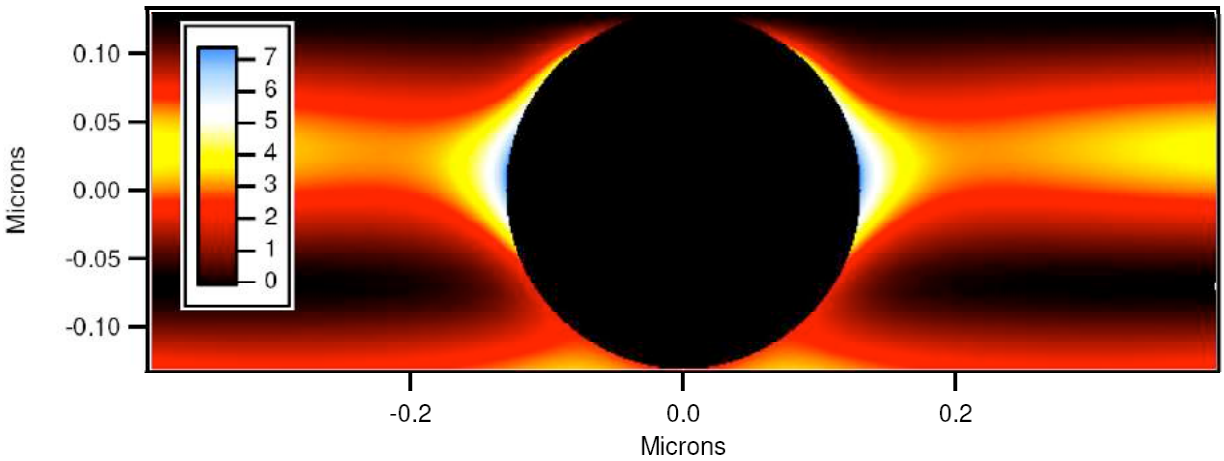

Figure I.L.4: Intensity around a 0.26 micron plasma sphere on a perfectly conducting plane (Plane is across top of image)

We next attempted to study the effect of having multiple spheres in close proximity. We contacted Mackowski who developed a code for to calculate the far field response of closely packed spheres. He extended his code to output the near field following our output specifications. This is now publicly available software available at his website [8]. We experimented with various sphere packing situations and studied hexagonal closed pack formations and random sphere formation. The maximum field enhancement occurred as expected for closely positioned spheres in the direction of polarization. To gauge this effect we ran the code with two identically sized spheres next to each other and changed the sphere size. We observed that the field was enhanced by more then an order of magnitude over the single spheres and that the size of maximum field was shifted to smaller diameter spheres. Such a calculation is illustrated in figure I.L.5.

The summary of these calculations is presented in figure I.L.6. Here, the effective intensity on the surface of the sphere (proportional to $|E|^2$) is plotted for all three situations. All three calculations suggest E-field enhancement for spheres with diameter smaller than those in which we see a maximization of x-ray energy. We are now exploring the possibility that the observed peak results from stochastic heating transit time resonances. This will be investigated with two and three dimensional PIC codes.

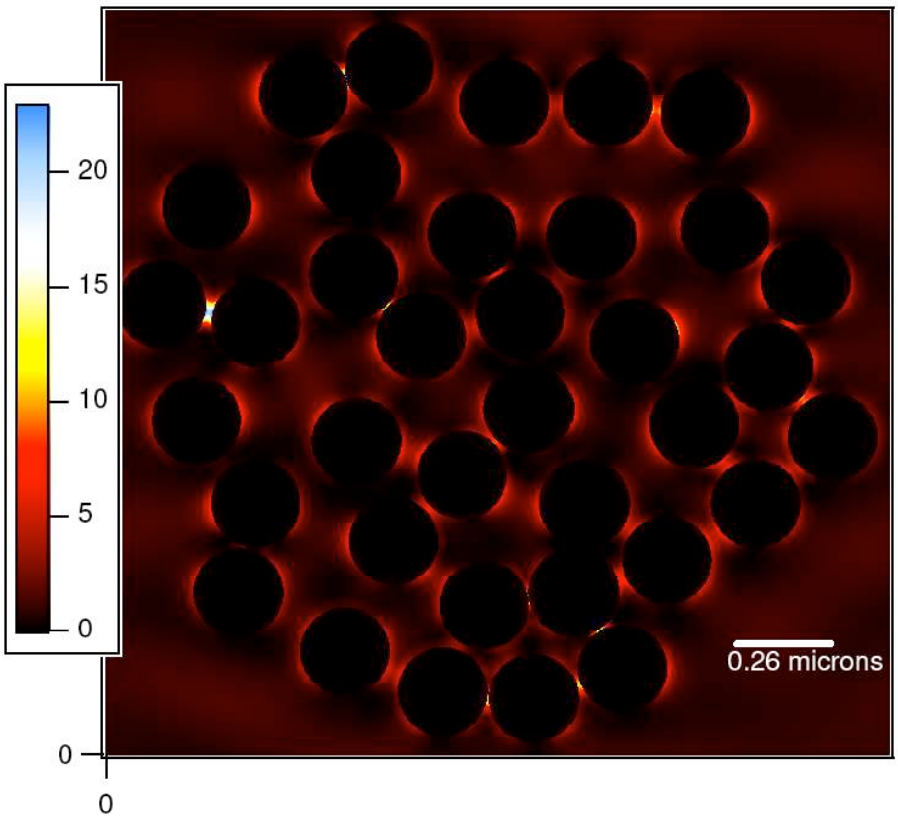

Figure I.L.5: Example of Intensity around randomly positioned 0.26 micron spheres

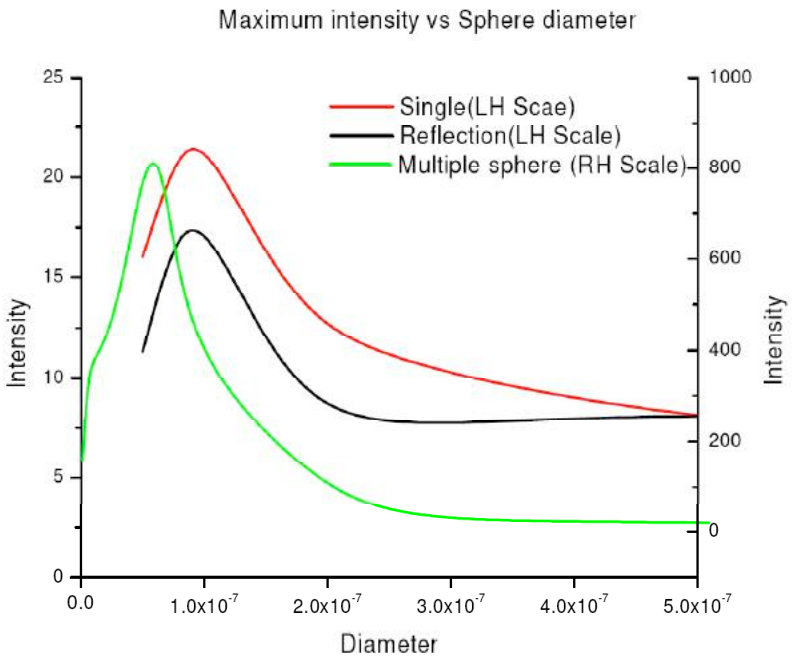

Figure I.L.6: Maximum intensity at sphere surface for isolated sphere, two spheres in close proximity and a sphere on a perfectly conducting surface

References for section I.L

1. S. P. Gordan, T. Donnelly, A. Sullivan, H. Hamster, and R. W. Falcone, Opt. Lett. **19**, 484 (1994).
2. G. Kulcsar, D. AlMawlawi, F. W. Budnik, P. R. Herman, M. Moskovits, L. Zhao, and R. S. Marjoribanks, Phys. Rev. Lett. **84**, 5149 (2000).
3. P. P. Rajeev, P. Taneja, P. Ayyub, A. S. Sandhu, and G. Ravindra Kumar, Phys. Rev. Lett. **90**, 115002 (2003).
4. T. D. Donnelly, M. Rust, I Weiner, M. Allen, R. A. Smith, C. A. Steinke, S. Wilks, J. Zweiback, T. E. Cowan, and T. Ditmire, J. Phys. B **34**, L313 (2001).
5. D. R. Symes, A. J. Comley, and R. A. Smith, Phys. Rev. Lett. **93**, 145004 (2004).
6. A. A. Andreev and J. Limpouch, J. Plasma Physics **62**, 179 (1999).
7. E. L. Clark, K. Krushelnick, M. Zepf, F. N. Beg, M. Tatarakis, A. Machacek, M. I. K. Santala. I. Watts. P. A. Norreys, and A. E. Dangor, Phys. Rev. Lett. **85**, 1654 (2000).
8. http://www.eng.auburn.edu/users/dmckwski/scatcodes/

I.M Magnetic Plasma Jets of Astrophysical Significance from a Laser Produced Plasma

Participants
*P. Brady, P. Valanju, R. Bengtson, and T. Ditmire (**University of Texas**)*

Leveraging the large expertise here at UT in magnetized plasmas, we have begun an investigation of plasma jet formation subject to external magnetic fields. These experiments are motivated by astrophysical jets of various types. Astrophysical plasma jets have interested scientists for decades due to their high velocities and collimation properties. Astrophysical plasma jets can emanate from accretion disks surrounding supermasive black holes, quasars and young stellar objects. They can obtain speeds on the order of 0.1c – 0.99c. Recent VLBA radio telescope images of astrophysical jets from the M87 galaxy have brought new interest in the study of astrophysical jets (see figure I.M.1). The radio telescope images revealed that these magnetic jets leave their origin with large solid angles and collimate several parsecs away from the source and remain collimated for thousands of parsecs. Scientists generally believe that magnetic fields are responsible for the collimation and speeds that these jets obtain. The current theories state that the magnetic fields get "wound up" from the spinning action of the accretion disk and once wound up the magnetic field expands like a compressed spring collimating the plasma and accelerating it.

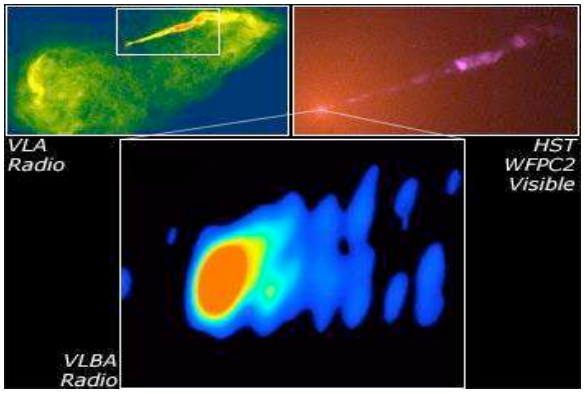

Figure I.M.1: Recent radiographs of the galactic jet from M87. [1]

We have embarked on an experiment in which the plasma is produced by a laser inside an externally imposed magnetic field. We would like to produce plasma in an environment where an electrode with a quasi spherical electrical field distribution is inside a strong axial magnetic field. We predict that this electromagnetic formation will provide conditions for the plasma to spin due to the **E x B** drift. We predict that this spinning motion will simulate the spinning of plasma in an accretion disc, and that the plasma will spin up the magnetic field in a way similar to a magnetized jet coming out of an astrophysical accretion disc. We use hydrodynamic scaling conditions to justify the comparison of physics between the laboratory frame and the astrophysical frame. The similarity numbers for a jet from a young stellar object and our laser experiment are estimated in table I.M.1.

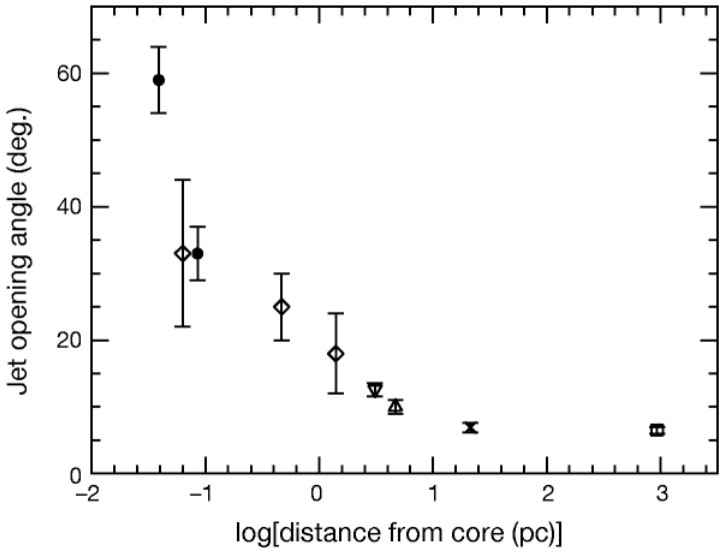

Figure I.M.2: Collimation angle vs. distance for the galactic jet emanating from M87. [2]

	Young Stellar Objects	Experiment
h(cm)	10^{11}	10^{-2}
t(s)	10^{4}	10^{-7}
P(Pa)	10^{-9}	10^{6}
n(cm^{-3})	10^{3}	10^{18}
T(eV)	1	1
B(G)	10^{-4}	10^{3}
v(cm/s)	10^{7}	10^{7}

Table I.M.1: This table compares the physical parameters between our experiment and young stellar objects. The orange regions are assumed parameters and the yellow regions are calculated to make the physics between the two regions hydrodynamically invariant. [4][5]

The specifics of our experiment, shown conceptually in figure I.M.3, involves impinging a focused 5J, 8ns FWHM 1064nm laser pulse onto a wire 25 μm in diameter inside a vacuum chamber with various electromagnetic field configurations. We back light this interaction with a

2ns FWHM 532nm Quantel laser pulse. This back lit laser pulse is imaged onto a CCD camera with the focus of the imaging telescope blocked by a beam block providing a Schlieren (dark field) image of the interaction. We place the interaction in three different environmental conditions, all of which have a background pressure of 10 mTorr. The first environment has no electromagnetic fields. The second environment has an axial magnetic field aligned with the wire, with the magnetic fields strength about 0.1 to 1.0 Tesla emanating from a permanent magnet. The third environment has the same magnetic field with an electric potential of 2500V supplied to the wire. We will use Schlieren images of the plasma expansion to look for evidence of successive axial broadening with the progression of the three environmental conditions.

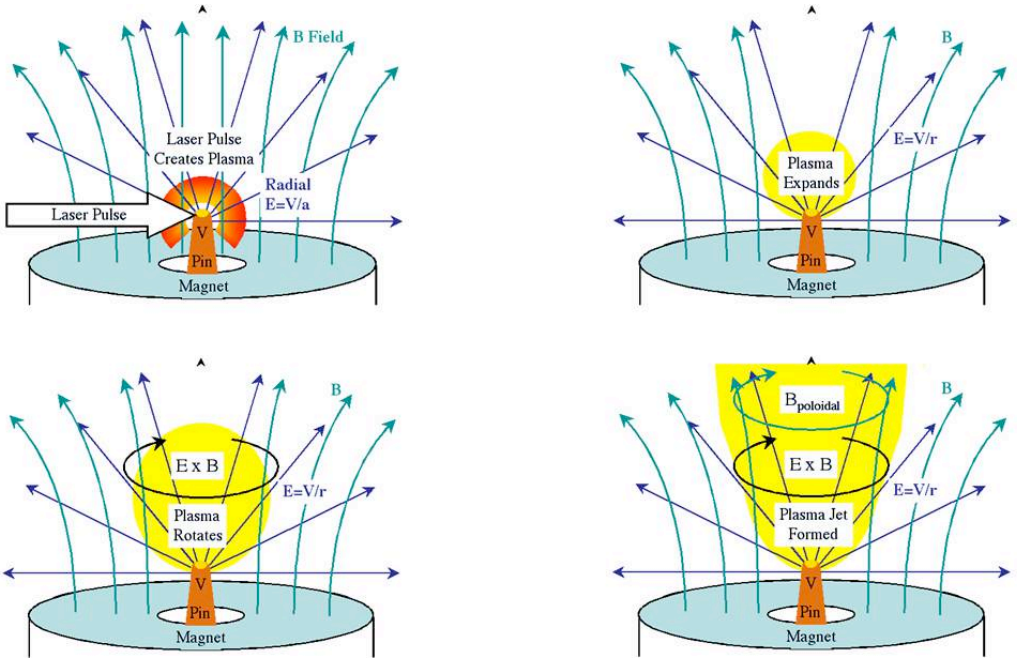

Figure I.M.3: Diagram of the predicted plasma expansion in our experiment. The laser creates an expanding plasma by impinging on the electrode. The ExB plasma drift spins the plasma, and the spinning plasma produces poloidal magnetic fields that aid in the jet formation. [3]

To create the laser plasma we have developed a compact multi-joule laser. This laser is an Nd-doped silicate glass amplified laser whose layout is illustrated in figure I.M.4. Using a seed laser of a GCR-YAG laser and telescope relay system we amplify the pulse with Pulse Forming Networks (PFN), powering the 19mm laser heads containing our silicate glass rods. We are capable of producing a pulse containing up to 5 joules. We built a vacuum chamber and a laser probe imaging system to house and image the laser plasma interaction. Using a HeNe laser collinear to the path of the drive beam we are able to position the target in the z-axis, and using the CCD camera we image the probe beam with we are able to position the target in the x-y plane. This positioning system has given us a high degree of repeatability on a shot per shot basis. We measure the timing and energy of the interaction using a photodiode.

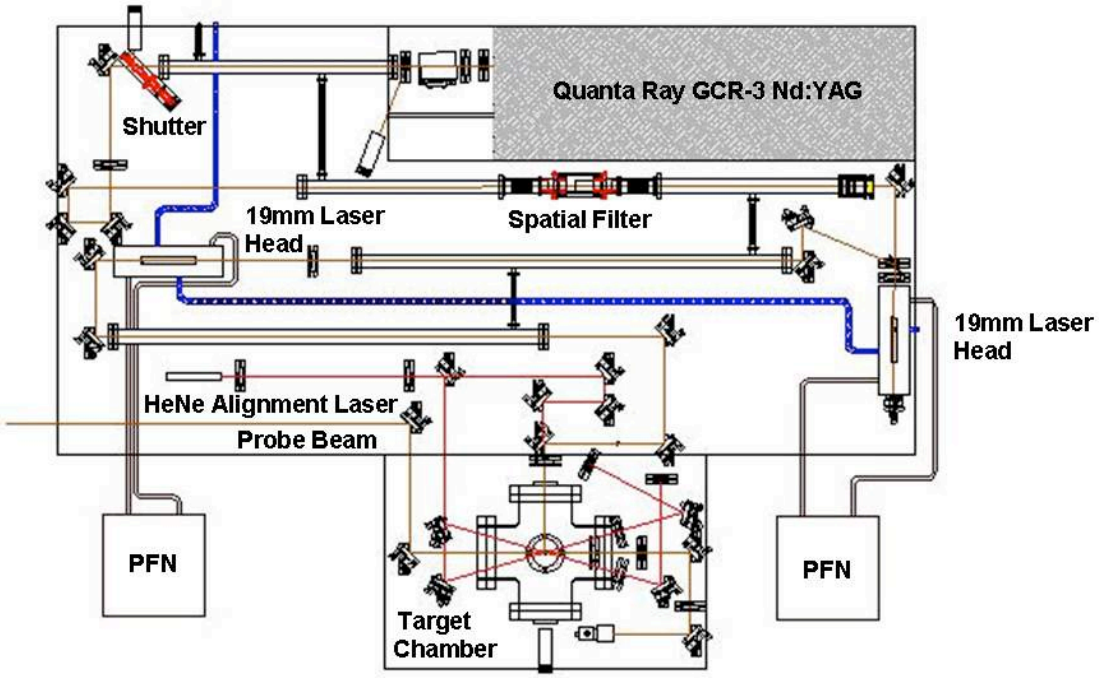

Figure I.M.4: Diagram of the laser system and experimental set up.

We have performed experiments in the first two conditions described. We have taken a series of Schlieren images in the conditions without magnetic fields and with magnetic fields. The magnetic fields at the laser plasma interaction region were 900 Gauss in magnitude. The timing and energy measurements of each shot were taken with a DET 210 photodiode. The results are displayed in figure I.M.5 in false color. The intensity in the picture is related to the gradient of the electron density. The data shows only slight differences in the two field conditions, which will not be significant for our purposes. We are modeling a design for a permanent magnet system that could give us 1 Tesla fields over a larger experimental region. We are currently adapting the electrode system to give us the electrical fields necessary to complete our experiment.

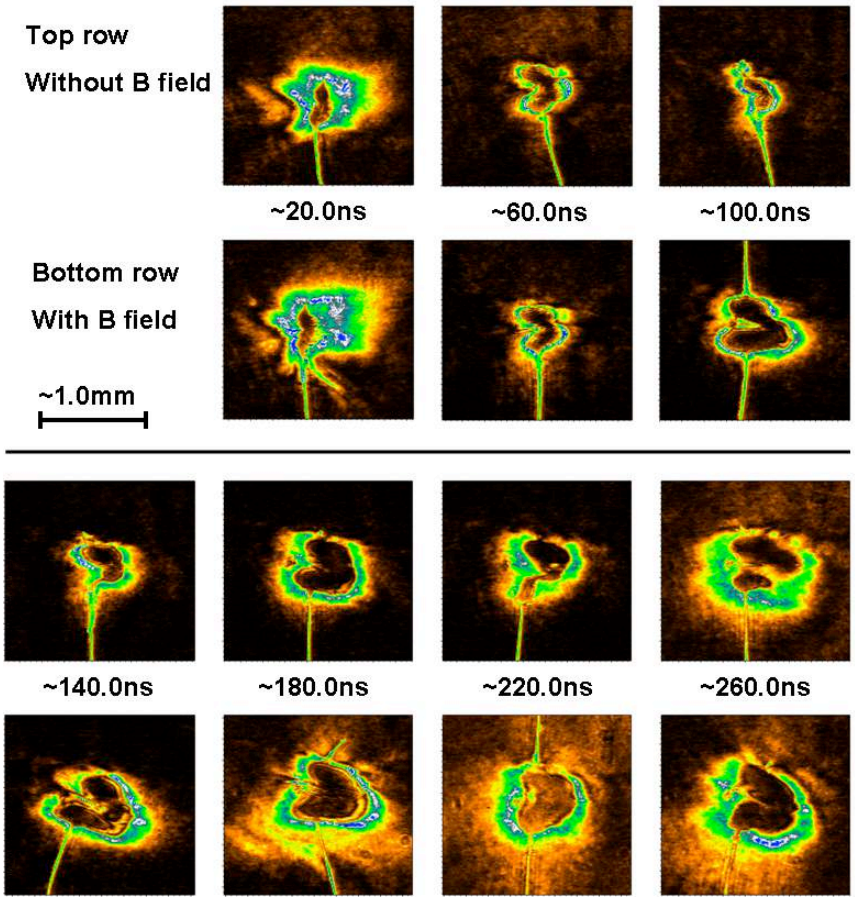

Figure I.M.5: Schlieren images of the time evolution of laser produced plasma with and without magnetic fields. The laser energy was ~4.7J, and the magnetic field strength was 900 Gauss.

References for section I.M:

1. http://oposite.stsci.edu/pubinfo/PR/1999/43/index.html
2. Magnetohydrodynamic Production of Relativistic Jets, David L. Meier et al., Science Volume 291, Number 5501, Issue of 5 Jan 2001, pp. 84-92.
3. Pictures by Prashant Valanju
4. Bacciotti, F., Eislöffel, J. 1998, Astron. Astrophys. "Ionization and density along the beams of Herbig-Haro jets"
5. Toshiki Tajima, Plasma Astrophysics, Addison-Wesley 1997

I.N Laser heating of clusters and cluster Coulomb explosions

Participants:
*M. Hohenberger, D. R. Symes, K. W. Madison A. Sumeruk, M. Teichmann, K. Hoffman J. Keto and T. Ditmire (**University of Texas**)*

We have an ongoing campaign within TCHILS to study high intensity laser interactions with exploding clusters. During the past year, with support from the Center, we have performed three activities in this area: we have studied the explosion of hydrogen clusters, the explosions of argon clusters subject to multiple independently delayed pump pulses and the explosions of heteronuclear clusters.

Our first set of experiments during the past year represented a finalization of experiments begun somewhat earlier. In particular, we examined the explosions of clusters in the regime intermediate to the standard, pure Coulomb explosion where all electrons are ejected by the laser field, and a hydrodynamic explosion, where most electrons are retained in the cluster by space-charge forces. To derive information on this intermediate regime, we examined the anisotopy of ions ejected from laser irradiated hydrogen clusters. Some recent work by Kumarappan *et al.* showed anisotropy in the explosion of argon clusters [1]. This anisotropy was attributed to the creation of higher ionization states at the poles of the spherical cluster resulting in the ejection of higher energy ions in the direction of the laser polarization. We chose, instead, to study the ion spatial distributions in hydrogen, where any anisotropy must arise from the electron dynamics and not by differing charge states.

In our experiments we did indeed observe a clear asymmetry with ion energies ejected from H_2 clusters. In particular we measured an enhancement of ion energies along the laser polarization direction. We conducted measurements for both short (40fs) and long (250fs) pulses attempting to access the pure Coulomb and intermediate interaction regimes. We find that the measured ion energies from irradiation with the short pulse can be reasonably well explained using a complete vertical ionization model. However, we find that higher ion energies were attained with the longer pulse, which we interpret as evidence for the vacuum heating of cluster electrons.

In our experiment we produced clusters with a pulsed supersonic gas jet directed through a skimmer which produced a low density cluster beam. The experimental apparatus is illustrated in figure I.N.1. These clusters were irradiated by the THOR laser in our lab at the University of Texas, which delivers 35fs, 800nm pulses with energy up to 0.75J at 10Hz. The laser was focused using an *f*/4.9 refractive graded index aspheric lens into the cluster beam. The energy was varied between 21mJ and 70mJ providing intensities between $\approx 9.6 \times 10^{16}$W/cm^2 and $\approx 3.2 \times 10^{17}$W/cm^2. The energies of the ions created by the laser cluster interaction were determined by measuring their time-of-flight (TOF) in a 1.14m, field-free drift tube. A microchannel plate (MCP) detected ions in an angular cone of 7.8×10^{-4}sr from the focus. We estimated the cluster size to be approximately 5 nm with both H_2 clusters.

The measured ion-energy spectra are shown in figure I.N.2 for two orthogonal polarizations, 0° (black) and 90° (gray), where 0° is defined as when the laser electric field points toward the detector. Both mean and maximum ion energies are enhanced for the 0° polarization.

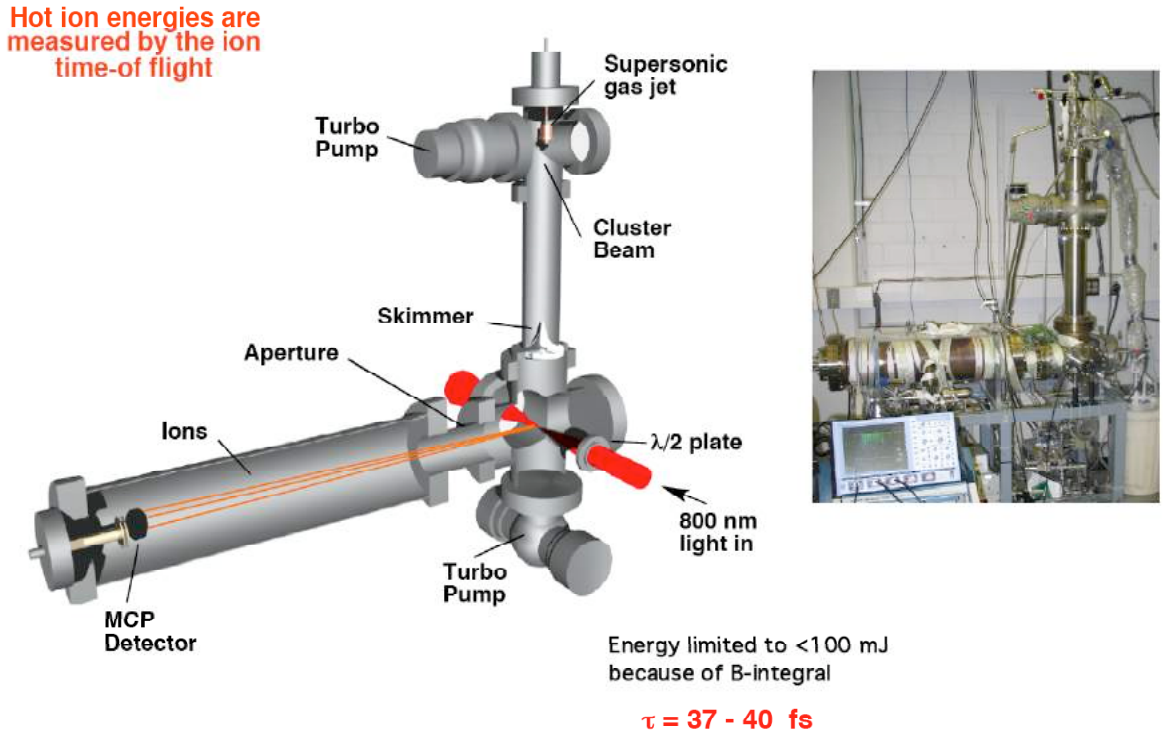

Figure I.N.1 Experimental apparatus for exploding cluster experiments.

With a 40fs pulse we observe E_{av}≈1keV and E_{max}≈9.5keV at 0° and E_{av}≈0.6keV and E_{max}≈8keV at 90°. With 250 fs pulses we observed E_{av}≈2keV and E_{max}≈13keV at 0° and E_{av}≈1.6keV and E_{max}≈11.5keV at 90°. Immediately striking and initially unexpected is the large increase in energy resulting from the use of the longer 250 fs pulse. The mean energies as a function of polarization angle for both pulse durations are shown in figure I.N..3. In both cases the energies optimize at 0° with the degree of anisotropy, $\left[\varepsilon_{\max}(0°)-\varepsilon_{\max}(90°)\right]/\varepsilon_{\max}(0°)$ ≈40% with 40 fs and ≈ 25% with 250 fs pulses. The plane of detection is perpendicular to the propagation direction of the laser so the aspect ratio of the laser focus has no bearing on the anisotropy measurement.

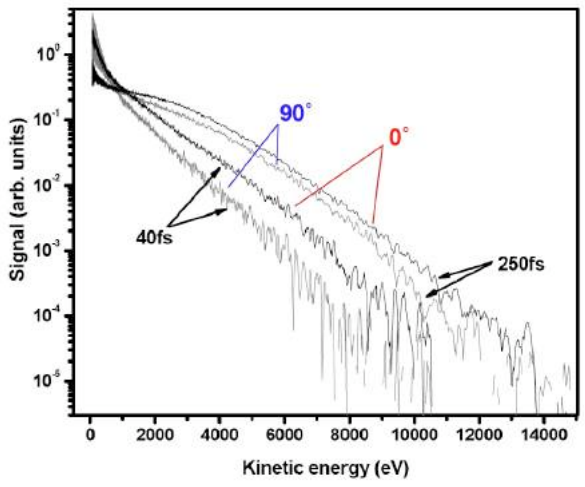

Figure I.N.2 Proton kinetic energy spectra from H_2 clusters irradiated with 40fs and 250fs laser pulses with 0° (black) and 90° (gray) polarization.

Though we expect that the hydrogen clusters will explode primarily by Coulomb forces, the deviation from a purely spherical explosion indicates that this picture is not entirely correct. Even when we employ 40 fs pulses the explosions do not strictly adhere to the fully stripped vertical ionization model

(ie the model in which all elelctrons are stripped from the cluster while it is at still at its initial radius). This model predicts symmetric ion expansion. Furthermore, the strong increase in ion energy observed when using a longer pulse was not predicted in simulations of small, 34Å D_2 clusters irradiated with pulse widths from 5–100fs. These simulations showed a steady decrease in ion energy since expansion reduces the charge density driving the explosion. We surmise that the energy enhancement originates from larger clusters in the distribution. These cannot be described with a purely Coulombic model since the extracted electrons begin to influence the expansion.

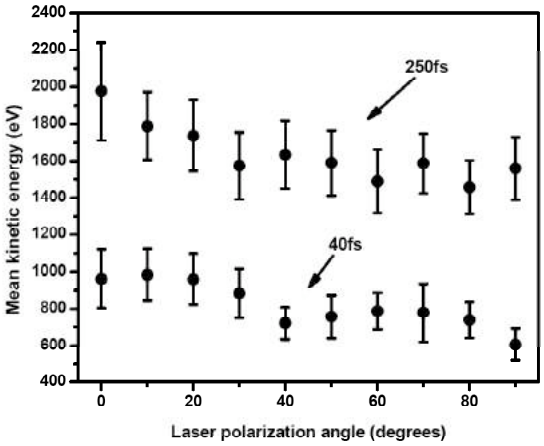

Figure I.N.3: Angular distribution of the mean ion energies from H_2 clusters irradiated with 40fs and 250fs laser pulses

Our colleagues here at UT, Boris Breizman and Alex Arefiev, have examined the physics of clusters partially evacuated of electrons in some detail. They find that ion anisotropy is inherent in the explosions of partially evacuated clusters. The internal electron core oscillates along the laser field direction so the force acting on the ions during the laser pulse is not symmetric. Further ion anisotropy arises when a cloud of extracted electrons remains bound to the cluster since the electron pressure is higher along the laser field axis. Particle-in-cell simulations support this picture for clusters with cluster radius comparable to the electron excursion distance in the laser field, a situation we find in our experiments. Furthermore, molecular dynamic simulations of D_2 cluster explosions also show an anisotropy which reduces with an increasing fraction of electron extraction. Our observations are consistent with this picture.

For the longer pulse -- 250 fs -- interactions, the expansion of the ions cannot be ignored because it takes place on the same timescale as the electron extraction. This would be expected to decrease ion energies because the reduction in density lowers the potential of the cluster. However, the pronounced shift of the spectrum to higher energies shows that this is overcome by the superior vacuum heating driven by the longer pulse. The longer pulse has more time to heat stochastically the electrons in the cluster and the more energetic electrons aid in driving a more energetic explosion.

We have also continued experiments on higher Z clusters, particularly with the goal of confirming the effects of the giant dipole resonance in enhancing the laser absorption and driving a more energetic explosion. These experiments were a natural continuation of the absorption, pump-probe experiments we conducted at LLNL. We examined the ion energies of argon ions from clusters irradiated by two 800 nm pulses, with the intention of delaying the second “pump” pulse by an amount that would allow the 800 nm light to come into resonance with the cluster giant dipole resonance.

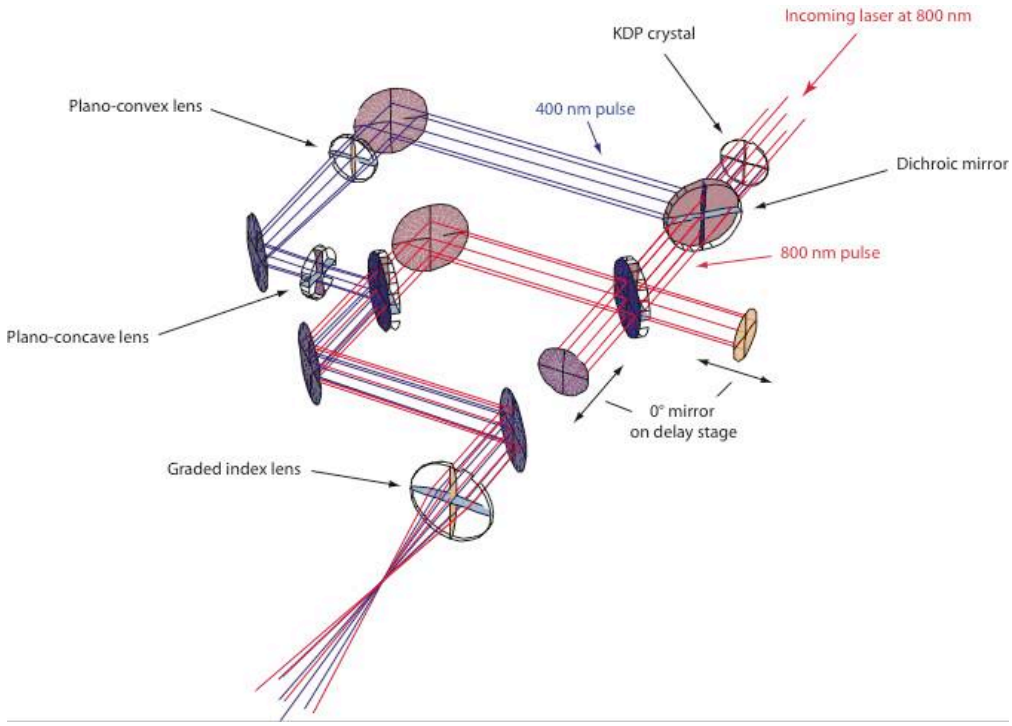

Figure I.N.4. Optical set-up for the multi-pulse pump- pump experiment.

For these experiments, we utilized the THOR laser and the apparatus pictured in figure I.N.1. We then installed a multi-pulse "pump-pump" optical set-up on the front end of the TOF chamber. This multipulse system is illustrated in figure I.N.4. We have designed the optics to allow us to irradiate the clusters with three delayed pulses, the first at 800 nm to initiate the explosion of the cluster, a second at 400 nm to hit the resonance at a plasma density of 2 x 10^{22} cm^{-3} and a third at 800 nm to hit the resonance at 5 x 10^{21} cm^{-3}. In the experiment we report here, only the two 800 nm pulses were used. We are presently analyzing the data from the three-pulse experiments.

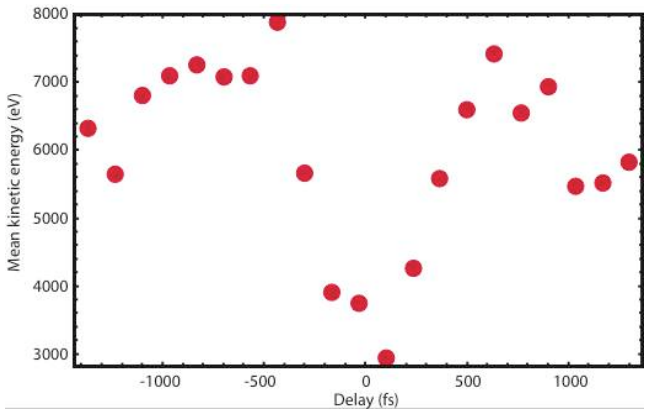

Figure I.N..5. Measured mean ion energies from exploding Ar clusters irradiated by two, delayed 800 nm pulses of equal energy.

Argon TOF ion traces were recorded with >1000 integrated shots per time point, and the mean ion energy determined from these traces. The argon cluster sizes were on average 10 nm as determined from Rayleigh scattering measurements. The mean ion energy as a function of delay between two equal strength pulses, each with roughly 30 mJ is plotted in figure I.N.5. When the pulses overlap, when the intensity in the clusters is highest, the mean energy we observe is only 3 keV. However as the delay between the two pulses increases (in either direction) to around 700 fs, the mean ion energy grows to 7 keV. It then falls off with greater delay.

These data seem to confirm the importance of the giant dipole resonance in the absorption of the second pulse and in driving the cluster explosion.

The third aspect of our cluster investigations over the past two years has been in the studies of mixed species clusters, particularly of low Z clusters at high intensity which rest in the pure Coulomb explosion regime. This is the regime most appropriate to the cluster fusion experiments described below. The motivation for studying Coulomb explosions of mixed species clusters in the context of exploding cluster fusion was advanced recently by Last and Jortner [2,3]. They showed, through a series of molecular dynamic simulations that the energies of deuterons from exploding heteronuclear clusters, like D_2O could exhibit enhancements in ion energy through a dynamical effect in the Coulomb explosion.

During the Coulomb explosion of a single species cluster, like D_2, clusters will eject deuterons with an energy given directly by the potential energy of the ion, as it is initially in the fully stripped cluster. In this simple picture, if higher Z ions are present, and ionized to higher charge states by the laser, the presence of the more highly charged ions should increase the stored potential energy of the deuterons and increase the subsequent energy of the ejected deuterons. Last et al. showed that, provided that the kinematic parameter $h = q_D m_D / q_B m_B$ is greater than 1 (where q_B and m_B are the charge and mass of the heavier, high Z ion and m_D, q_D are the mass and charge of the light ion), then the light ions will outrun the heavier ions and explode in an outer shell with a higher average energy than would be expected from the naïve estimate of ion energy based on initial potential energy. They further showed that fusion yield could be substantially increased in plasmas formed from explosions of heteronclear clusters over that of neat D_2 clusters of the same size because of this kinematic enhancement of ion energies in the mixed ion case.

To explore this physics, we performed experiments on laser induced explosions of the methane isotopes CH_4 and CD_4. These clusters are produced under otherwise identical conditions and have the identical chemical and clustering properties. Since they differ only in the η_A parameter, these data provide unambiguous evidence of a dynamic acceleration effect during the ion expansion, since the initial potential driving the cluster explosion is the same in both cases. The experimental apparatus used was the same as that in figure I.N.1. The laser and gas jet parameters were also similar to the experiment described in the previous section, with the exception that the gas jet was backed with one of the methane gases. We estimated that the methane cluster sizes in these experiments had an average diameter of 3 nm.

Measured ion distribution from both methane and deuterated methane clusters are shown in figure I.N.6. The original TOF data for each were averaged over 200 shots, normalized and

converted to an energy spectrum. The shape of the spectrum is consistent with that expected from Coulomb explosion when a distribution of cluster sizes is taken into account. The transformation to an energy distribution required us to assume a certain mass, which we set to the mass of H^+ or D^+, according to the gas we were shooting. The signal is a superposition from both carbon and deuterium/hydrogen arriving at the MCP and these signals cannot be separated. We assume that the maximum energy E_C, for carbon ions of mass m_C, is approximately 2.5-3 times the maximum energy of the lighter species. We can then estimate a minimum TOF for the heavier carbon ions which corresponds to a maximum energy in the energy spectrum obtained using the mass of the lighter ion species m_A. Any signal above this energy $E_{min} = E_C \cdot m_A/m_C$, denoted in figure 3.6 by the dotted lines, can only be caused by the detection of H^+ or D^+ ions.

The difference in kinematic parameters between H^+ ($h = 3$) and D^+ ($h = 1.5$) causes a clearly apparent isotope effect. In the energy ranges attributed solely to the lighter ion species, the H^+ energies exceed the D^+ energies, indicating a higher average energy in the proton distribution and validating the theory predicting kinetic energy enhancement. Figure I.N.7 illustrates similar data for a range of laser intensities. At the lowest intensities, we see very little difference between the proton and deuteron data. This would be consistent with the fact that the laser ponderomotive energy is below that required to extract all the electrons and drive a Coulomb explosion. In this case we expect a plasma-like explosion and, as the data illustrate, expect no difference between the two isotopes. At the highest intensities, however, the Coulomb explosion mechanism dominates and the dynamic enhancement seen in figure I.N.6 becomes more prominent.

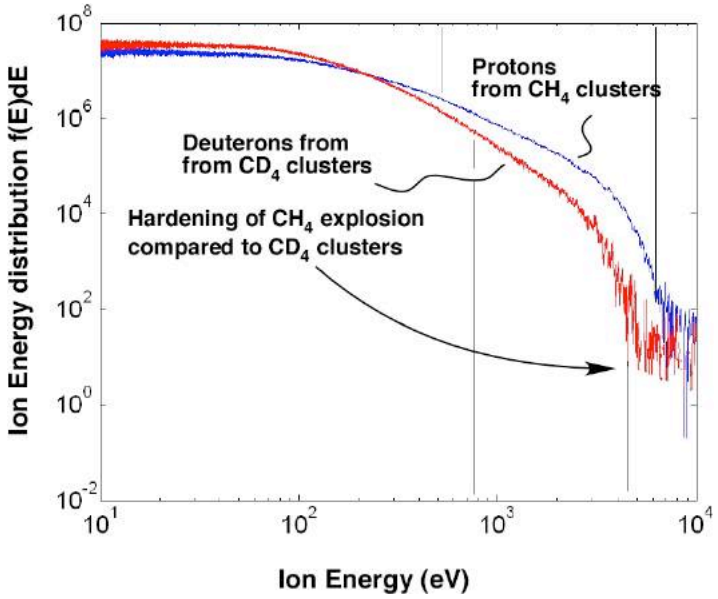

Figure I.N.6 Measured ion distribution from both methane and deuterated methane clusters.

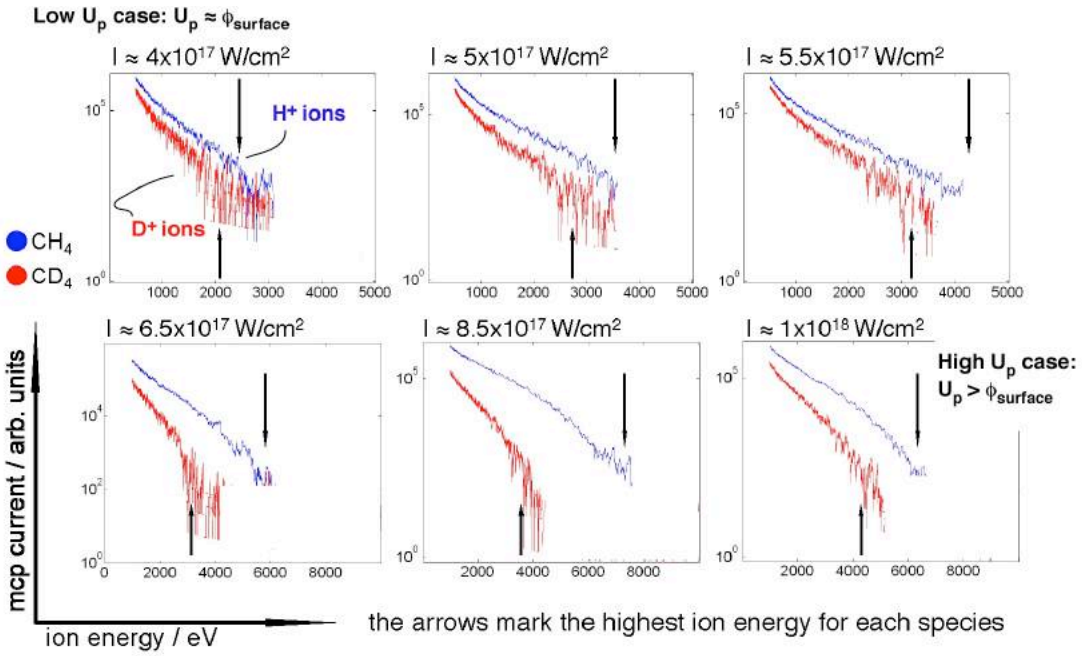

Figure I.N.7: Measured ion spectra from CH_4 and CD_4 clusters at a range of laser intensities.

References for section I.N

1. V. Kumarappan, M. Krishnamurthy, and D. Mathur,Phys. Rev. Lett. **87**, 085005 (2001).
2. I. Last and J. Jortner, Phys. Rev. Lett. **87**, 033401 (2001).
3. I. Last and J. Jortner, J. Phys. Chem. A. **106**, 10877-10885 (2002).

I.O Theoretical Studies of Intense Laser/Cluster Interactions

Participants:
*A. Arefiev, T. Ditmire and B. Breizman (**University of Texas**)*

TCHILS supports a theory effort to aid in our understanding of the cluster explosion experiments described in the previous section. A theory has been developed to describe ion acceleration in dense laser-irradiated clusters that are smaller than the laser wave-length [1].

The theory developed by Breizman and Arefiev reveals that the breakdown of quasineutrality is a key element of the laser-cluster interaction. There are three regimes of the cluster explosion that depend on the cluster radius and the strength of the laser field (see figure I.O.1). Small clusters are completely stripped of electrons and the ions explode due to their own space-charge. In medium-size clusters the laser creates a positively charged ion shell that surrounds a cold electron core. The shell expands due to its own space-charge much faster than the central part of the cluster. In large clusters the laser creates a two-component electron distribution: a cold core that responds to the laser field coherently and a hot-electron halo that undergoes stochastic heating. The hot electrons expand together with an equal number of ions that are accelerated to

supersonic velocities in a double layer at the cluster edge. The ion energy gain during the explosion increases with cluster radius, and large clusters produce fast ions with energies much greater than the ponderomotive potential. Cluster expansion limits the rate of the stochastic heating, which gives an upper estimate for the ion energy gain. The spectrum of ions produced by large clusters is found from a kinetic model of the hot-electron halo that takes into account electron cooling due to the cluster expansion. The halo model and ion spectrum results are new results to be submitted for publication. Experimentally observed anisotropy of the ion spectrum is directly related to the dynamics of the hot-electron halo. The theory of ion acceleration suggests that larger deuterium clusters can significantly enhance the neutron yield from D-D fusion events in future laser-cluster experiments.

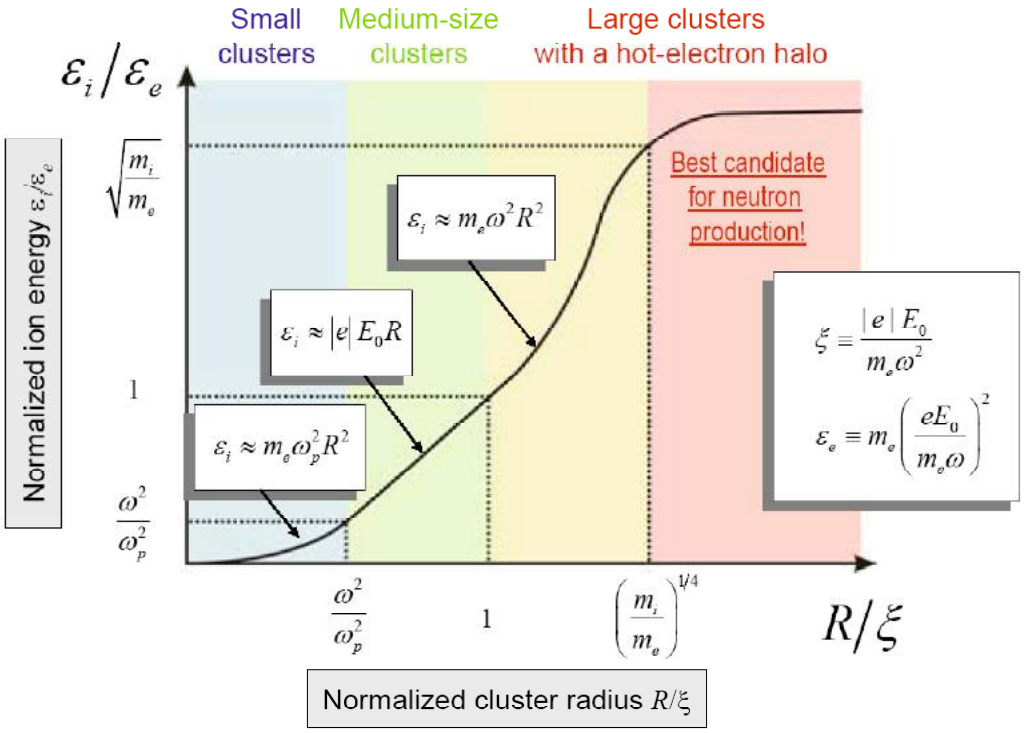

Figure I.O.1 Schematic plot of the ion energy as a function of cluster radius R for a given laser field amplitude E_0. The cluster radius is normalized to the quivering amplitude x of a free electron in the laser field E_0 and the ion energy e_i is normalized to the ponderomotive potential e_e.

References for section I.O

1. B. N. Breizman and A. V. Arefiev, Phys. Plasmas **12**, 056706 (2005).

I.P Ultrafast radial transport in a micron-scale aluminum plasma excited at relativistic intensity

Participants:
*B.T. Bowes, M. C. Downer (**University of Texas**)*
*H. Langhof (**Physikalisches Institut der Universität Würzburg**)*
*M. Wilcox, B. Hou, J. Nees and G. Mourou (**University of Michigan**)*

Under support from the Center, we have conducted a series of heat transport experiments in HED plasmas using a short pulse laser to heat a solid target. These experiments are, principally, a collaboration between Texas and Michigan. They were begun in 2004 and completed with final analysis this past year.

Intense, high contrast femtosecond laser pulses deposit energy into the electrons of a solid faster than it escapes from the initially-excited volume and much faster than the target surface expands hydrodynamically. When initial electron temperature kT_e exceeds several hundred eV radiative heat transport begins to dominate over collisional transport [1]. Past experiments in this regime [2] used loosely focused, ~1J, ~1ps pump pulses and probed the target transversely in transmission and thus were restricted to observing late stages of 1D radiative transport in an optically transparent material on a time scale of tens of picoseconds. Within our work over the last couple of years, we performed measurements using 1mJ, 24fs pump pulses from the kHz Ti:sapphire laser at the University of Michigan focused to a diffraction-limited λ^2-size spot (1.5μm diam.) to excite a metal target surface at relativistic intensity. We probe the target in reflection through microscope optics. This geometry enables us to observe the earliest stages of radiative transport in 2D on *any* target material on a sub-picosecond time scale. New features of radiative transport are expected on this space-time scale. For example, simple transport models in the diffusive limit (*i.e.* Rosseland radiation mean free path λ_R << heated spot size λ) predict very different temporal evolution of the thermal/ionization front in 2D vs. 1D [3]. Moreover, since our focal spot size is on the order of λ_R, our experiment may open up fs studies of *nonlocal* radiative transport.

Pump pulses, focused with an f/1 off-axis paraboloid coupled to adaptive optics [2], excite an Al target at 1kHz repetition rate. At the highest focused pump intensity, Kα and continuum bremsstrahlung x-rays are clearly observed. The target is translated so each laser shot interacts with clean target material. Surface wobble is limited to <1μm giving highly reproducible damage spots. The probe is split from the pump, frequency-doubled and focused at 60^o incidence angle to a ~20μm spot centered on the pump spot. The reflected probe is imaged with high quality microscope optics onto a CCD camera, recording 140× magnified images of the pump-excited spot with <1μm spatial resolution.

The darkening in the center of the target area (illustrated in figure I.P.1 a) indicates heating and ionization of the Al surface, but its physical origin must be understood to model transport quantitatively. In figure I.P.1 b we plot $\Delta R_{probe}(\Delta t)/R_0$ in P- and S- polarized probe reflectivity for excitation at 1.8×10^{18}W/cm^2 obtained by the measuring the center of the imaged pump-excited region. ΔR is negligible for an S-polarized probe showing that the drop of the P-polarized reflectivity is caused by resonance absorption (RA) [4] at the expanding critical surface. The

critical surface expands vertically at the ion acoustic velocity and max. RA occurs when it expands to $v_z\Delta t_{max} \approx \lambda_{probe}/8 \approx 50$nm. [4]. From Fig.I.P.1b, $\Delta t_{max} \approx 0.3$ps, implying $v_z \approx 2\times10^7$cm/s. This v_z is consistent with ionization state $Z \approx 10$ and $kT_e \approx$ several keV. The slight delay between ionizing and heating a point on the surface to (Z,kT_e) and the appearance of maximum RA must be taken into account in modeling the radial expansion data. Since vertical expansion $v_z\Delta t$ remains much less than the radial spot size during the time interval ($0<\Delta t<1$ps) of interest, a 1D hydrodynamic MEDUSA-like model [5] is sufficient. Although pre-pulses at the 10^{-5} level were present no ΔR_{probe} occurred before arrival of the main pump pulse.

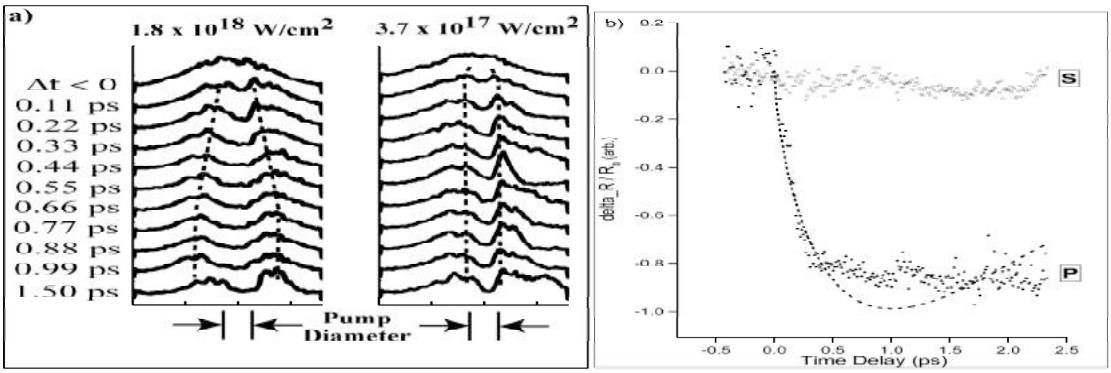

Figure I.P.1. a) Lineouts from probe images at two different pump laser intensities. Large radial expansion of the laser excited region is clearly observed at the highest pump intensity (left) but is nearly absent when the pump laser intensity is reduced to 3.7×10^{17}W/cm^2. b) Normalized S- and P-polarized probe beam reflectivity $\Delta R_{probe}(\Delta t)/R_0$ of the center of the laser excited region for pump intensity 1.8×10^{18}W/cm^2. Dashed curve: fit of P-polarized data to a 1D RA model [4] assuming constant vertical expansion velocity $v_z=2\times10^7$cm/s. The data deviate from the model for $\Delta t>1$ps because the critical surface expansion becomes 3D and kTe has cooled.

We model the evolution of the electron temperature profile $T_e(r, z\le0, t)$ at constant solid density ρ by numerically solving the nonlinear diffusion equation $\partial T_e/\partial t = \nabla\bullet(\chi\nabla T_e)$ with a T_e-dependent thermal diffusivity $\chi = (\kappa_{SH} + \kappa_R)/\rho c_v$ that included collisional (Spitzer-Härm) conductivity $\kappa_{SH} \sim (kT_e)^{5/2}/(Z+1)$ and radiative conductivity $\kappa_R = 16\sigma_{SB}T_e^3\lambda_R/3$ [3], where λ_R[cm] = $(9 \times 10^6)T_e[^oK]^2/Zn_e[cm^{-3}]$ is a simplified radiative mean free path for hydrogenic ions [1,3]. The initial condition was defined by partitioning absorbed pump energy (~1mJ, Gaussian radial profile) between electron thermal energy kT_e and ionization $Z(kT_e)$ assuming Saha equilibrium. The choice of initial absorption depth z_{abs} was not critical because $T_e(r,z\le0,t)$ quickly evolved to a nearly hemispherical profile which became the effective initial condition. Our code reproduces the 1D transport results of ref. [1]. We complete the model by coupling the calculated $T_e(r,z<0,t)$ to the 1D hydrodynamic model assuming $T_e(r,z>0,t)=T_e(r,0,t)$. This approximation is justified by the low heat capacity and high thermal conductivity of the expanding coronal plasma.

Figure I.P.2 shows the calculated profile of the critical surface S(r,z) at several Δt for excitation at 1.8×10^{18}W/cm^2. During $0<\Delta t<1$ps, S expands vertically at nearly constant $v_z\sim2\times10^7$cm/s. Simultaneously it expands radially, at first rapidly, then rapidly decelerating because of the highly nonlinear χ. The radius r_c of the "dark" spot was taken to be the radius of S(r,z) at $z=\lambda_{probe}/8$ (max. RA). The resulting time evolution $r_c(\Delta t)$ is plotted in Fig. 2b and compared with the measured HWHM $r_{dark}(\Delta t)$ of the dark spot.

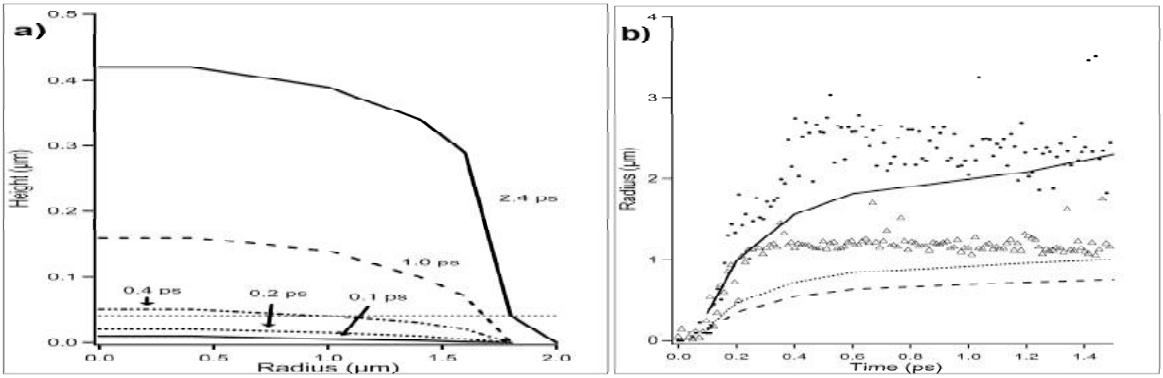

Figure I.P.2. a) Calculations of expanding critical surface of the laser-excited target from combining 2D radiative transport model with 1D hydrodynamic model at different times Δt. b) Data points: Measured radius $r_{dark}(\Delta t)$ of darkened pump-excited plasma region at pump intensities 1.8×10^{18}W/cm^2 (circles) and 3.7×10^{17}W/cm^2 (triangles). Curves: Calculated radius $r_c(\Delta t)$ of critical surface highest intensity (solid), lower intensity (dotted) and neglecting radiative transport (dashed).

Both curves reproduce the measured spatial extent of radial expansion quite well. The main discrepancy between measured $r_{dark}(\Delta t)$ and calculated $r_c(\Delta t)$ (inc. κ_R) is the faster initial evolution of the former. We believe that this is caused in part by the initially nonlocal character of the radiative transport, which cannot be described by a diffusion equation. This belief is based on an estimated $\lambda_R \sim 1\mu$m, comparable to the pump focal spot size, for our estimated initial conditions. Additional complications may be the dependence of λ_R on material opacity, which has been greatly simplified in our model, and the transport of hot electrons by **E×B** drift. [6] The latter effect pulls electrons out of the corona into vacuum, moves them radially away from the plasma region then drives them back into cool target material.

References for section I.P

1. T. Ditmire *et al.*, "Supersonic ionization wave driven by radiation transport in a short-pulse laser-produced plasma," Phys. Rev. Lett. **77**, 498 (1996).
2. O. Albert *et al.*, "Generation of relativistic intensity pulses at a kilohertz repetition rate," Opt. Lett. **25**, 1125 (2000).
3. Y.B. Zel'dovich and Y.P. Raizer, *Physics of Shock Waves and High-Temperature Hydrodynamic Phenomena*, edited by W.D. Hayes and R.F. Probstein (Dover, New York, 2002)
4. W. L. Kruer, *The Physics of Laser-Plasma Interactions* (Addison-Wesley, 1988).
5. J.P. Christiansen *et al.*, "MEDUSA a one-dimensional laser fusion code," Comp. Phys. Commun. **7**, 271 (1974).
6. Y. Sentoku *et. al.*, "Laser light and hot electron micro focusing using a conical target," Phys. Plasmas **11**, 3083 (2004).

II. Texas Petawatt construction activities

The Center is also undertaking an extensive campaign of laser development, focusing on the development of the Texas Petawatt laser. Since these activities are described in detail elsewhere, we simply summarize them in this section. Greater details on the Texas Petawatt project can be found in the Texas Petawatt Conceptual Design Report.

II.A Development of the Texas Petawatt Laser

Participants:
*E. W. Gaul, , M. D. Martinez, S. Douglas, J. Blakeney, D. Gorski, W. Henderson and T. Ditmire (**University of Texas**)*
*A. Erlandson, J. Caird, C. Ebbers, I. Iovanovic, W. Molander, B. Stuart (**Lawrence Livermore National Laboratory**)*

Within TCHILS the development of a novel a petawatt laser has been proposed as the experimental core of the research center. The nature of many of the experiments proposed, require a pulse width near 100 fs. Also, pulse energies of between 100-300 J are desirable. Activity over the past year has included conclusion of the detailed design of the laser as well as initial procurements and construction.

In recent years a number of approaches to high energy chirped pulse amplification (CPA) have been explored. These recent advances in high intensity laser development were described in 2004 at the International Conference on Ultrahigh Intensity Lasers (ICUIL) [1]. In particular, Nd;glass systems have been extremely successful in pushing CPA to the multi-joule level, as illustrated with the extreme scaling of CPA in Nd;glass by the LLNL Petawatt [2]. While Nd:glass is attractive because of the high quality, large aperture amplifiers that are possible, Nd:glass exhibits a rather limited gain bandwidth of about 10 nm. Additionally, gain narrowing further diminishes the spectral width of a broadband seed pulse and prohibits recompressed pulse widths much below one picosecond. Thus, a straightforward Nd:glass architecture is not appropriate for the laser parameters envisioned (200J/150FS). CPA with Ti:sapphire has been demonstrated with pulses down to 20 fs and several joules, and a number of groups worldwide are currently pushing Ti:sapphire lasers to the multi-hundred TW level by increasing the energy and crystal size. Despite the broad bandwidth available, Ti:sapphire's largest disadvantage for high energy systems is that the short excited state lifetime of Ti:sapphire (3.2 μs) demands that it be pumped by a second laser operating in the green (such as the second harmonic of a ns Nd:YAG or Nd:glass laser). Although gain narrowing is not as significant in Ti:sapphire, the gain per pass is very limited at the peak fluorescence of Nd:glass. Ultimately, crystal size, and the cost of pump laser prohibit this approach for the Texas Petawatt Laser.

To push the pulse width limit attainable in Nd:glass laser systems, a hybrid approach will be taken, which uses a broadband amplification for the majority of the system gain (10^9) up to the joule level and then Nd:glass amplifiers are used to extract the bulk of the energy with an overall gain approximately 10^2. The principal approach of the Texas Petawatt laser is to use OPCPA,

which is more flexible in selecting a gain maximum. Also, operating at least one OPCPA stage in saturation can increase the bandwidth of the seed pulse. After more than nine orders of magnitude net gain in OPCPA, the bandwidth will effectively broaden. More than 99% of the energy with a gain of <300 will be extracted out of Nd:glass amplifiers. By balancing the gain between silicate and phosphate Nd:glass a final bandwidth of 10-12 nm can be reached leading to compressed pulsewidths of 150-170 fs.

Figure II.A.1 displays a schematic layout of the laser system. A Ti:sapphire oscillator produces 100 fs pulses at 1057 nm. The pulses are stretched to 1.8 ns (GDD = 115 ps/nm) by double passing (8 grating reflections) a compact, folded stretcher. The stretcher is a modified Banks stretcher ref [2], which replaces the mirror stripe on the grating with a stripe mirror mounted in front of the grating to allow a higher bandwidth transmission for a smaller size grating. The pulses then pass through a Dazzler to correct phase distortions and to pre-shape the spectrum. After a Pockels cell slicer the 10 Hz pulses are amplified in two OPCPA stages, which are pumped by a commercial 8 ns, 1.2 J Q-switched laser with a top hat spatial profile. The first stage uses three 15 mm long BBO crystals with walk-off compensation and a gain of ~100 per crystal. The second stage uses a walk-off compensated pair of BBO crystals with a saturated total gain of ~100 and an output bandwidth > 30 nm. Figure II.A.2 illustrates spectral modeling results of the different amplifier stages. Such an OPCPA laser has been demonstrated and it was found that reducing the gain per crystal and simply adding additional crystals for the system net gain improved the reliability of the amplifier which allows the use of commercial Q-switched lasers for pumping. Using a commercial pump laser offers reduced complexity and price for pumping OPCPA. The output of these stages will be ~50-100 mJ and the bandwidth is limited by the size of the stretcher optics to < 42 nm. A serrated aperture in combination with a spatial filter shapes the beam to an 8th order super-Gaussian profile. The spatial profile is also slightly truncated on the sides to match the compressor clear aperture given by the grating size. A third OPCPA stage then increases the energy to 0.8 J. This stage will use a single crystal and requires a custom pump laser that produces about 4 J in 4 ns with spatially and temporally flat pulses.

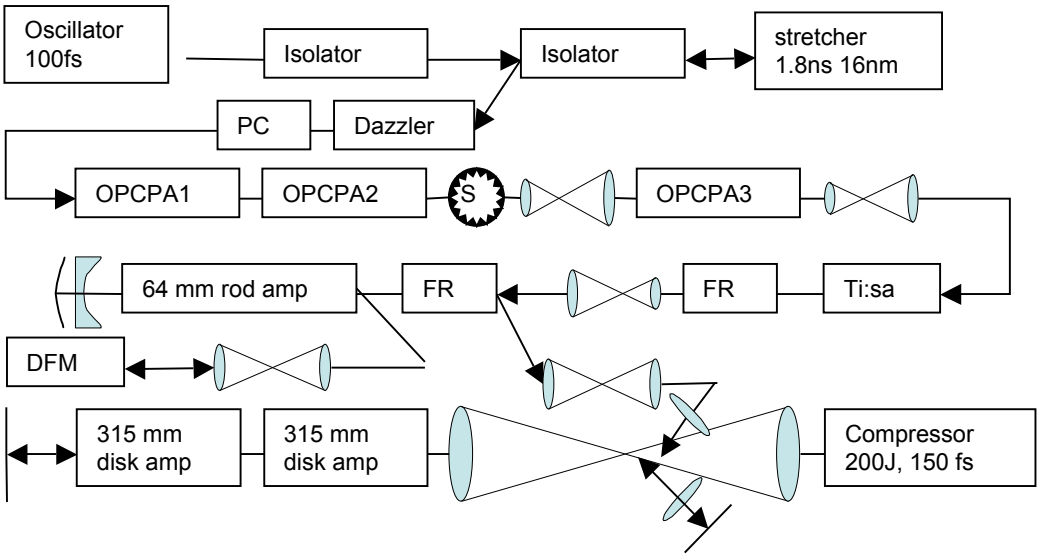

Figure II.A.1: Block diagram of the laser chain. PC is a slicer Pockels cell, DFM is a deformable mirror for wavefront correction, FR are Faraday rotators, SA is a serrated aperture.

The 1J pulse is then injected into a passive 4-pass through a 64 mm diameter, 240 mm long rod amplifier with silicate Nd:glass and yields an output energy of 31 J with a B-integral less than 0.5 radian. The Faraday rotator used for passive switching also ejects back reflections from the main amplifiers. The final stage is a 4-pass in a pair of 315 mm NOVA amplifiers, which contain two phosphate Nd:glass disks in each amplifier. The four passes are separated by angular multiplexing and are isolated with pinholes. About 400 J can be extracted out of these disks with an additional B-integral of only 0.25 radians due to the large beam size. However, the energy extracted will be limited to about 300 J due to the peak fluence limitations on the final grating. After the final pass through an amplifier disk the pulses are relay imaged into the compressor. The design goals for the individual amplifier stages are summarized in table II.A.1.

Table II.A.1 Designs goal for various stages of the laser chain.

Amplifier Stage	Energy [J]	Pulsewidth [ns]	Spectral Bandwidth [nm, FWHM]	ΣB	Beam Size [mm]
oscillator	10^{-9}	100 fs	16.4		3 (Dia.)
OPCPA2	.050	3.5	33		8 (Dia.)
OPCPA3	.80	3.5	33	.01	12 (Dia.)
rod amplifier	31	1.58	12.5	.50	45x55
2^{nd} pass disk	90	1.72	14.7	.55	180x220
4^{th} pass disk	250	1.47	12.4	.80	180x220
compressor	200	150 fs	12.0	.80	180x220

The double pass compressor uses a pair of 40x80 cm multilayer dielectric coated gratings with 1740 lines/mm at 124 cm separation and 73.2 degree angle of incidence. The input mirror has a vertical tilt of 0.65 degrees to separate the input and output beam and the rooftop mirror is replaced by a 0 degree mirror. The footprint of the incident and outgoing beam on the grating partially overlap which effectively increases the clear aperture though the compressor in the vertical dimension by up to 50 % reducing the fluence on the gratings. The damage fluence of the dielectric gratings is currently not well known for pulses as short as 150 fs. An operational fluence of just below 1 J/cm^2 in the beam is anticipated as reasonable. The vertical spatial chirp resulting from the tilt is negligible. The serrated aperture matches the beam size to the compressor's clear aperture and defines an image plane, which will be relay imaged throughout the chain.

One image plane will be at the deformable mirror after the second pass in the rod amplifier. A second image will be before the injection into the disk amplifier, where a static phase plate can be inserted to correct for wave front aberration of the lenses. Aberrations are induced by passing off axis though the lenses in the disk amplifier section, which also requires a meniscus lens close

to the Nd:glass disk to avoid critical ghost foci. Large lenses introduce besides the wave front distortions a significant amount of spatial group delay chirp and spatial group delay dispersion chirp [4]. The center of the beam passes through an additional ~4 cm of lens glass material compared to the edge of the beam, which leads to additional 1.3 ps group delay at the center and additional group delay dispersion broadens the pulse by 40 fs at the center of the beam. Both effects can be reduced by using achromatic lenses or by inserting extra material at the edge of the beam which can be done by replacing the mirror at the rod amplifier with a negative lens and a curved mirror.

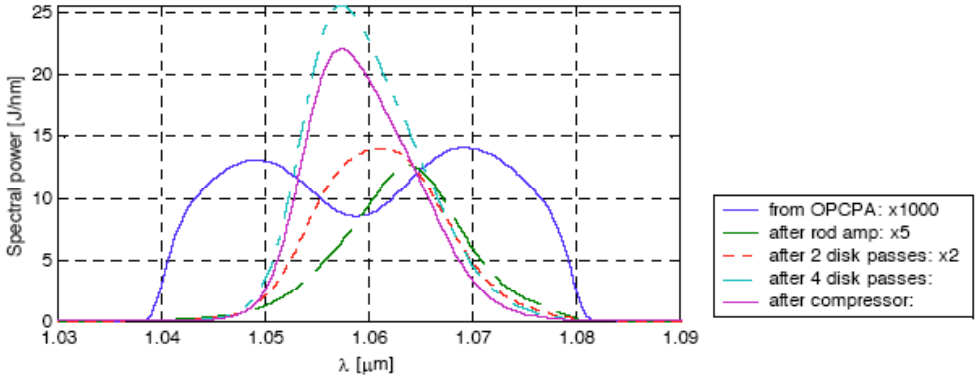

Figure II.A.2 Normalized spectral power after several amplifier stages

The laser is constructed inside a 1600 sqft, class 100,000 cleanroom and will be assembled on a 180 sqft optical table. The compressor which is fits on a 5x8' breadboard inside a vacuum vessel will be installed outside the cleanroom in the target area near two target chambers which are enclosed by a concrete brick wall for radiation shielding. The capacitor storage bank and the pulsed power equipment for the disk amplifiers are located in a separate room. A full system shot sequence will be initiated remotely in a separate control room with a full suite of controls and diagnostics systems interface.

When the facility (figure II.A.3) is fully commissioned, the Texas Petawatt will also employ a long pulse laser (500J, 532nm @ 1-20ns) not described in this paper. This high energy (500 J), long pulse (1-20 ns), synchronized laser is proposed to complement the Texas Petawatt Laser. The combination of this short pulse laser with a second long pulse laser beam enables an even greater range of high energy density studies.

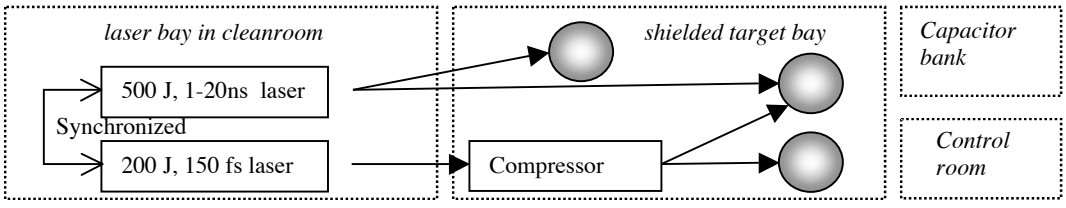

Figure II.A.3 Schematic overview of the Petawatt facility.

In the past year much work has been done on the front end of the laser through the OPCPA stages. The man stages are the laser frontend, the OPCPA gain section, the rod and disk glass amplifier, the compressor, the target areas and controls. The oscillator has been operated routinely from day to day. The stretcher has been refined to optimize the residual spatial chirp from the oscillator. Relay imaging throughout the laser chain is required since the system does not have a filtering cavity after the oscillator.

Several different configurations have been investigated for the first two OPCPA stages. The final version uses a pair of 15 mm long BBO crystals with walk off compensation per stage. The crystals are cut 1 degree of phase matching angle to reduce parametric fluorescence. The pump beam is set at 200 MW/cm^2 which significantly reduces the risk for optical damage, but is sufficient to get saturation in the second stage. A one degree separation between pump and seed beam increases the phase matching bandwidth to 100 nm, well beyond the requirements. It also separates the idler beam and allows it to be blocked by an iris before the following stage.
The current output of the second stage is 40 mJ. This can be increased by delaying the 8 ns long pump beam so it with the ~3ns seed beam at is peak intensity. However, this will compromise the spatial quality of the amplified seed. The spatial profile at the beginning of the pump beam is shaped Gaussian, but develops into a ring shaped structure towards the end of the pulse. The spatio-temporal peak of the pulse has been measured as shown in Fig. 3 (top panel). If the seed pulse is amplified to the maximum energy the shape will also be like a ring which is much less suitable for further amplification.

The pulse broadens form 1.8 ns to 3.5 ns in the second OPA stage due to saturation. The saturation can be tuned by changing the pump intensity or the phase matching angle and the timing of the pump pulse. This allows for some flexibility of the temporal/spectral profile of the output and can be used to optimize the bandwidth after the glass amplifiers. The middle panels in Fig 3 show the near field output at 40 mJ and two temporal profiles with varies delay between pump and seed. Both show saturation off the pulse, but the pulse width/spectrum is shifted.
For the third stage a custom pump laser has been ordered with 4J in 4 ns and a spatially and temporally flat beam profile. The laser has been delivered and installed with several months delay due to delays from the supplier of the subcomponents. Some commissioning data of the 4J laser are shown in Fig 3 (bottom panels) The third stage which has a pair of 25 mm long 30 mm wide KDP crystals is currently commissioned.

The Nd:silicate rod amplifier has been built at the supplier and is currently undergoing final test. Two 64 mm glass rods of N0306 silicate were purchased, polished and coated to specifications. The type of silicate is slightly different form the Schott silicate originally envisioned. The spectral peak is not quite as far from the phosphate peak as for Schott LG680, but simulations suggest that the bandwidth will still be sufficient to produce 150 fs compressed pulses if the seed can be manipulated as suggested above. Different laser glass has been investigated as and alternative/ upgrade which would reduce the final pulse width below 100 fs [5]. Delivery and installation of the rod amplifier system is scheduled for March 2006.
The spatial filters for the rod amplifier four pass section use Nova laser parts which have modified at UT to fit the Petawatt layout and specifications. The remaining hardware for the rod amplifier stage and some diagnostic is in house.

The disk amplifier requires refurbishing of the Nova A315 parts. They laser disks are currently been polished. The amplifier housing will be cleaned and verified at LLNL. The parts will then be shipped to UT and the final assembly is with the disk is in house. The reflector panels will be coated with a Miro finished silver plate. This material does not oxidize under air environment and allows the purge with dry air instead of nitrogen. Nitrogen poses a significant health risk in a cleanroom with limited fresh air circulation. An upgrade to the dry air supply of the building will be installed in the next few months.

The spatial filter of the disk amplifier uses partially Nova parts, which have also been modified to fit the design. New pinhole and injection sections have been designed engineered and manufactured in house and are currently vacuum tested. None of the available Nova lenses were exactly suitable for the design. However, some lenses need to be reworked on one side and recoated to make them suitable for the Petawatt laser.

Components for pulsed power of these amplifiers are steadily refurbished and tested in parallel to the work on the laser. In addition, some missing parts such as the dump rod assemblies have been made similar to existing LLNL design. Laboratory upgrades such as proper electrical grounding wires and door interlocks have been installed.

The compressor has been modeled using CAD to verify the layout in the target area. A draft of the compressor indicates a 14 feet long cylinder shaped vacuum vessel which contains besides the gratings a switch yard mirror and some diagnostics for pulse duration of the compresses pulse. Most of the other diagnostic is located outside the compressor.

Two target chambers are planed for Petawatt experiments. The first one uses a 12.5 m long focal length off-axis parabolic mirror and fold mirror to keep the evacuated beam path within a reasonable size chamber. A long focal geometry (F-number = 50) and or large focal spot is required for the gas cluster, high harmonic and laser wakefield experiments. This chamber will also be used for two beam experiments with the long pulse laser. The second chamber uses a short 1 m focal length parabola for X-ray generation and high field experiments.

In summary we have accomplished the following tasks in the past year:

- We built and commissioned two OPCPA stages and installed the third stage.
- Purchased and commissioned a custom pump laser with spatially and temporally shaped 4J pulses.
- A 64mm silicate rod amplifier was procured. Initial tests of the gain characteristics were performed on the system and it is ready for installation.
- The glass disks for the main amplifier are being polished and the remaining optics has been procured.
- A control system for the Petawatt front end has been developed. The remaining control hardware for the Petawatt laser has been purchased.

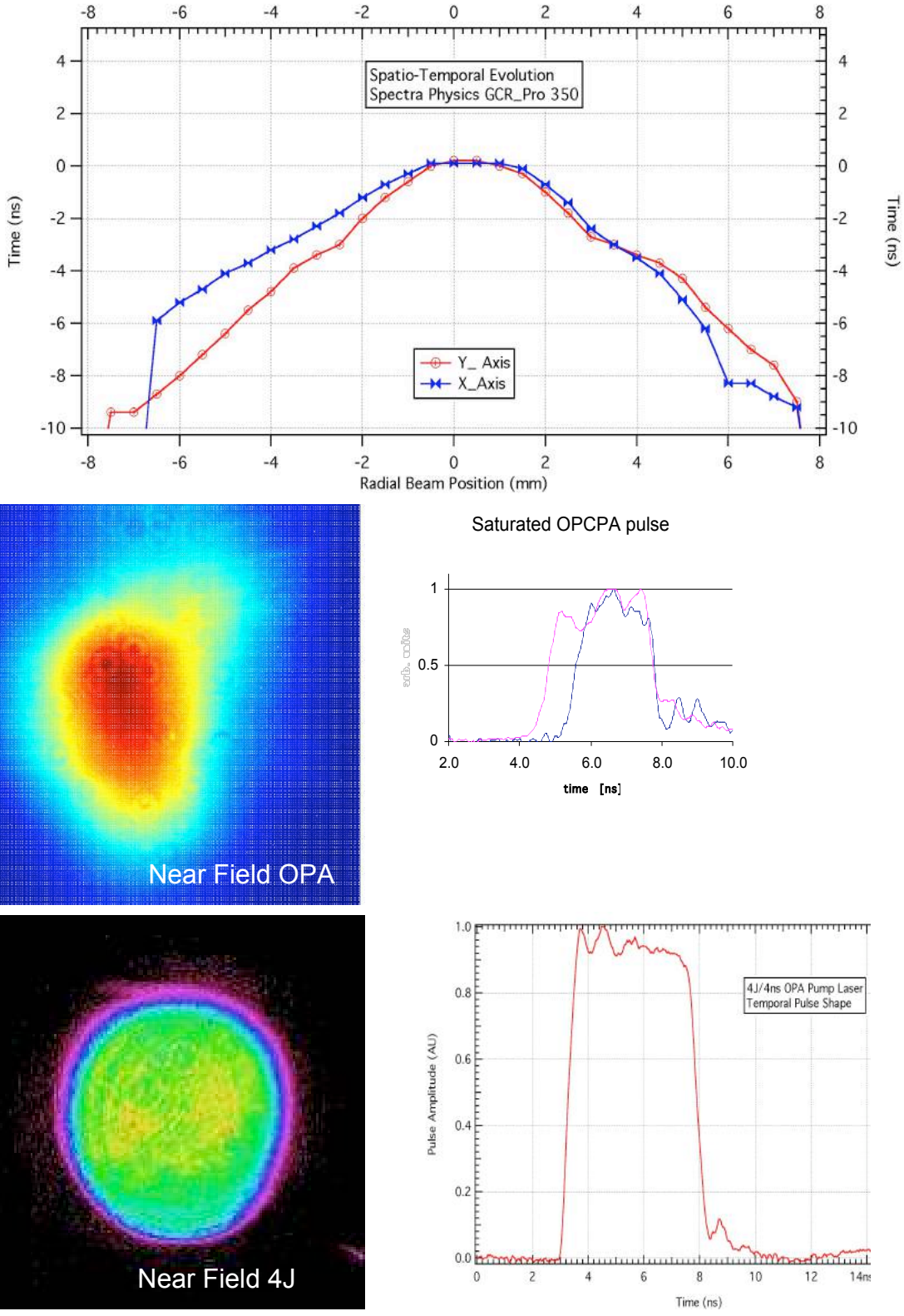

Figure II.A.3 Spatial temporal profile of the pump laser for OPA stages I and II (top). Nearfield and temporal profile of CPA after stage II. Nearfield and temporal profile of the custom pump laser for OPA stage III.

References for section II.A

[1] International Conference on Ultrahigh Intensity Lasers 2004, Tahoe City, CA
[2] M. Perry, *et al*, Opt. Lett. 24, 160 (1999)
[3] I. Jovanovic, *et. al,* Applied Optics, **41**, 2923-2929, 2002
[4] Z. Bor, Journal of modern Optics, **35**, 1907-1918, 1988
[5] E. Gaul *et al* Frontiers in Optics 2005, OSA Annual meeting, Tucson, 2005

II.B Spectral shaping efforts to achieve near 100 fs pulses from a hybrid OPCPA and mixed Nd:glass amplifier

Participants:
*G. R. Hays, E. Gaul, and T. Ditmire (**University of Texas**)*

In addition to the central Petawatt laser development, we have undertaken a smaller scale project that will assess the technology needed to make the Petawatt laser pulses shorter than 200 fs. To do this, we have initiated the construction of a 10 TW scale, hybrid OPCPA/mixed Nd:glass laser. Work this past year has focused on the construction of the front end of this system and characterization of gain in the glas amplifier heads.

This work is motivated by the fact that CPA and the development of high intensity laser systems have been primarily limited to two laser host mediums, Titanium sapphire and Neodymium doped laser glass. Ti:sapphire systems have allowed the development of ultrashort pulses (<30 fs) due to its broad spectral emission. However it is limited by its relatively short fluorescence lifetime making it difficult to generate pulses exceeding a few joules. Nd:glass systems have been successful in pushing CPA to the multi-joule level. The availability of high quality, large aperture amplifiers has made it extremely attractive for high energy applications. However, its chief detractor is its limited spectral emission of 25 nm (FWHM). This limits the amplification of laser pulses with recompressed pulse widths of approximately 1 ps because gain narrowing significantly diminishes the spectral width of the seed.

In order to decrease the pulse width in glass lasers, hybrid systems utilizing Ti:sapphire and Nd:glass have been successfully deployed [1]. Here Ti:sapphire is used both to generate the seed and for preamplification to the several mJ level. The remaining bulk amplification is done in Nd:glass. At 1053 nm Ti:sapphire has extremely low gain making preamplification difficult. In addition the short excited state lifetime leads to rather extensive amplified spontaneous emission (ASE). This in combination with the limited spectral content of Nd:glass allows for compressed pulses of approximately 400 fs.

The recent development of optical parametric chirped pulse amplification (OPCPA) has spurred a great new interest in high intensity laser development [2]. OPCPA possesses and extremely broad and uniform gain spectrum. Gains in excess of 10^3 over a broad spectrum have been

achieved [3]. However, OPCPA is highly nonlinear and requires a strictly uniform pump pulse. This highly formatted pump pulse makes it costly and difficult to achieve amplified energies in excess of 1 J. Further hybrid techniques have utilized the shifted spectral lines of Nd:phospate and Nd:silicate glass [4,5]. The peak emission lines of phosphate and silicate glasses are separated by 8 nm and overlap nicely. By using a mixed glass amplifier chain, a broader gain spectrum is available permitting amplified pulses with up to 16 nm (FWHM). This corresponds to a transform limited Gaussian pulse of 100 fs.

Our efforts have been to produce a hybrid CPA laser system utilizing all three of the previously mentioned techniques. We are developing a unique CPA laser that will combine the laser mediums of Ti:sapphire, OPCPA, and mixed laser glasses in an effort to maintain an amplified spectrum of up to 16nm FWHM. The use of each media in careful balance of gain allows us to develop a several Joule laser pulse with enough bandwidth to achieve a 150 fs in the transform limit.

In order to produce a near 150 fs compressed pulse from a Nd:glass amplifier chain, precision control of the pulse spectrum must be maintained. The natural emission of Nd:phosphate and Nd:silicate laser glasses are each in excess of 25nm FWHM and their peak spectral emissions are separated by 8 nm (Figure.II.B.1 a). Therefore by employing both media in an amplifier chain, the seed pulse experiences a net broader gain spectrum allowing us to reduce the effects of spectral gain narrowing. However the combined gain spectrum is still highly shaped and significant spectral narrowing will occur if the net gain is too high. Our system is designed to limit the gain from glass to 10^2 in the final amplification. Here high energy is achieved by the large energy storage capacity from the laser glass host. There the preamplification is done in a multi-stage OPA.

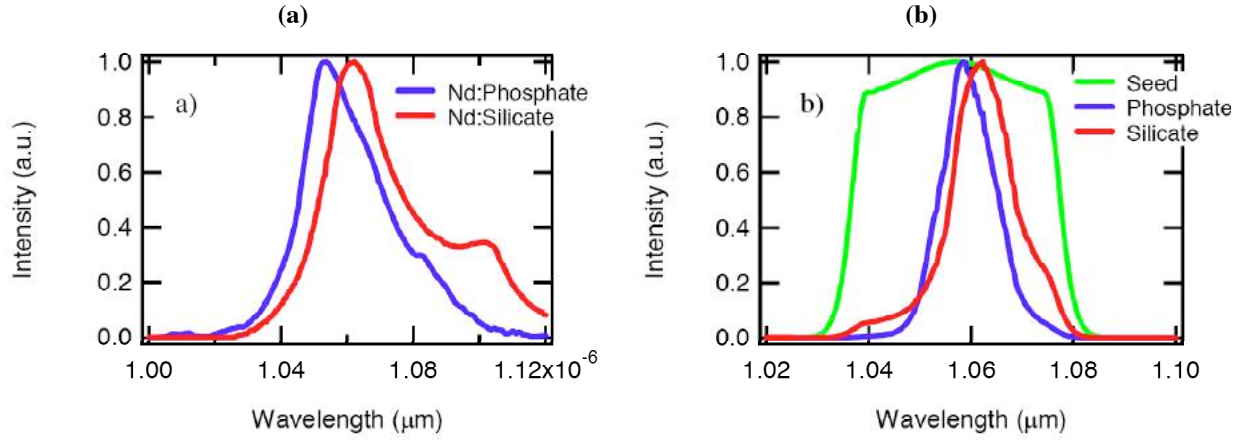

Fig II.B.1. Characteristics of phosphate and silicate laser glasses: (a) spectral emissions of Nd:phosphate and Nd:silicate laser glass, (b) simulated spectral shaping by amplifying a broadband OPCPA seed in a mixed laser glass amplifier chain. The seed is first amplified in Nd:silicate and then secondly in Nd:phosphate.

The benefits of OPCPA are pertinent to our design. Degenerate parametric amplification is inherently broadband. A nearly uniform gain spectrum over a 100 nm bandwidth with a gain of 10^3 is available from a singly passed nonlinear optical crystal. The detractor however is the highly nonlinear intensity dependent gain of the pump pulse. In order to achieve a uniformly

amplified seed, the pump pulse must be both temporally and spatially uniform during the parametric interaction. Therefore an 8 ns, super-Gaussian pump pulse is used. The 1 ns seed is interacted with pump at the temporal peak to where it experiences nearly uniform intensity. Finally gain saturation in such a highly nonlinear medium allows for significant spectral broadening.

The nearly uniform spectrally broadened pulse from the OPA is then seeded into the mixed glass amplifier. Each rod is double passed to allow for efficient energy extraction. However the gain from phosphate and silicate laser glass is not the same. Phosphate glass has a smaller emission cross-section creating a larger small signal gain. Also, silicate glass has a broader spectrum that extends much further into red side of the spectrum. Therefore there exists a natural balance between the two combined gains that produces the largest amplified spectrum. Figure 1b shows our modeling simulations of a mixed glass amplifier. We will present preliminary gain measurements that demonstrate the spectral shaping of a mixed glass amplifier chain.

The laser system is designed by employing a Ti:sapphire based oscillator, an OPCPA preamplifier, and a mixed Nd:glass rod amplifier chain (Figure II.B.2). Our laser system utilizes a commercial Kerr-lens mode-locked, Ti:sapphire oscillator that produces 100 fs pulses with 16 nm of bandwidth (FWHM). The pulse train is then sliced down to 10 Hz and injected into an all-reflective single grating pulse stretcher producing a 1 nJ, 1 ns stretched seed pulse. A 3-stage nearly degenerate OPCPA chain is used for preamplification. Each BBO crystal is pumped by a frequency doubled Nd:YAG laser that is injection-seeded to eliminate temporal mode beating.

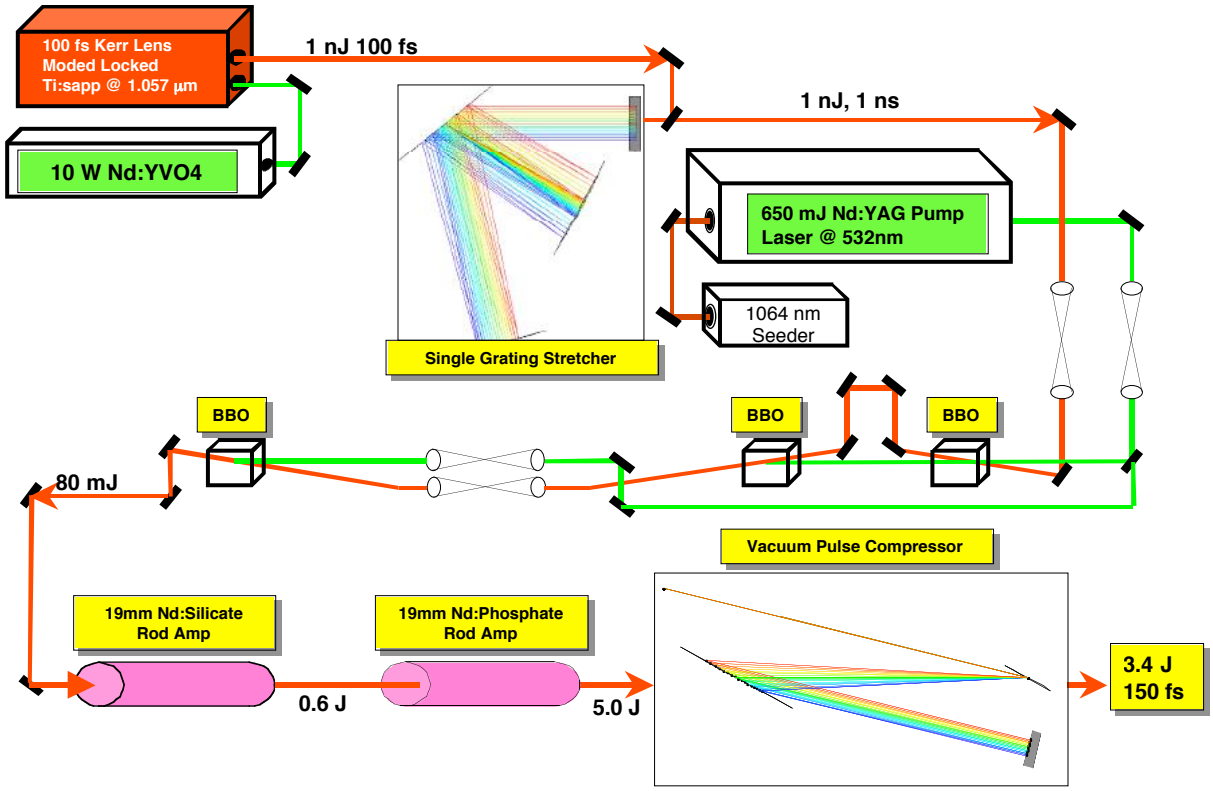

Figure II.B.2 Schematic of the Hybrid OPCPA mixed glass laser

In order to produce a near 150 fs compressed pulse from this Nd:glass amplifier chain, precise control of the pulse spectrum must be maintained. The natural emission of Nd:phosphate and Nd:silicate laser glasses are each in excess of 25nm FWHM and their peak spectral emissions are separated by 8 nm (Figure II.B.1). Our laser is designed to limit the gain from glass to 10^2 in the final amplification. Here high energy is achieved by the large energy storage capacity from the laser glass host. Therefore the pre-amplification is done in a multi-stage OPA.

For the purposes of this investigation we have deployed a scale model of the Texas Petawatt laser to investigate spectral gain narrowing from a mixed-glass architecture. A 16 nm FWHM seed pulse centered at 1057 nm is stretched to 1 ns and then preamplified to 35 mJ in a two stage optical parametric amplifier. The preamplified pulse is spectrally broadened to 26.2 nm which is shown in figure II.B.3. The pulse is then seeded into two 19 mm Nd:glass rod amplifiers, one using APG-1 Nd:phosphate glass and the other LG-680 Nd:silicate. The spectrally broadened pulse was also attenuated to 1 mJ negating the effects of gain saturation and allowing purely small signal gain in the glass amplifiers. Further each rod is double passed to allow for sufficient high gain measurements.

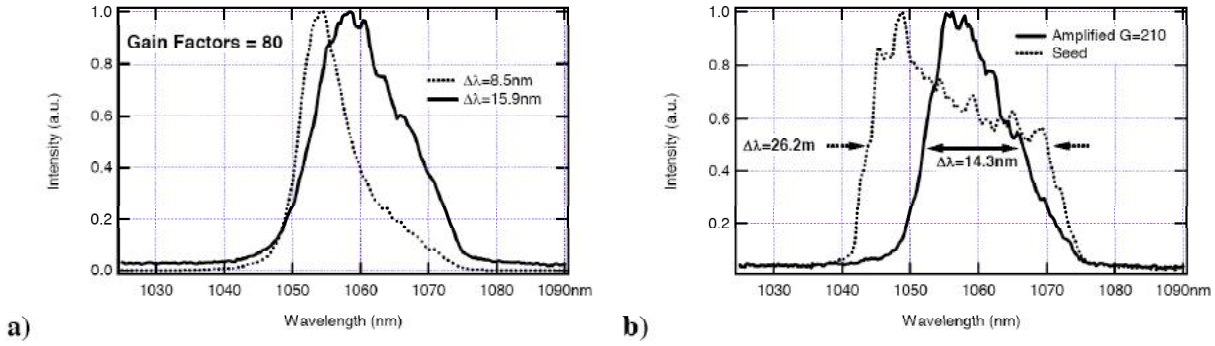

Figure II.B.3 a) Amplified pulse spectra from Nd:glass amplifiers. The dotted line shows amplification in Nd:phosphate glass alone with total gain of 80. The solid line shows an optimized amplified bandwidth with a combined gain of 80 from mixed amplifiers using both Nd:phosphate and Nd:silicate glasses. The gain ratio between phosphate and silicate is 1.2 (G_{phos}/G_{sil}). b) Amplified pulse spectrum from the mixed Nd:glass amplifiers with a combined gain of 210 and gain ratio of 3.2 plotted with the seed pulse spectrum.

Since the gain spectra from phosphate and silicate laser glass are not uniform, there subsequently exists a natural balance between the two combined media that produces the broadest amplified spectrum. By varying the net gain in each rod amplifier, we can control the spectral gain narrowing in the combined system. In Figure II.B.3a, the 26.2 nm spectrally broadened pulse centered at 1057 nm is seeded into a Nd:glass amplifier chain and is amplified by a factor of 80. The dotted line indicates amplification purely in phosphate glass which is subsequently gain narrowed to 8.5 nm. This represents nearly a 70% loss of spectral content. The solid spectrum illustrates amplification also by a factor of 80 in a mixed glass amplifier. In this case over 60% of the spectral content is maintained and the pulse is gain pulled to center at 1059 nm. Figure II.B.3b shows the same pulse amplified by a factor of 210 maintaining 55% of the spectral content. Here the amplified pulse is spectrally centered at 1058 nm with a gain ratio of 1.2 (G_{phos}/G_{sil}).

Figure II.B.4 plots the amplified spectral bandwidth as a function of the gain ratio from the rod amplifier chain. Each point represents the amplified bandwidth with a gain factor of 200. The seed pulse is centered at 1057 nm, which is half way between the two peak emissions of phosphate and silicate. Both media stongly narrow the spectrum without the presence of the other. Individually silicate maintains a broader amplified spectrum over the phosphate amplifier, but this is attributed to its larger emission spectrum The optimum measured gain ratio is revealed in this case to be 3.2 or about 3:1.

Many spectra were measured to have net equal bandwidths with different gain ratios at the same gain level. This is attributed to gain pulling of the spectrum from one amplification center to the other. This is also illustrated in figure II.B.4. In this case when the gain ratio is shifted from 0.04 to 0.24, the net amplified bandwidth is the same; however the spectrum is pulled from the silicate amplification center to the phosphate side. As the ratio increases, the amplified spectrum center moves toward the phosphate center. The peak spectral bandwidth of 14.2 nm centered at 1057 nm was measured with a gain ratio of 3.2. This is precisely centered between the peak emission centers of the two laser glasses.

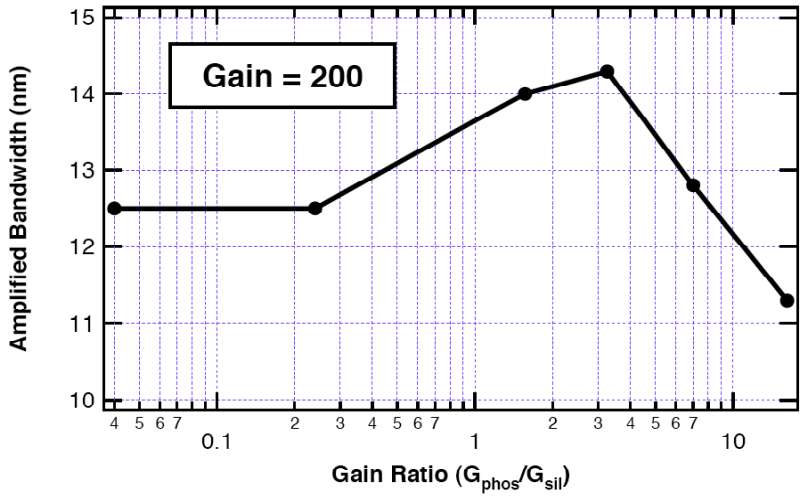

Figure II.B.4. Measured amplified pulse spectrum bandwidth (FWHM) as a function of gain ratio (G_{phos}/G_{sil}) between the two amplifiers. The total gain at each point is 200.

References for section II.B

1. M. D. Perry and B. W. Shore " Petawatt Laser Report" LLNL Internal report UCRL-ID-124933.
2. I.N. Ross, P. Matousek, M. Towrie, A.J. Langley, J.L. Collier, Optics Comm. **144**, 125-133 (1997).
3. I. Jovanovic, B.J. Comaskey, C.A. Ebbers, R.A. Bonner, D.M. Pennington, M.C. Morse, Appl. Opt. **41**, 2923-2929 (2002).
4. R. Danielius, A. Piskarsus, D.Podenas and A. Varanavicius, Optics Comm. **84**, 343-345 (1991).
5. N. Blanchot, C. Rouyer, C. Sauteret and A. Mingus, Opt. Lett. **20**, 395-397 (1995).

III. Supporting Material

III.A Publications resulting from or supported by this NNSA SSAA Center Cooperative Agreement to date

PAPERS AND PUBLICATIONS

1) J. F. Hansen, G. Luca, D. Froula, M. J. Edwards, A. E. Edens and T. Ditmire "Laboratory observation of secondary shock formation ahead of a strongly radiative blast wave" *Phys. Plas.* Accepted.

2) W. Grigsby, A. Dalton, B. Bowes, S. Bless, J. Colvin, E. Taleff, M. Marder, M. Downer, T. Ditmire "Study of laser driven shocks in thin tin slabs" *J. Appl. Phys* to be submitted.

3) F. Buersgens, K. W. Madison[1], D. R. Symes, R. Hartke, J. Osterhoff, W. Grigsby, G. Dyer and T. Ditmire , "Angular distribution of neutrons from deuterated cluster explosions driven by fs-laser pulses", *Phys. Rev. E,* Accepted

4) Bowes BT, Langhoff H, DOWNER MC, Wilcox M, Hou B, Nees J, and Mourou G, "Femtosecond microscopy of radial energy transport in a micrometer-scale aluminum plasma excited at relativistic intensity," *Optics Letters* **31**, 116-118 (2006).

5) A. D. Edens, T. Ditmire, J. F. Hansen, M. J. Edwards, R.G. Adams, P. Rambo, L. Ruggles, I.C. Smith, and J. L. Porter, "Measurement of the decay rate of single-frequency perturbations on blast waves" *Phys. Rev. Lett.* **95**, 244503 (2005).

6) R. Hartke, D. R. Symes, F. Buersgens, L. Ruggles, J. L. Porter, T. Ditmire, "Neutron Detector Calibration using a table-top laser heated plasma neutron source" *Nuc. Inst. And Methods A* **540**, 464 (2005).

7) T.D. Donnelly, J. Hogan, A. Mugler, M. Schubmehl, N. Schommer, Andrew J. Bernoff, S. Dasnurkar and T. Ditmire, "Using ultrasonic atomization to produce an aerosol of micron-scale particles", *Rev. Sci. Instr.* **76**, 113301 (2005).

8) Hansen S.B., Faenov AY, Pikuz TA, Fournier KB, Shepherd R, Chen H, Widmann K, Wilks SC, Ping Y, Chung HK, Niles A, Hunter JR, Dyer G, and Ditmire T, "Temperature Determination Using K-Alpha Spectra from M-shell Ti Ions" *Phys. Rev. E*, **72** 036408 (2005)

9) Edens AD, Ditmire T, Hansen JF, Edwards MJ, Adams RG, Rambo P, Ruggles L, Smith IC, Porter JL, "Studies of laser-driven radiative blast waves" *Astrophys. and Space Sci.* **298,** 39 (2005).

10) Hansen JF, Edwards MJ, Froula D, Gregori G, Edens A, Ditmire T, "Laboratory simulations

of supernova shockwave propagation" *Astrophys. and Space Sci.* **298,** 61 (2005).

11) Presura R, Ivanov VV, Sentoku Y, Sotnikov VI, Laca PJ, Le Galloudec N, Kemp A, Mancini R, Ruhl H, Astanovitskiy AL, Cowan TE, Ditmire T, Chiu C, Horton W, Valanju P, Keely S "Laboratory simulation of magnetospheric plasma shocks" *Astrophys. and Space Sci.* **298,** 299 (2005).

12) Horton W, Chiu C, Ditmire T, "Laboratory simulations of bow shocks and magnetospheres" *Astrophys. and Space Sci.* **298,** 395 (2005).

13) M. Hohenberger, D. R. Symes, K. W. Madison, A. Sumeruk, and T. Ditmire, "Dynamic Acceleration Effects in Explosions of Laser Irradiated Heteronuclear Clusters", *Phys. Rev. Lett.* **95**, 195003 (2005).

14) M. Fomytskyi, C. Chiu, F. Grigsby and M. C. DOWNER, "Controlled plasma wave generation and particle acceleration through seeding of the forward Raman instability," *Phys. Plasmas* **12**, 023103 (2005).

15) Lane, J. M. D. and Marder, M. P. "Numerical method for shock front Hugoniot States." Shock Compression of Condensed Matter 2005. APS Proceedings. (Accepted, in press).

16) Lane, James Matthew Doyle, "A New Continuous Hugoniot Method for the Numerical Study of Shock Waves." Ph.D. Dissertation, UMI, August 2005.

17) K. W. Madison, R. Fitzpatrick, P. K. Patel, D. Price, T. Ditmire, "The role of laser pulse duration in Coulomb explosions of deuterium cluster targets" *Phys. Rev. A* **70**, 053201 (2004).

18) A. D. Edens, T. Ditmire, J. F. Hansen, M. J. Edwards, R.G. Adams, P. Rambo, L. Ruggles, I.C. Smith, and J. L. Porter, "Study of high Mach number laser driven blast waves" *Phys. Plas.* **11**, 4968 (2004).

19) L. E. Ruggles, J. L. Porter, W. W. Simpson, M. F. Vargas, D. M. Zagar, R. Hartke, F. Buersgens, D. R. Symes, T. Ditmire, "High sensitivity neutron detector for Z" *Rev. Sci Inst.* **75**, 3595 (2004).

20) T. Ditmire, S. Bless, G. Dyer, A. Edens, W. Grigsby, G. Hays, K. Madison, A. Maltsev, J. Colvin, M. J. Edwards, R. W. Lee, P. Patel, D. Price, B. A. Remington, R. Sheppherd, A. Wootton, J. Zweiback, E. Liang and K. A. Kielty, " Overview of future directions in high energy-density and high-field science using ultra-intense lasers" *Rad. Phys. And Chem.* **70**, 535 (2004).

21) K. W. Madison, P. K. Patel, D. Price, A. Edens, M. Allen, T. E. Cowan, J. Zweiback, and T. Ditmire, "Fusion neutron and ion emission from laser induced explosions of deuterium and deuterated methane clusters" *Phys. Plas.* **11**, 270 (2004).

22) B. T. Bowes, M. C. Downer, H. Langhoff, M. Wilcox, B. Hou, J. Nees and G. Mourou, "Ultrafast Radial transport in a micron-scale aluminum plasma excited at relativistic intensity," in *Advanced Accelerator Concepts*, *AIP Conference Proceedings* **737**, 609-613 (2004). Presented at 11th Advanced Accelerator Concepts Workshop, Stony brook NY, 23 June 2004.

23) R. Zgadzaj, E. W. Gaul, N. H. Matlis, M. C. DOWNER, and G. Shvets," Femtosecond pump-probe study of preformed plasma channels," *J. Opt. Soc. Am. B* **21**, 1559-1567 (2004).

24) B. Shim, G. Hays, M. Fomytskyi, A. Arefiev, B. Breizman, T. Ditmire and M. C. DOWNER, "Time-resolved harmnonic generation from exploding noble-gas clusters," in *Advanced Accelerator Concepts*, *AIP Conference Proceedings* **737**, 777-782 (2004). Presented at 11th Advanced Accelerator Concepts Workshop, Stony brook NY, 22 June 2004.

25) M. Fomytskyi, C. Chiu, F. Grigsby and M. C. DOWNER, "Controlled plasma wave generation and particle acceleration through seeding of the forward Raman instability," *Phys. Plasmas* **12**, 023103 (2004).

26) C. Chiu, M. Fomytskyi, F. Raischel, F. Grigsby, M. C. DOWNER and T. Tajima, "Laser accelerators for radiation medicine: a feasibility study," *J. Med. Phys.* **31**, 2042-2052 (2004).

27) A. Maltsev and T. Ditmire, "Above Threshold Ionization in Tightly Focused, Strongly Relativistic Laser Fields" *Phys. Rev. Lett.* **90**, 053002 (2003).

28) K. W. Madison, P. K. Patel, M. Allen, D. Price, T. Ditmire, "An investigation of fusion yield from exploding deuterium cluster plasmas produced by 100 TW laser pulses" *J. Opt. Soc. Am. B* **20**, 113 (2003).

29) G. Dyer, R. Sheppherd, J. Kuba, E. Fill, A. Wootton, P. Patel, D. Price, T. Ditmire, "Isochoric heating of solid aluminium with picosecond X-ray pulses," *J. Mod. Opt.* **50**, 2495 (2003).

30) J. Kuba, A. Wootton, R. M. Bionta, R. Shepherd, E. E. Fill, T. Ditmire, G. Dyer, R. A. London, V. N. Shlyaptsev, J. Dunn, R. Booth, S. Bajt, R. F. Smith, M. D. Feit, R. Levesque, M. McKernan, "X-ray optics research for free electron lasers: study of material damage under extreme fluxes," *Nuc. Inst. Meth. A – Accelerators, Spectrometers Detectors and Associated Equipment* **507**, 475 (2003).

31) J. F. Hansen, M. J. Edwards, H. F. Robey, A. Miles, D. Froula, G. Gregori, A. E. Edens and T. Ditmire "Laboratory Simulations of Supernova Shockwave Propagation and ISM Interaction" in *Inertial Fusion Science and Applications 2003,* Proceedings of the American Nuclear Society (2004).

III.B Students and Post Docs supported on this cooperative agreement

Project Participants	Percentage of Time of Support (Based on 12 mos.)	Period of Appointments
Undergraduates (Part/Time)		
Bansal, Gaurav	21.3	06/01 - 12/31/05
Dziuk, Janna	4.0	06/01 - 12/31/05
Escamilla, Jose	5.1	10/17 - 12/20/05
Gerrity, Michael	11.1	03/01 - 12/31/05
Gonzales, America	6.3	05/01 - 08/15/05
Hammond, Douglas	42.0	05/23 - 12/31/05
Herrera, Miguel	24.7	06/13 - 12/31/05
McKay, Justin	12.8	05/23 - 07/31/05
Schnose, Elise	3.8	01/25 - 05/31/05
Graduate Research Assistants		
Allen, Jonathan	5.4	04/25 - 06/08/05
Avila, Marco	58.3	06/01 - 12/31/05
Belolipetski, Alexei	4.2	06/01 - 06/15/05
Bowes, Benjamin	37.7	01/01 - 01/15/05, 09/01 - 12/31/05
Brady, Parrish	54.3	01/16 - 02/28/05, 08/01 - 12/31/05
Brewer, Jonathan	54.3	01/16 - 03/31/05, 09/01 - 12/31/05
Churina, Irina	33.3	09/01 - 12/31/05
Dalton, Douglas	33.3	09/01 - 12/31/05
Dyer, Gilliss	16.7	05/01 - 06/30/05
Edens, Aaron	12.7	01/16 - 02/28/05
Hays, Greg	99.8	01/16 - 12/31/05
Henig, Andreas	33.3	09/01 - 12/31/05
Keely, Sean	54.3	01/16 - 03/31/05, 09/01 - 12/31/05
Kneip, Stefan	37.5	09/01 - 09/15/05. 10/01 - 12/31/05
Lane, Matt	66.7	01/01 - 08/31/05
Milathianaki, Despina	46.0	01/16 - 02/28/05, 09/01 - 12/31/05
Morgan, Robert	46.0	01/16 - 02/28/05, 09/01 - 12/31/05
Murphy, Brenden	12.7	01/16 - 02/28/05
Sumeruk, Ariel	12.7	01/16 - 02/28/05
Postdocs		
Bernstein, Aaron	39.3	01/11 - 05/31/05
Lane, Matt	33.3	09/01 - 12/31/05
Symes, Dan	66.7	05-01 - 12/31/05
Technical Staff		
Blakeney, Joel	74.1	03/28 - 12/31/05
Carter, Keith	4.2	01/01 - 01/31/05
Douglas, Skyler	100.0	01/01 - 12/31/05
Gorski, Dan	100.0	01/01 - 12/31/05
Henderson, Watson	91.7	01/01 - 12/31/05
Ringuette, Martin	16.7	11/01 - 12/31/05
Researchers		
Arefiev, Alexey	50.0	01/01 - 12/31/05
Ditmire, Todd, P.I.	16.7	06/01 - 07/31/05
Gaul, Erhard	100.0	01/01 - 12/31/05
Hoffmann, Kay	100.0	01/01 - 12/31/05
Martinez, Mikael	100.0	01/01 - 12/31/05